A COMPARISON STUDY OF ACTUATORS AND PATH PLANNERS FOR INCREASING ROBOT SAFETY

A COMPARISON STUDY OF ACTUATORS AND PATH PLANNERS FOR INCREASING ROBOT SAFETY

BY

JIAWEI XU, B. Eng.

A Thesis
Submitted to the School of Graduate Studies
in Partial Fulfilment of the Requirements
for the Degree
Master of Applied Science

McMaster University

MASTER OF APPLIED SCIENCE (2022) McMaster University

(Mechanical Engineering) Hamilton, Ontario, Canada

TITLE: A comparison study of actuators and path planners for increasing robot safety

AUTHOR: Jiawei Xu

B.ENG., (McMaster University, Canada)

SUPERVISOR: Dr. Gary M. Bone, Professor

NUMBER OF PAGES: xxv, 136

LAY ABSTRACT

A robotic arm's performance and safety are important factors in both industrial and non-industrial applications. In this thesis, performance is measured by how precisely the robot moves along a desired trajectory, and safety is measured by the maximum contact force that occurs in a simulated collision between the robot and a human head. The use of four different actuators to drive the joint of a robotic arm is simulated and the actuators' performance and safety are discussed and compared. In addition, several methods to improve robot safety are proposed and simulated, and their advantages and disadvantages are discussed in detail. Finally, we propose and simulate a new path planner for a robotic arm with three motorized joints. The path planner is shown to be effective at improving safety and can be applied to more robots than existing methods.

ABSTRACT

Since robotic arms operating close to people are increasingly common, there is a need to better understand how they can be made safe, while still providing the required performance. The objective of this thesis is to study and compare various actuators and methods for improving robot safety.

It begins with a study of the safety and performance of a one degree of freedom (DOF) robotic arm whose parameters are mostly derived from the first joint of a 6-DOF industrial robot. The use of electric actuator (EA), series elastic actuator (SEA), pneumatic actuator (PA) and hybrid pneumatic electric actuator (HPEA) with model-based controllers to drive the robotic arm, and the collision between the arm and a human head, are simulated. The simulation employs dynamic models of the robot, actuators, and collision. The addition of a compliant covering to the arm, and the use of collision detection and reaction strategies are also studied. The performance and safety of the robot are quantified using root mean square error (RMSE) between the desired and actual joint angles in the trajectory, and maximum impact force (MIF), respectively. When compliant covering and the collision reaction strategy “withdrawing the arm (WTA)” are both applied, and the detection delay is 25 ms, the MIF reduced by 65% or more. Furthermore, when the desired closed-loop bandwidth is chosen individually, EA has the best performance, and SEA and PA are the safest. The HPEA is the best choice when considering both safety and performance.

Next, the relationship between the joint angles and the reflected mass of a 3-DOF planar robot is studied. A novel optimal path planner for reducing the reflected mass is then proposed. Simulation results show the planner can reduce the MIF by 75%, while still being able to bring the robot's end-effector to the target position precisely.

ACKNOWLEDGEMENTS

I would like to express my sincere gratitude to my research supervisor, Dr. Gary M. Bone, who generously provided knowledge and expertise. He graciously helped me at every stage of my research and patiently answered every question I asked. Without him, I could never have finished this thesis.

I would also like to thank my colleagues: Peige Guo, Behrad Rouzebh and Abdelrahman Zaghloul, they gave me a lot of advice during my research.

Finally, I would like to thank my family and friends for their encouragement and support.

TABLE OF CONTENTS

LIST OF TABLES

LIST OF FIGURES

NOMENCLATURE

A_g	Total cross-sectional area of each CG
A_{v1}, A_{v2}	The orifice area for each valve
A_{vd1}, A_{vd2}	The desired orifice area for each valve
A_{vgain}	Valve gain factor
C_1, C_2, C_f	Valve coefficient
C_{neck}	Neck damping coefficient
C_{v1}, C_{v2}, C_{v3}, C_{vf}	UR5 coefficient of viscous friction
$\hat{C}_{v1}$, $\hat{C}_{vf}$	The predicted value of UR5 coefficient of viscous friction
d_{foam0}	Initial thickness of compliant covering
D_h	Head deflection
$d_{\min}$	Lower thickness limit of compliant covering
d_p	The compressed thickness of the compliant covering
dt	Integration timestep
f_{bw}	Desired closed-loop bandwidth
F_c, $\hat{F}_c$	The Coulomb friction force and its predicted value
$F_{contact}$	Contact force
F_{cx}, F_{cy}	Contact force in x and y direction
F_p, $\hat{F}_p$	The force given by the PA and its predicted value

F_s , $\hat{F}_s$	The static friction force and its predicted value
g	Acceleration of gravity
$\mathbf{h}$	The sum of the Coriolis and centripetal torques for the 3-DOF planar robot
I_{r1}	The moment of inertia of the link
$\hat{I}_{r1}$	The predicted moment of inertia of the link
J_1 , J_2 , J_3	The motor inertia
$\hat{J}_1$, $\hat{J}_2$, $\hat{J}_3$	Predicted value of the motor inertia
$\mathbf{J}_r$	Robot's Jacobian matrix
$\mathbf{J}_{xy}$	First and second row of $\mathbf{J}_r$
k	The ratio of specific heats for air
k_p	A positive constant used in the simpler planner
K_{b1}	A gain that should be made slightly smaller than 1
K_{p1} , K_{d1}	Proportional and derivative terms of the PD controller of the EA
K_{dp1} , K_{dd1}	Proportional and derivative terms of position controller of SEA
K_{pp1} , K'_{dp1}	Proportional and derivative terms of position controller of PA and HPEA
K_{pm1} , K_{dm1}	Proportional and derivative terms of the electric controller of HPEA
K'_{p1} , K_{i1}	Proportional and integral terms of pressure controller of PA and HPEA
$K_{\tau p1}$, $K_{\tau d1}$	Proportional and derivative terms of torque controller of SEA

K_{foam}	Compliant covering stiffness
K_{head}	Head stiffness
K_{neck}	Neck stiffness
K_{s1}	Spring stiffness of the SEA
K_{sum}	Combined stiffness of head and compliant covering
L_1	Distance from the EE to the rotation axis of the first joint
$\mathbf{M}$	The inertia matrix for the 3-DOF planar robot
m_1, m_2, m_3	Mass of the link
$m_{contact}$	Reflected mass
$\mathbf{M_{cs}}$	The robot's Cartesian space inertia matrix
m_{head}	Head mass
$\dot{m}_1$, $\dot{m}_2$, $\hat{\dot{m}}_{d1}$, $\hat{\dot{m}}_{d2}$	The overall mass flow rate into the CGs and their sensed values
$m_{payload}$	Payload mass
$m_{PayloadM\mathrm{ax}}$, $m_{PayloadMin}$	Maximum and minimum allowed payload for the UR5 robot
n_{cx}, n_{cy}	Contact normal
$objective$, obj_1, obj_2, obj_3	Objective function of the path planar and its components
P_1, P_2, $\hat{P}_1$, $\hat{P}_2$	the pressures inside CG1 and CG2 and their estimated value
P_{1d}, P_{2d}	The desired chamber pressures

$\tilde{\dot{P}}_1$, $\tilde{\dot{P}}_2$	Estimated value of rate of change of chamber pressures
P_{atm}	The atmospheric pressure
P_{cr}	Critical pressure ratio that differentiates subsonic and sonic flows in the valve
P_{dj}	The down-stream pressure
P_S	The supply pressure
P_{uj}	The up-stream pressure
Q	The weight of the path planner for keeping the end effector on the path
R	The universal gas constant
R_{acc}	The weight of the path planner on the desired angular acceleration of the joints
R_{g1}, R_{g2}, R_{g3}	HDT transmission ratio
r_i	Inertia ratio
r_p	Pitch radius of pinion gear
T	Air temperature
T_c, T_p	Sampling period
t_d	Collision detection delay
u_1, u_2	The valve input
$\mathrm{u}_{\mathrm{valvemax}}$	Maximum value of the valve input
V_{01}, V_{02}	CG1 and CG2 volumes at $\theta=0$

V_1, V_2, $\hat{V}_1$, $\hat{V}_2$	CG volumes and their sensed values
$v_{\max}$	Maximum desired EE velocity
v_{xd}, v_{yd}	X and Y components of desired EE velocity
x_d, y_d	X and Y components of desired EE position
x_{head}	The position of the head
x_{head0}	The equilibrium position of the head
$\dot{x}_{head}$, $\ddot{x}_{head}$	The velocity and acceleration of the head
x_{robot}, y_{robot}	The coordinates of the EE of the robot
ξ, ξ_{out1}, ξ_{in1}, ξ_{p1}, ξ_{d1}, ξ_{m1}	Damping ratio
ΔP_{1d}	Desired pressure change
$\Delta\theta_{d1}$, $\Delta\theta_{d2}$, $\Delta\theta_{d3}$	Desired change in the joint angles
$\Delta\theta_{d1previous}$, $\Delta\theta_{d2previous}$, $\Delta\theta_{d3previous}$	$\Delta\theta_{di}(i=1,2,3)$ value of previous short period of time
θ_1, θ_2, θ_3	Joint angle
$\dot{\theta}_1$, $\dot{\theta}_2$, $\dot{\theta}_3$	Joint angular velocity
$\ddot{\theta}_1$, $\ddot{\theta}_2$, $\ddot{\theta}_3$	Joint angular acceleration
$\hat{\theta}_j$, $\dot{\hat{\theta}}_j$, $\ddot{\hat{\theta}}_j$ ($j=1,2,3$)	Estimated joint angle, angular velocity and angular acceleration
θ_{1d}, θ_{2d}, θ_{3d}	Desired joint angle

$\dot{\theta}_{1d}$, $\ddot{\theta}_{1d}$, $\dddot{\theta}_{1d}$	Desired joint angular velocity, acceleration and jerk
θ_{M1}, $\dot{\theta}_{M1}$, $\ddot{\theta}_{M1}$	Motor's rotor angle, angular velocity and acceleration
θ_{sensed}	Sensed angle of the link
μ_1, μ_2	PWM duty cycle for the supply valve of the associated CG
τ_{A1}	Actuator torque
τ_{A1d}, $\dot{\tau}_{A1d}$, $\ddot{\tau}_{A1d}$	Desired actuator torque and its derivative
τ_{C1}, $\hat{\tau}_{C1}$, τ_{C2}, τ_{C3}	The Coulomb friction torque and its predicted value
τ_{CT1}, τ_{CT2}, τ_{CT3}	Torque from the contact force with human head
τ_{F1}, τ_{F2}, τ_{F3}	Friction torque
$\hat{\tau}_{F1}$, $\hat{\tau}_{F2}$, $\hat{\tau}_{F3}$	Predicted value of friction torque
τ_{M1}, τ_{M2}, τ_{M3}	Motor torque
$\tau_{M,HPEA}$, $\tau_{M,HPEA,\max}$	Torque from the electric motor of HPEA and its maximum value
$\tau_{\max 1}$, $\tau_{\max 3}$	Maximum motor torque
τ_{Mjf}, τ_{Mjb} $(j=1,2,3)$	Feedforward and feedback part of the motor torque
τ_{P1}	The torque from the PA
τ_{p1d}	Desired torque from the PA
φ_d	The desired end effector orientation angle
ω_{nd1}, ω_{n_d1}, ω_{n_in1}, ω_{n_m1}, ω_{n_out1}, $\omega_{n\_p1}^{\;2}$	The desired closed-loop natural frequency

ABBREVIATIONS

AWR	Arm withdrawal reflex
CG	Chamber group
CPU	Central Processing Unit
DC	Direct current
EA	Electric actuator
EE	End-effector
HDT	Harmonic drive transmission
HIC	Head injury criterion
HPEA	Hybrid pneumatic electric actuator
HSC	High stiffness controller
LSC	Lower stiffness controller
MaxAE	Maximum absolute error
MIF	Maximum impact force
PA	Pneumatic actuator
PWM	Pulse-width modulation
RMSE	Root mean square errors
SEA	Series elastic actuator
SMC	Sliding mode control

SOA	Switching off the actuator
SSE	Steady-state error
TAO	Turn the actuator off
VEC	Viscoelastic covering
VSEA	Variable-stiffness series elastic actuator
WTA	Withdraw the arm

CHAPTER 1 INTRODUCTION

1.1 Motivation

Robotic arms operating close to people are becoming increasingly common. Industrial applications of these robots include assisting workers with assembly tasks, while non-industrial applications include "assistive robots" for improving the quality of life of older adults and people with disabilities. These applications require robots that combine safety with high performance in terms of their motion control. However, conventional robot designs, actuators and control systems emphasize performance over safety.

Whenever a person is within reach of a robot, there is always a chance that the robot will hit the person. Since brain injuries are the most serious, only collisions with the human head will be studied in this thesis. Although the collision could almost occur anywhere on the robotic arm, the most likely location is its end-effector (EE). Since the EE usually has the largest linear velocity, this collision location will also tend to produce the most serious collision and largest impact force. For these reasons, we assume the collisions take place at the EE. As shown in Figure 1.1.1, two types of impact can occur when the EE hits the head. The first, shown in 1.1.1(a), happens when the person's head can move. This is called an "unconstrained impact". The second case can occur when a human is close to a heavy or fixed structure (e.g., a table or wall) such that they cannot move away from the robot, and their head is fixed when the collision happens. This second case, shown in 1.1.1(b), is called a "constrained impact". Both impact cases will be studied in this thesis.

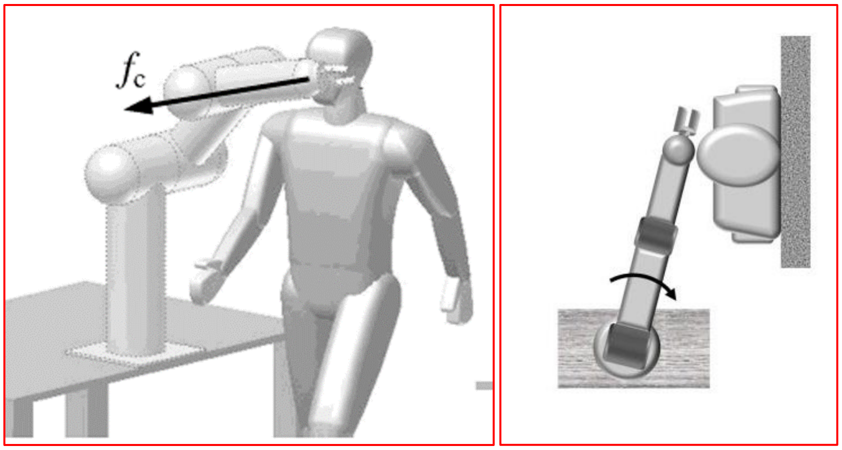

(a) (b)

Figure 1.1.1 (a) Unconstrained impact (Zeng & Bone, 2013a) . (b) Constrained impact (Rouzbeh & Bone, 2018a).

Regarding industrial applications, the safest robot arms designed for industry are known as “collaborative robots” or “cobots”. Cobots can operate at high speeds with payloads up to 10 kg. Almost all cobots employ electric motors. Unfortunately, electric motors suffer from a relatively low torque-to-mass ratio. To create an actuator with enough torque to drive the joints of the robot, they must be coupled with high-ratio transmissions such as gearboxes or harmonic drive transmissions (typically with ratios of 100:1 or larger) (Rouzbeh et al., 2019a). Taking a gearbox as an example, because the moment of inertia at the gearbox output is equal to the motor's inertia multiplied by the transmission ratio squared, the moment of inertia of the output shaft can be very large even with a small motor inertia. As we all know, the torque is equal to the inertia multiplies the angular acceleration. Larger inertia also means larger torque, which makes collisions with the robot more dangerous. The gearbox also increases the friction torque which makes this conventional actuator even less safe.

In contrast, the arms designed for assistive robots are very safe. They achieve this safety by carrying only small payloads at low speeds, and using feedback from expensive torque sensors to make its conventional actuators (i.e., electric motors plus harmonic drive transmissions) safe. For example, the "JACO robot arm" by Kinova costs around $50,000, which makes it unaffordable for most people. So, using conventional actuators has not produced robots which combine safety and performance at a reasonable price.

Unconventional actuators might be the solution for making robotic arms safe and affordable, with similar performance to the conventional actuator. Unconventional robot actuators include:

1. **Series elastic actuator (SEA):** With a SEA, a spring is placed between the output shaft of an electric actuator (consisting of a motor rigidly coupled to a transmission) and the link as shown in Fig 1.1.2 This partially decouples the electric actuator's and link's inertias, which increases the robot's safety. However, the spring also makes a SEA more difficult to precisely control.

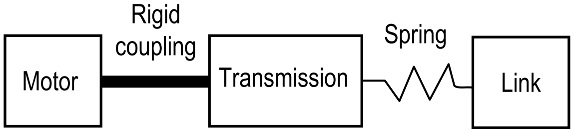

Figure 1.1.2 Structure of a series elastic actuator.

2. **Pneumatic Actuator (PA):** A PA can produce large torques without a gearbox or other transmission, so its inertia is lower than an EA's. This along with the natural

compliance of air makes a PA inherently safer than an EA. The drawback is its slow response, compliance and nonlinear dynamics make it difficult to control precisely.

3. **Hybrid Pneumatic Electric Actuator (HPEA):** A HPEA consists of a PA connected in parallel with an electric motor. It benefits from both by combining the high torque provided by the PA with the fast torque response of the electric motor. Unlike, the conventional EA, the large torque provided by the PA allows a small transmission ratio (or even no transmission) to be used with the electric motor. This keeps the total inertia of the HPEA small, and makes it inherently safer than an EA. The disadvantage of a HPEA is its complex dynamics make precise position control difficult.

Apart from using different actuators, other approaches may be used to reduce the impact force and make the collision less dangerous. Various reaction strategies may be executed after detecting the collision. These include: braking the actuator to a stop, switching the actuator off, and reflexively withdrawing the arm from the location of the impact. Path planners that emphasize safety over path following can also be beneficial. Finally, a simple approach for improving the safety of a robotic arm is to wrap its links with a compliant covering. All of the actuators and approaches mentioned above will be studied in this thesis.

1.2 System Overview

Robotic arms with six joints are the most common type of industrial robot. These joints allow the robot's EE to move with six degree-of-freedom (DOF). The first joint must deal with the largest inertia since it must move almost the entire arm. This means motions involving the first joint are the most likely to cause dangerous collisions like those shown in Figure 1.1.1. Simplifying the problem from a 6-DOF robot to a 1-DOF robot is also expected to yield a better understanding of the actuators and safety approaches, and the roles of their design parameters. For these reasons, a 1-DOF robot whose parameters are mostly derived from the first joint of a 6-DOF industrial robot will be investigated in most of this thesis. To provide more context, the general structure of the control system for the 1-DOF robot is shown in Figure 1.2.1. The desired joint position, velocity and acceleration, as well as the position and velocity feedback, are input to the position controller. The position controller outputs the desired torque and/or the desired pressures (which are required with the PA and HPEA). The inner loop controller controls the actuator's output torque. For the SEA, it uses motor and joint position feedback. For the PA and HPEA it uses pressure feedback. The actuator's output torque minus torque caused by the contact between the robot and head (when that contact occurs) is applied to the robot's link. That link includes the inertia of almost the entire arm, as mentioned earlier. The remainder of the blocks represent the sensors that provide feedback to the controllers.

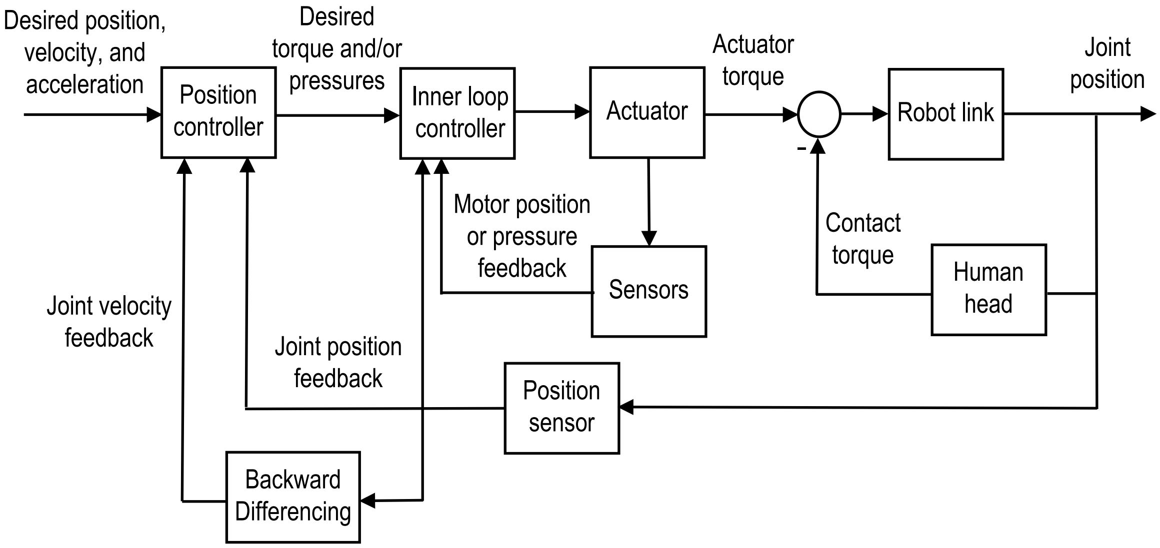

Figure 1.2.1 Structure of the control system for the simplified,1-DOF robot.

1.3 Objectives and Organization

The objective of this thesis is to study and compare various actuators and approaches for improving robot safety. The path tracking performance and impact forces produced by the EA, SEA, PA, and HPEA driving the 1-DOF robot will be studied and compared. The effectiveness of compliant coverings, collision reaction strategies, and an optimal path planner will also be investigated. The research uses computer simulations since doing experiments using the various actuators with a crash test dummy (to emulate the human) was infeasible due to the high cost and time required.

The organization of this thesis is as follows. In chapter 2, the relevant literature is reviewed. In chapter 3, the dynamic models for the robotic arm, actuators and impact between the human head and robot are presented. The controllers for each actuator and the collision reaction strategies are described in chapter 4. The simulations of the actuators and methods for improving safety are presented and discussed in chapter 5. In chapter 6, a novel optimal path planner that makes a trade-off between minimizing a robot's reflected mass and its path following error is introduced. Simulations of a 3-DOF robot are used to evaluate the planner's effectiveness. Finally, the achievements and the limitations of this research, and the recommendations for future work are presented in chapter 7.

CHAPTER 2 LITERATURE REVIEW

2.1 Introduction

The relevant literature is reviewed in this chapter. Papers on unconventional actuators for improving robot safety are reviewed in section 2.2. This section covers the prior research on SEA, PA and HPEA. In section 2.3, literature related to path planning for impact force reduction is reviewed. Research on other approaches for impact force reduction, including compliant covering, and collision detection and reaction, are reviewed in section 2.4. The review's findings are summarized in section 2.5.

2.2 Unconventional robot actuators for improving safety

2.2.1 Series elastic actuators

(Pratt & Williamson, 1995) proposed the SEA. They claimed it has several advantages over the conventional EA, such as shock tolerance, lower reflected inertia, stable force control, energy storage and less damage when it contacts the environment. The last benefit is relevant to applications requiring safety. They proposed a model-based feedforward plus feedback controller for the force control of a linear motion SEA. Their experimental results show that the controller works well at low frequencies. Note that they didn't apply the SEA to robotic arm.

(Bicchi & Tonietti, 2004) proposed a variable-stiffness SEA (VSEA) designed to improve the trade-off between performance and safety for a robotic arm. A tradition SEA has a constant spring stiffness. A VSEA is a SEA whose stiffness can be adjusted while the actuator is moving. As is shown in Figure 2.2.1, they decreased the spring stiffness as the velocity of the robot arm increases. This reduction in stiffness is intended to compensate for the increase in impact force caused by the higher velocity, assuming a collision happens during the "Fast and Soft" part of the trajectory shown in the figure. They quantified the actuator's safety using the standard head injury criterion (HIC). HIC is typically used to measure crash safety in the automotive industry. It is a nonlinear function of the deceleration experienced by a crash test dummy's head during a crash. To quantify the performance, they used the minimum time necessary for the actuator to reach a given target position under safety constraints and actuator saturation. Based on simulations, they found that the effectiveness of the VSEA depends on the available range of compliance at the joint. As the range becomes larger, the performance improves. Compared to the constant stiffness case, when the range of stiffness is 0.2 to1.8 of the centre value, the minimum time decreases by at least 1/8 and at most 1/4. This paper is mainly focused on actuator and only discussed the controller qualitatively. No experiment results are included.

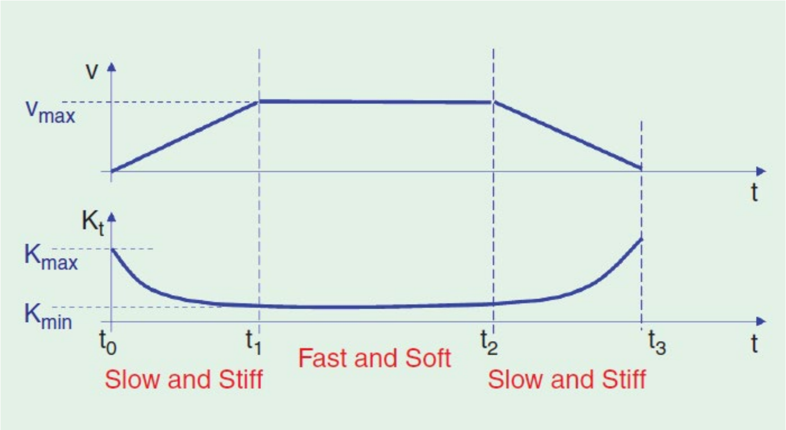

Figure 2.2.1 The intuitive behaviour of a VSEA in a 1-DOF rest-to-rest task (Bicchi & Tonietti, 2004).

(Bae et al., 2010) used gait phase-based smoothed sliding mode control (SMC) for a rotary SEA. SMC is a type of robust control. A controller is called "robust" when it is insensitive to model uncertainties and external disturbances. SMC can cause high frequency variations in the control signal, known as "chattering". Chattering is undesirable in most cases since it can excite unmodelled high frequency dynamics such as higher frequency vibration modes, which will have negative effect on the control performance (Slotine & Li, 1991). Smoothed SMC by utilizing a boundary layer was applied in this paper to make a trade-off between decreasing chattering phenomenon and reducing tracking error. The experimental results show that, in contrast to the case of fixed boundary layer, the torque error reduces around 1/4 in the case of varying boundary layer.

(Sun et al., 2018) proposed a rotational VSEA. Their design features a new mechanism that allows the stiffness to be theoretically adjusted from zero to infinity. It also reduces the complexity of controlling the stiffness by using a linear transmission. A PD feedback and feedforward controller was developed. The prototype's performance was demonstrated in regulation and tracking experiments. Step responses for position variation were performed for different loads (0 and 3 kg) at the 200 N m/rad stiffness condition. Besides, the step response of theoretical stiffness from 30 to 200 N m/rad was investigated for two load conditions. In the second experiment, the overshoot increases around 5.3% in the case with 3 kg load. They also performed sinusoidal tracking experiments. The results indicates that the load significantly influences the tracking accuracies of both the position and theoretical stiffness control. For example, in the simultaneous tracking experiment, the sinusoidal trajectories of the positions for an amplitude of 100° and a stiffness range of 10–110 Nm/rad were determined at 0.5 Hz. The result shows that a 3 kg load makes the root mean square errors (RMSE) increase 0.7° (233%) and 1.6 Nm/rad (133%). Another disadvantage is that the maximum torque of their actuator prototype is only 25 Nm, which is too small to be used with most robotic arms.

2.2.2 Pneumatic actuators

(Zhu & Barth, 2005) presented a method for the impedance control of a linear PA for tasks involving contact and physical interaction. The control method employs an inner loop to control the pressures of the two chambers of a pneumatic cylinder, and an outer loop to enforce an impedance relationship between external forces and motion. They first did pressure tracking and motion tracking experiments in free space. Then they did collision experiments with three different sets of impedance parameter combinations. Position tracking is good for all three cases, and the peak contact force increases as the target inertia of the system is increased. The disadvantage of this paper is that they did not calculate the RMSE of position control or of the pressure control, so quantitative comparisons cannot be performed.

(Toedtheide et al., 2016) presents a novel joint torque-based impedance controller for antagonistically driven flexible joints actuated by pneumatic cylinders. Their mechanical model is shown in Fig 2.2.3. Their control method is similar to Zhu & Barth's paper (Zhu & Barth, 2005), and includes an outer impedance control loop with an inner force control loop. They experimentally tested the tracking performance for sinusoidal signals with frequencies of 0.125, 2, 4, and 7 Hz. The mean absolute errors were 0.021, 0.042, 0.028 and 0.133 rad, respectively. They also studied sudden contacts of the EE with an obstacle during tracking operation. The result shows that the system remained stable when the rigid contact occurred, and was able to proceed with the tracking control after the EE moved away from the obstacle again. However, they did not measure the impacts force, so the safety benefits of their approach are unknown.

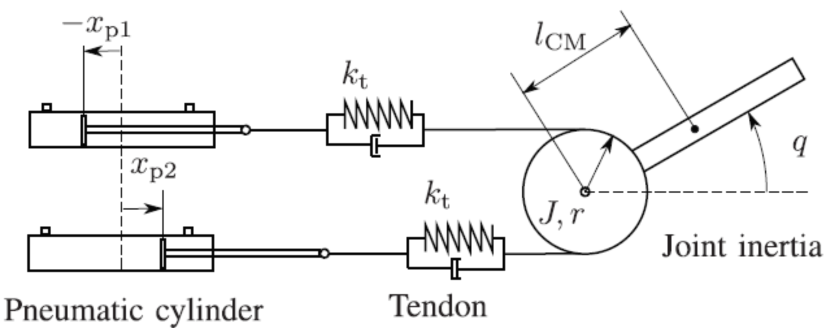

Figure 2.2.2 Mechanical model of the antagonistic flexible pneumatic robot joint (Toedtheide et al., 2016).

(Zheng et al., 2016) used a PA as a VSEA to overcome the disadvantages of common VSEA designs (i.e., complex, heavy, and bulky). The actuator's stiffness is a function of the chambers' air masses and the piston's displacement, so it can be controlled like a variable stiffness spring. They propose a stiffness control approach in which a predictive pressure control algorithm is used to improve pressure control performance while minimizing the valve action. Finally, they performed experiments to determine if the pneumatic VSEA could match the behaviour of an ideal spring with a stiffness of 15 kN/m. The results show that the maximum error is less than 15 N over a force range of -60 to 80 N.

(Rouzbeh et al., 2018a) presents the modeling, controller design, and experimental verification of a high-accuracy position-controlled rotary PA. The outer-loop position control law uses a PD controller with a model-based feedforward term, including an adaptive friction compensator. The inner pressure control loop uses a PID controller with model-based feedforward terms. They also proved the robust stability of the inner and outer subsystems theoretically. Experiments were done to test the performance of pressure control and position control. They defined the chambers of the cylinders that work together as a "chamber group" (CG). The CG that creates the positive torques is termed "CG1" and the CG that creates the negative torques is termed "CG2". For the pressure control of CG1, the RMSE is 0.29% of the max desired pressure, and the maximum absolute error (MaxAE) is 0.71%. The performance with CG2 is similar. For the position control, they did experiments to test the tracking results for sinusoidal reference position trajectories and multiple cycloidal trajectories. For the 1 Hz case, the RMSE and MaxAE were 0.736° and 1.280°, respectively, and for the 0.5 Hz case, the RMSE and MaxAE were 0.299° and 0.547°, respectively. For the cycloidal trajectory, an RMSE of 0.156° and MaxAE of 0.500° were achieved. Finally, they tested the controller robustness to unknown payloads, and measured the tracking error with and without using a payload estimator beforehand. Two alternate payloads were used, one with a 53% decrease, and the other with a 34.7% increase, in the arm's inertia relative to its nominal value. When the payload was light, the RMSE was 4 times larger without the estimator. When the payload is heavy, the RMSE was 2 times larger without the estimator. All of their results show good tracking performance and robustness, but safety is not discussed in this paper.

2.2.3 Hybrid pneumatic electric actuators

The concept of a HPEA first appeared in a 1987 U.S. patent (Petrosky & County, 1987), sponsored by Westinghouse Electric Corp. It was intended to solve the problems of electric motor overheating and low power to weight ratio for high payload applications. This device consisted of an electrical motor and a pneumatic motor connected in parallel. No evidence was found of a commercial device (or even a prototype) being produced. The patent discusses a control algorithm in qualitative terms only.

(Shin et al., 2010) presented the design and control of a rotary HPEA. The design employs a pair of pneumatic artificial muscles connected to the rotary joint using cables and a pulley to form a rotary PA. The EA consists of a small DC motor is connected to the joint by belt which gives a 5:1 transmission ratio. Their controller divided the reference input torque into low frequency and high frequency components. The low frequency component is used as the desired torque for the PA, while the high frequency component is used as the desired torque for the EA. They compared the performance of force control and position control of the HPEA and the PA working alone. With their force control experiments, the PA had a overshoot over 20% and a large steady state error. The HPEA had an overshoot of only around 10% and almost no steady error. With their position control experiments, the desired trajectory is a 6 Hz sine wave with a 5° amplitude. The PA has a tracking error of around 1°. The HPEA reduced this error to around 0.1°. Their results show the performance advantage of the HPEA.

(Rouzbeh et al., 2019b) used a different control method for the HPEA. Their control system is shown in Fig 2.2.5, it consists of an outer position control loop, a pressure distributor, two inner pressure control loops and an inverse motor model. They did experiments with the actuator prototype rotating a link and payload in the vertical plane. For a fast multi-cycloidal trajectory, a root-mean-square error of 0.024° and a steady-state error (SSE) of 0.0045° were achieved. The RMSE reduces around 65% in comparison with the pneumatic actuator and the SSE value is almost 10 times smaller than the best value for HPEAs in other published papers. They also included simulations of a human-robot constrained impact that showed their HPEA produced smaller impact forces than a conventional EA.

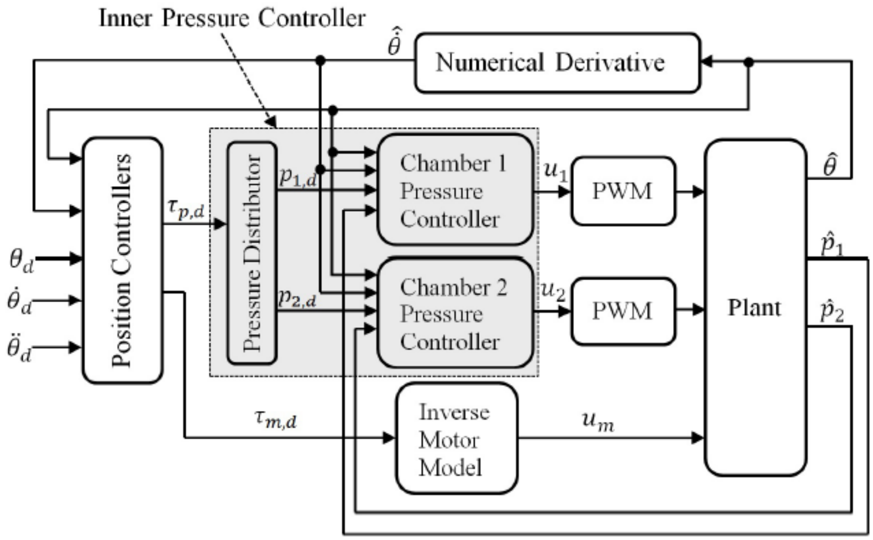

Figure 2.2.3 Control system structure from (Rouzbeh et al., 2019b).

2.3 Path planning for impact force reduction

(Walker, 1990) introduced a model of robotic arm impact dynamics. From the model, they determined that the impact force is a function of three factors, the pre-impact velocity, the geometry of the collision, and the arm's configuration. Regarding the term "configuration", for a robotic arm of the articulated type (which is the most common type) the arm's configuration equals its set of joint angles. Among those three factors, if the manipulator is kinematically redundant then its configuration can be varied for a given EE position. This means its impact force can be reduced without changing the path of its EE in Cartesian space. He proposed several methods to select the configuration that gives the best reduction in the impact force according to his dynamic model. He includes some theoretical results, but does not include any simulation or experimental results.

(Khatib, 1995) introduced the concept of reflected mass, which is the mass perceived during a collision with the EE of a robotic arm. He presented an equation for the reflected mass that shows it is dependant on the configuration of the arm, as well as the mass distributions of its components.

(Kulić & Croft, 2005) presented a strategy for improving the safety of human–robot interaction by minimizing a danger criterion during the planning stage. The danger criterion is the product of an "inertia factor" that approximates the robot's inertia, and a "distance factor" that depends on the distance between the robot and human. Their planning algorithm seeks a path that minimizes a cost function consisting of a quadratic goal seeking function, a quadratic obstacle avoidance function, and the danger criterion. They included simulation results for a 3-DOF robotic arm. These results show that their algorithm produced collision-free paths and small values of the inertia and distance factors. They did not include any simulated collision results or any experimental results.

(Haddadin et al., 2008) demonstrated the influence of robot mass and velocity during blunt unconstrained impacts with humans. They used a crash test dummy in place of a human participant. They performed experiments for different robot masses, robot velocities and impact locations on the dummy. Their results for four different sized robots show the impact forces increasing and the impact durations decreasing for increasing values of the robot's speed. Furthermore, as the robot becomes heavier, the impact forces increase at a faster rate as the velocity is increased. For example, for a DLR-LWRIII robot, the maximum impact force is around 400N at 0.7m/s and increases to around 1000N at 1.5m/s. It increases 150%. For the heavier KUKA KR500 robot, the maximum impact force is around 900N at 0.7m/s and increases to around 2400N at 1.5m/s.

(Kang et al., 2010) proposed an optimization method to reduce impact forces between a mobile manipulator and its environment. Their mobile manipulator combines a 7-DOF robotic arm with 3-DOF mobile base to give it a total of 10 DOF. Since only 6 DOF are required to manipulate the position and orientation of an object in 3D space, this robot has 4 redundant DOF. They use those redundant DOF with an unconstrained optimization method to find the 10 joint angles which balance moving the arm to its minimum effective inertia configuration with keeping those angles far away from their upper and lower limits. Their method assumes that the direction of approach between the mobile manipulator and the environment is known in advance of the collision, which is not always true. They conducted both collision simulations and experiments. After contact, the motions of the arm and its base were controlled by a damping controller to regulate the contact force. In the experiments, the robot's EE was moved at 0.1 m/s into a Styrofoam wall with an approximate stiffness of 40 kN/m. The experimental maximum impact force using their optimization method and damping controller was 120 N, or 50 N less than the 170 N impact force without it.

(Rossi et al., 2015) presented a novel model-based injury index built on the concept of dissipated kinetic energy in a potential inelastic impact. This index depends on the robot reflected mass and velocity in the impact direction. Based on this index, they proposed a control algorithm that allows the robot to perform a given task while bounding the injury assessment and minimizing the reflected mass in the expected direction of the impact at the same time. They compared the impact forces in collision experiments with and without their control algorithm. When the algorithm was active, the maximum impact force was approximately 12% lower than without it.

(Mansfeld et al., 2017) exploited the redundant degrees-of-freedom (DOF) of a joint torque controlled 8-DOF robot. As previously mentioned, a redundant robot can minimize the reflected mass without affecting the desired Cartesian EE trajectory. Their method minimizes the reflected inertia by projecting the gradient of the reflected mass onto the null space of the Jacobian matrix. They found reflected mass extrema that can be obtained by null space motions, and propose a real-time, torque-based redundancy resolution scheme.

They include experimental results showing that the reflected mass is minimized during the robot's motion, but they do not test their method's ability to make collisions safer.

2.4 Other approaches for impact force reduction

2.4.1 Addition of compliant covering

(Yamada et al., 1997) proposed applying a viscoelastic covering (VEC) to cover a robot's links. They modelled the mechanics of contact between the human and robot as shown in Figure 2.4.1. The human body in contact with the VEC is modelled by a semi-ellipsoidal model. Assuming a constant velocity during impact, they derived an equation for the impact force and studied the effects of the VEC's parameters. They did not present any experimental or simulation results showing how much the compliant covering reduces the impact force.

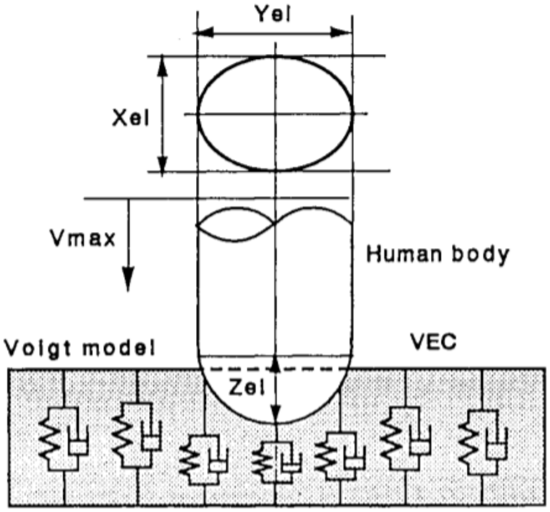

Figure 2.4.1 Model of the contact mechanics of the human and VEC proposed by (Yamada et al., 1997).

(Zeng & Bone, 2013a) investigated the use of a compliant foam covering to reduce impact severity and enhance human safety. They proposed the dynamic model shown in Figure 2.4.2. Using this model, they derived an equation for the impact force. They showed that this equation is suitable for head impacts with impact velocities not exceeding 1.25 m/s. Impact experiments were performed with an apparatus simulating the human head. The maximum error between the predicted and experimental maximum head acceleration results was less than 7%. They presented a procedure for designing the stiffness and thickness of the foam to ensure safe impacts. In their experiments, the maximum head acceleration was within the safety limits, proving the effectiveness of the foam design procedure.

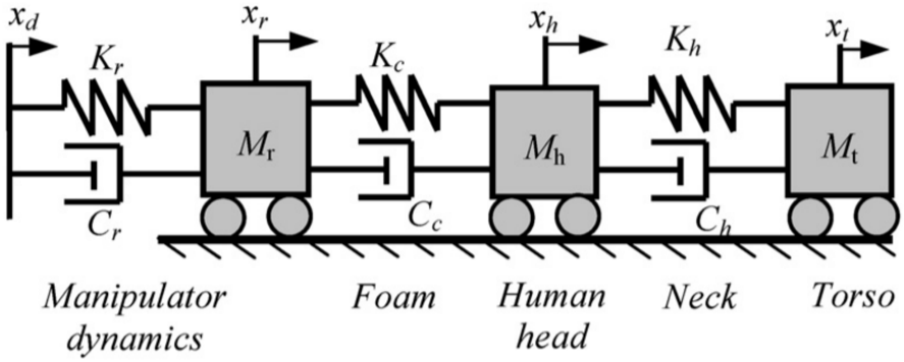

Figure 2.4.2 Normal direction impact dynamic model (Zeng & Bone, 2013a)

2.4.2 Collision detection and reaction strategies

(De Luca et al., 2006) proposed a collision detection method which uses only proprioceptive robot sensors and provides direction information for the safe robot reaction after a collision. They defined a collision detection signal that is a function of the robot's actuator torques, joint velocities, kinetic energy, and gravitational potential energy. The collision is detected when this signal is larger than a threshold chosen based on the noise characteristics of the system. The direction of impact collision force is estimated using a residual torque vector. When the collision is detected, the control law is switched from PD control to a collision reaction controller whose objective is to reduce the residual torque vector to zero which is also supposed to reduce the impact force. They performed experiments using a DLR-III robotic arm colliding with a balloon. The DLR-III is a state-of-the-art research robot. The collision detection times ranged from 5-7 ms. The collision reaction strategy reduced the residual torque from 35 Nm to 0 in about 0.25 s. They did not report any impact force measurements. It is likely that the detection and reaction speeds would be slower with industrial collaborative robots due to their higher values of link inertia and joint friction.

(Han et al., 2017) proposes a collision detection strategy employing the slope of the feedback commanded torque. This strategy is based on their observation that the slope of the feedback commanded torque during collisions is far larger than in the absence of collisions. Collision can be recognized before the contact force achieves its peak. As for the reaction strategy, after a collision is detected the manipulator is commanded to stop like a mass-spring-damper system. Their collision experiments involved a custom-made 1-DOF robot arm hitting a rigid object. The maximum collision detection time was 10 ms. They did not report any impact force measurements and did not compare the performances with and without their reaction strategy. Again, it is likely that the detection and reaction times would be slower with an industrial robot.

(Rouzbeh & Bone, 2018b) studied two different collision reaction strategies. One is switching off the actuator when the impact is detected (SOA) and another is implementing an arm withdrawal reflex (AWR) by applying the maximum actuator torque in the opposite direction. They simulated collisions between a UR5 collaborative robot and a person's constrained head. For the uncovered robot with a high bandwidth, high stiffness controller (HSC), SOA reduced the impact force 19.8% and AWR reduced it 13.9%. For a lower stiffness, lower bandwidth controller (LSC), SOA reduced the impact force of 4.5% and AWR reduced it 11.5%. This paper also mentioned the disadvantage of these strategies is that they require rapid impact detection to be effective.

2.5 Summary

The literature on unconventional actuators, path planners and other methods to reduce the danger of a human-robot collision was reviewed in this chapter. The research on SEAs, PAs and HPEAs shows that each should be safer alternative to conventional EAs, but it is unclear what the improvement in safety would be since very few of those papers report safety measurements, such as impact force results. They do report performance results, such as tracking errors, but these cannot be compared fairly since the desired trajectories and payload carried are different. A study that compares a robotic arm driven by each of these actuators (using the same desired trajectory and payload), and that reports both safety and performance results, would be a new contribution to the literature. Regarding the path planners, the state-of-the-art research by (Kang et al., 2010), (Rossi et al., 2015) and (Mansfeld et al., 2017) shows that path planning can be used to reduce the robot's reflected mass during its motion. This mass reduction will decrease the impact force. However, these planners may only be applied to redundant robots, i.e., spatial robots that have more than six DOF. This makes them impractical since most industrial robots and assistive robots have only six DOF, and increasing the number of DOF makes a robot more expensive. There is an unmet need for a planner that reduces the reflected mass, and can be applied to a robot with six or fewer DOF.

The research on compliant coverings has shown they can reduce the impact force, but more research is needed quantifying how the reduction is when they are used with different actuators. Collision detection and reaction strategies have been shown to be effective at reducing the impact force when the delay is 5 ms, which is the shortest time reported in the literature. This short delay was obtained with a state-of-the-art research robot. Further research is needed to determine the effects of larger delays, and to study the interaction between the actuator type, compliant covering, collision reaction strategy and detection delay.

CHAPTER 3 SYSTEM MODELING

3.1 Introduction

The robot arm model, four actuator models and two models of the impact between the human head and robot are presented in this chapter. These dynamic models are essential for simulating the robot and the collisions between the robot and human so that the robot's safety and performance can be studied. They are also needed to design the model-based controllers that will be presented in Chapter 4.

3.2 Dynamics of the robot arm

The robot arm model is shown in Figure 3.2.1. The robot operates in the horizontal plane. The mass of the link is modelled as one concentrated mass (m_1) located at the EE. $m_{Payload}$ is the mass of the payload carried by the robot. L_1 is the distance from the joint to the EE.

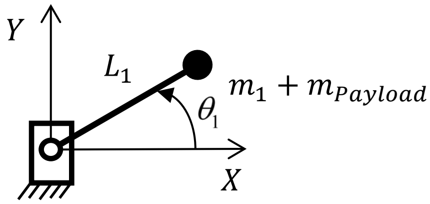

Figure 3.2.1 One-DOF planar robot arm model.

Taking the torques from contact with the human's head (τ_{CT1}) into consideration, the dynamics of the robot arm are given by:

$$\tau_{A1} - \tau_{CT1} = I_{r1}\ddot{\theta}_1 \tag{3.1}$$

where τ_{A1} is the torque from the actuator, I_{r1} is the moment of inertia of the link and actuator, and $\ddot{\theta}_1$ is the joint's angular acceleration. The equation for I_{r1} depends on the actuator being used.

3.3 Actuator dynamic models

3.3.1 Electric actuator

The conventional actuator used with robot joints is an electric actuator (EA) consisting of a DC motor rigidly coupled to a transmission. Typically, the transmission is a harmonic drive transmission (HDT) since they are lightweight and do not suffer from backlash. The structure of the EA is shown in Figure 3.3.1. The desired actuator torque (τ_{A1d}) is input to the motor driver which controls the current such that the motor outputs a torque of τ_{M1}. This torque is multiplied by the HDT gear ratio (R_{g1}) to produce the actuator torque, *i.e.*, $\tau_{A1} = R_{g1}\tau_{M1}$.

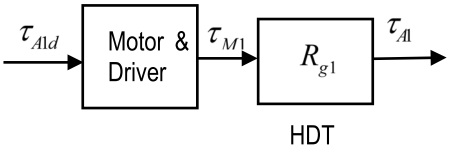

Figure 3.3.1 Structure of the electric actuator.

The HDT also magnifies the friction torque. Since the output shaft of the HDT is rigidly coupled to the link, the motor and link inertias are combined in the dynamics. The motor inertia (J1), friction torque (τ_{F1}), and gear ratio (R_{g1}) are included with the robot dynamics as follows:

$$\tau_{A1} - \tau_{CT1} - \tau_{F1} R_{g1} = I_{r1} \ddot{\theta}_1 \tag{3.2}$$

where the value of I_{r1} for this EA is:

$$I_{r1} = J_1 R_{g1}{}^2 + m_1 L_1^2 \tag{3.3}$$

If inertia matching is used to choose the motor size, then we have: $J_1 = m_1 L_1^2 / R_{g1}{}^2$.

In (3.2), if the friction torque is approximated as a combination of Coulomb friction (representing both static and kinetic friction) and viscous friction, its equation is:

$$\tau_{F1} = \begin{cases} \tau_{C1} & \dot{\theta}_1 = 0 \text{ and } \tau_{M1} > \tau_{C1} \\ -\tau_{C1} & \dot{\theta}_1 = 0 \text{ and } \tau_{M1} < -\tau_{C1} \\ \tau_{M1} & \dot{\theta}_1 = 0 \text{ and } \left|\tau_{M1}\right| \le \tau_{C1} \\ \tau_{C1} \operatorname{sgn}\left(\dot{\theta}_1\right) + C_{v1} \dot{\theta}_1 & \dot{\theta}_1 \ne 0 \end{cases} \tag{3.4}$$

where τ_{C1} is the Coulomb friction torque, and C_{v1} is the coefficient of viscous friction.

3.3.2 Series elastic actuators

The structure of the series elastic actuator (SEA) is shown in Figure 3.3.2. This figure and the equations in this section are based on the theory from (Pratt & Williamson, 1995). With a SEA the rigid connection between the output shaft of the transmission and the link is replaced by a torsional spring so the transmission and link are not rigidly coupled. The dynamics of the link are given by:

$$\tau_{A1} - \tau_{CT1} = I_{r1}\ddot{\theta}_1 \tag{3.5}$$

where the value of I_{r1} for the SEA is:

$$I_{r1} = \mathrm{m}_1 L_1^2 \tag{3.6}$$

Assuming the spring's mass is negligible, the actuator torque is simply:

$$\tau_{A1} = K_{s1}\left(\frac{\theta_{M1}}{R_{g1}} - \theta_1\right) \tag{3.7}$$

where K_{s1} is the spring's stiffness. The acceleration of the motor is given by:

$$\ddot{\theta}_{M1} = \frac{\tau_{M1} - \tau_{F1} - \left(\tau_{A1}/R_{g1}\right)}{J_1} \tag{3.8}$$

where the friction torque can be calculated using (3.4) again.

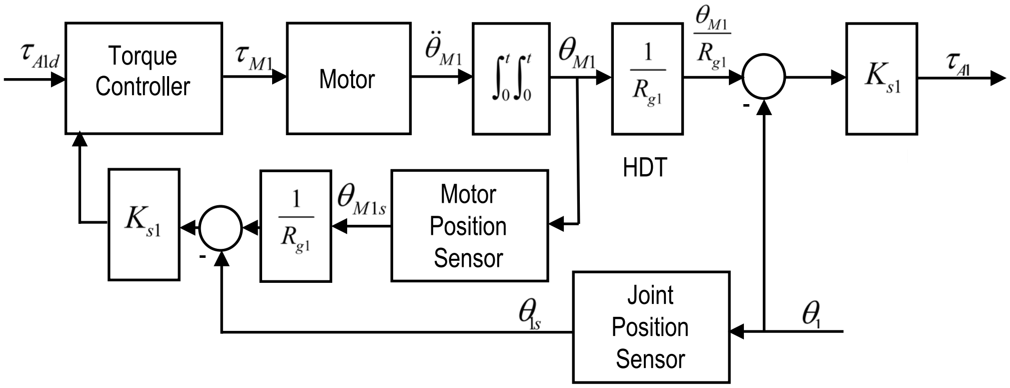

Figure 3.3.2 Structure of the series elastic actuator.

3.3.3 Pneumatic actuator and hybrid pneumatic electric actuator

The equations in this section are based on the models presented in (Rouzbeh et al., 2019c). The dynamic equation for both the PA and HPEA is:

$$\tau_{A1} - \tau_{CT1} - \tau_{F1} = I_{r1}\ddot{\theta}_1 \quad (3.9)$$

For the PA, the inertias of the pistons, rods and gears are negligible compared to the link inertia, so I_{r1} is given by (3.6). Similarly, for the HPEA, the motor is rigidly coupled to the link and its inertia is negligible compared to the link inertia, so (3.6) applies again. The actuator torque is given by:

$$\tau_{A1} = \tau_{P1} + \tau_{M,HPEA} \quad (3.10)$$

where $\tau_{M,HPEA}$ is the torque from its electric actuator and τ_{P1} is the torque from its pneumatic actuator. With the PA, $\tau_{M,HPEA} = 0$. The pneumatic torque for both PA and HPEA is given by:

$$\tau_{P1}=r_p F_p \tag{3.11}$$

where r_p is the pinion gear's pitch radius; F_p is the force given by the pneumatic actuator and:

$$F_p = A_g \left(P_1 - P_2\right) \tag{3.12}$$

where A_g is the total cross-sectional area of each chamber group (CG). P_1 and P_2 are the pressures inside CG1 and CG2.The dynamic equation for each CG is:

$$V_j \dot{P}_j + kP_j \dot{V}_j = \dot{m}_j kRT \quad j \in \{1,2\} \tag{3.13}$$

from this equation the derivative of pressure can be written as:

$$\dot{P}_j = \left(\dot{m}_j kRT - kP_j \dot{V}_j\right) / V_j \quad j \in \{1,2\} \tag{3.14}$$

where $\dot{m}_j$ is the overall mass flow rate into the CGs, *k* is the ratio of specific heats for air, *R* is the universal gas constant, *T* is the air temperature, P_j is the CG pressure, and V_j is the CG volume, which can be derived from:

$$\begin{cases} V_1 = V_{01} + A_g r_p \theta \\ V_2 = V_{02} - A_g r_p \theta \end{cases} \tag{3.15}$$

where V_{01} and V_{02} are CG1 and CG2 volumes at θ=0. Regarding the value of $\dot{m}_j$, assuming air as an ideal gas, $\dot{m}_j$ can be obtained by:

$$\dot{m}_j = A_{vj} \mu_j \quad j \in \{1,2\} \tag{3.16}$$

where A_{vj} is the orifice area for each valve, and according to (Ferretti et al., 2004), μ_j is the pulse-width modulation duty cycle for the supply valve of the associated CG and can be found by assuming an isentropic process through the valve's orifice:

$$\mu_j = \begin{cases} C_1 C_f \dfrac{P_{uj}}{\sqrt{T}} & \dfrac{P_{dj}}{P_{uj}} \le P_{cr} \\ C_2 C_f \dfrac{P_{uj}}{\sqrt{T}} \left(\dfrac{P_{dj}}{P_{uj}}\right)^{1/k} \sqrt{1 - \left(\dfrac{P_{dj}}{P_{uj}}\right)^{(k-1)/k}} & \dfrac{P_{dj}}{P_{uj}} > P_{cr} \end{cases} \quad j \in \{1,2\} \tag{3.17}$$

where P_{uj} is the pressure upstream of the valve, P_{dj} is the down-stream pressure. Assuming the supply pressure (P_S) and atmospheric pressure (P_{atm}) are constant:

$$P_{uj} = \begin{cases} P_s & A_{vj} > 0 \\ P_1 & A_{vj} \le 0 \end{cases} \quad j \in \{1,2\} \tag{3.18}$$

$$P_{dj} = \begin{cases} P_1 & A_{vj} > 0 \\ P_{atm} & A_{vj} \le 0 \end{cases} \quad j \in \{1,2\} \tag{3.19}$$

where C_f is the discharge coefficient of the valve, C_1 and C_2 are dependent on the ideal gas constant and specific heat ratio for air. P_{cr} is the critical pressure ratio that differentiate subsonic and sonic flows in the valve.

Back to the equation of m_j, the orifice area for each valve A_{vj} is given by:

$$A_{vj} = u_j A_{vgain} \quad j \in \{1,2\} \tag{3.20}$$

where u_j are the valve inputs, A_{vgain} is a constant number which equals to 2×10^{-5} m^2/V.

Finally, considering the friction force in the dynamic equation, it is given by:

$$\tau_{F1} = \begin{cases} r_p F_c \operatorname{sgn}\left(\dot{\theta}_1\right) + C_{vf}\dot{\theta}_1 & \dot{\theta}_1 \ne 0 \\ r_p F_p & \dot{\theta}_1 = 0 \wedge \left|F_p\right| < F_s \\ r_p F_s \operatorname{sgn}\left(F_p\right) & otherwise \end{cases} \tag{3.21}$$

where F_c is the Coulomb friction force, F_s is the static friction force, and C_{vf} is the viscous friction force coefficient.

3.4 Collision scenarios and impact dynamics

3.4.1 Constrained impact

A model for the constrained impact scenario described in section 1.1 is presented in this section. A simplified model for the human's head at the impact location is a linear spring with its far end fixed, as is shown in Figure 3.4.1. Since head is the most dangerous part of human, the spring stiffness can be seen as human head stiffness.

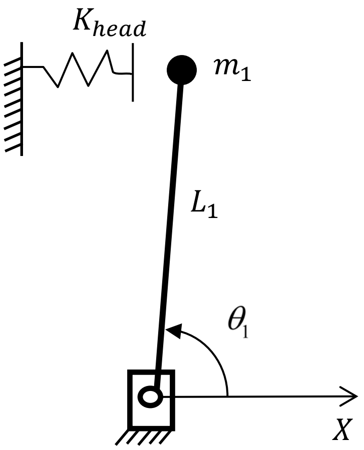

Figure 3.4.1 Human head model for constrained impact.

The following equations are based on the models presented in (Rouzbeh & Bone, 2018c) and (Zeng & Bone, 2013b). Assuming the link is infinitely stiff, the contact force is given by:

$$F_{contact} = \begin{cases} 0 & x_{robot} \geq x_{head} \\ K_{head}\left(x_{head} - x_{robot}\right) & x_{robot} < x_{head} \end{cases} \tag{3.22}$$

where $x_{robot} = L_1 \cos\theta_1$ and x_{head} is the coordinates of head (which corresponds to the right end of the spring in the figure). Assuming the spring's deflection is small, the contact torque for this head location is simply: $\tau_{CT1} = L_1 F_{contact}$.

Another case occurs when a compliant covering made of elastomeric foam is added to the robot. We assume the foam may also be modelled as a spring, with a stiffness of K_{foam}. In this case, when the impact happens, the spring stiffness can be replaced by the stiffness of two springs in series:

$$K_{sum} = \frac{K_{head} K_{foam}}{K_{head} + K_{foam}} \tag{3.23}$$

However, a real compliant covering will have a lower thickness limit where it cannot be further compressed so it becomes effectively rigid. For a compliant covering with an uncompressed thickness of d_{foam}, and a lower thickness limit of $d_{\min}$, the contact force is given by:

$$F_{contact} = \begin{cases} 0 & x_{robot} - d_{foam} \geq x_{head} \\ K_{sum}\left(x_{head} + d_{foam} - x_{robot}\right) & x_{robot} - d_{foam} < x_{head} \wedge d_{foam} - d_p \geq d_{\min} \\ K_{head}\left(x_{head} + d_{foam} - x_{robot} - d_p\right) & otherwise \end{cases} \tag{3.24}$$

where d_p is the compressed thickness of the covering. It is given by:

$$d_p = \min\left(\frac{x_{head} + d_{foam} - x_{robot}}{K_{foam} / K_{head} + 1}, d_{foam} - d_{\min} \right) \tag{3.25}$$

3.4.2 Unconstrained impact

As explained in section 1.1, the second impact scenario studied in this thesis occurs when the robot hits a person's unconstrained head. Since the head can move during the impact, x_{head} is no longer a fixed value, and the model must include the head's mass and the neck dynamics. Using the model from (Zeng & Bone, 2013a), the neck can be simplified as a spring with the stiffness K_{neck} in series with a damper with the damping coefficient C_{neck}, as is shown in Figure 3.4.2. The acceleration of the head is then:

$$\ddot{x}_{head} = \frac{-F_{contact} + K_{neck}\left(x_{head0} - x_{head}\right) - C_{neck}\dot{x}_{head}}{m_{head}} \tag{3.26}$$

where x_{head0} is the equilibrium position of the head and m_{head} is the mass of the head.

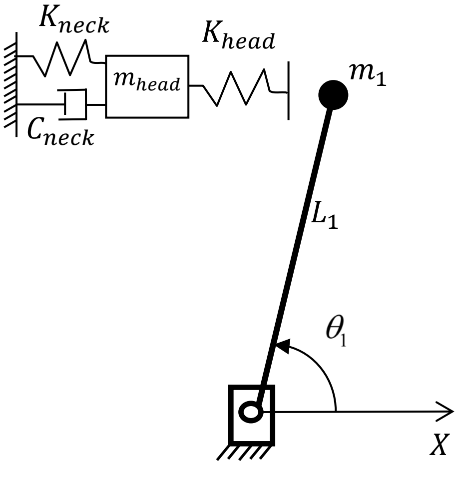

Figure 3.4.2 Human head and neck model for unconstrained impact.

CHAPTER 4 CONTROLLER DESIGN

4.1 Introduction

In this chapter, we present the controllers that will be used with the EA, PA, HPEA and SEA that were modelled in Chapter 3. For the EA, non-model-based and model-based controllers are described. The controllers for the other three actuators are model-based. In the last section, different collision reaction strategies for improving safety are introduced.

4.2 Controllers for the electric actuator

4.2.1 PD controller

The PD controller is a non-model-based controller with the form:

$$\tau_{M1} = K_{p1}\left(\theta_{1d} - \hat{\theta}_1\right) + K_{d1}\left(\dot{\theta}_{1d} - \dot{\hat{\theta}}_1\right) \tag{4.1}$$

where K_{p1} and K_{d1} are its proportional and derivative gains; θ_{1d} and $\dot{\theta}_{1d}$ are the desired joint angle and angular velocity in the trajectory; and $\hat{\theta}_1$ and $\dot{\hat{\theta}}_1$ are the estimated joint angle and joint velocity. The velocity is obtained from the sensed angle by backward differencing. Since the joint angle is measured with an incremental encoder, both the angle and velocity are first order low-pass filtered to reduce the effects of the encoder's quantization noise. The motor's torque is limited as follows: $\left|\tau_{M1}\right| \le \tau_{\max 1}$.

4.2.2 Model-based controller

An inverse dynamics model-based controller will be designed using the dynamic model from Chapter 3. This controller should allow the closed-loop system to achieve faster and more precise trajectory tracking.

As in (Rouzbeh & Bone, 2018c), we can divide the motor torque into two parts. The model-based feedforward part is:

$$\tau_{M1f} = \frac{1}{R_{g1}} \hat{I}_{r1} \ddot{\theta}_{1d} \tag{4.2}$$

where $\hat{I}_{r1}$ is the estimated value of the moment of inertia of the link, and $\ddot{\theta}_{1d}$ is the desired angular acceleration. The feedback part is:

$$\tau_{M1b} = \frac{1}{R_{g1}} \hat{I}_{r1} \left[K_{p1} \left(\theta_{1d} - \hat{\theta}_1 \right) + K_{d1} \left(\dot{\theta}_{1d} - \dot{\hat{\theta}}_1 \right) \right] \tag{4.3}$$

Then the equation for τ_{M1} is:

$$\tau_{M1} = \frac{1}{R_{g1}} \hat{I}_{r1} \left[\ddot{\theta}_{1d} + K_{p1} \left(\theta_{1d} - \hat{\theta}_1 \right) + K_{d1} \left(\dot{\theta}_{1d} - \dot{\hat{\theta}}_1 \right) \right] + \hat{\tau}_{F1} \tag{4.4}$$

where $\hat{\tau}_{F1}$ is the estimated friction torque which is given by:

$$\hat{\tau}_{F1} = \begin{cases} \hat{\tau}_{C1} & \dot{\hat{\theta}}_1 = 0 \text{ and } \tau_{M1} > \hat{\tau}_{C1} \\ -\hat{\tau}_{C1} & \dot{\hat{\theta}}_1 = 0 \text{ and } \tau_{M1} < -\hat{\tau}_{C1} \\ \tau_{M1} & \dot{\hat{\theta}}_1 = 0 \text{ and } \left|\tau_{M1}\right| \le \hat{\tau}_{C1} \\ \hat{\tau}_{C1}\,\mathrm{sgn}\left(\dot{\theta}_1\right) + \hat{C}_{v1}\dot{\hat{\theta}}_1 & \dot{\hat{\theta}}_1 \ne 0 \end{cases} \tag{4.5}$$

In order to tune the controller systematically, some more derivation is necessary. First, after transforming the time domain equations to frequency domain equations, (4.4) can be rewritten as:

$$\tau_{M1} = \frac{1}{R_{g1}}\hat{I}_{r1}\left[s^2\theta_{1d} + K_{p1}\left(\theta_{1d} - \hat{\theta}_1\right) + K_{d1}s\left(\theta_{1d} - \hat{\theta}_1\right)\right] + \hat{\tau}_{F1} \tag{4.6}$$

From chapter 3 we know:

$$\theta_1 = \frac{\tau_{A1}}{I_{r1}s^2} \tag{4.7}$$

Assuming the model is perfect, we have: $I_{r1} = \hat{I}_{r1}$. Combining equation (4.6), (4.7) and $\tau_{A1} = R_{g1}\tau_{M1}$ we obtain:

$$\left(s^2 + K_{d1}s + K_{p1}\right)\left(\theta_{1d} - \theta_1\right) = 0 \tag{4.8}$$

This error equation can be written in the standard 2nd order form: $(s^2 + 2\zeta_d\omega_{nd}s + \omega_{nd}{}^2)E(s) = 0$. Then, comparing (4.8) to the standard 2nd order form, the controller gains can be obtained using:

$$K_{p1}=\omega_{nd1}^{2} \text{ and } \quad K_{d1}=2\zeta_{d1}\omega_{nd1} \tag{4.9}$$

where $\omega_{nd1}=\dfrac{2\pi f_{bw}}{\zeta_{d1}+\sqrt{1+\zeta_{d1}^{2}}}$ is the desired closed-loop natural frequency, ζ_{d1} is the desired closed-loop damping ratio, and f_{bw} is the desired closed-loop bandwidth.

4.3 Controller for the series elastic actuator

The series elastic actuator may be controlled using an outer position control loop with an inner torque control loop. The torque control loop is based on the force control loop presented in (Pratt & Williamson, 1995). The position control loop uses this common PD plus acceleration feedforward controller:

$$\tau_{A1d}=\hat{I}_{r1}\ddot{\theta}_{1d}+K_{dp1}\left(\theta_{1d}-\hat{\theta}_{1}\right)+K_{dd1}\left(\dot{\theta}_{1d}-\dot{\hat{\theta}}_{1}\right) \tag{4.10}$$

where K_{dp1} and K_{dd1} are the proportional and derivative gains of the PD controller. The PD plus torque feedforward and acceleration feedback torque controller is:

$$\tau_{M1}=\frac{\tau_{A1d}}{R_{g1}}+\frac{\hat{J}_{1}R_{g1}}{K_{s1}}\ddot{\tau}_{A1d}+K_{\tau p1}\left(\tau_{A1d}-\tau_{A1}\right)+K_{\tau d1}\left(\dot{\tau}_{A1d}-\dot{\tau}_{A1}\right)+K_{b1}\hat{J}_{1}R_{g1}\ddot{\hat{\theta}}_{1}+\hat{\tau}_{F1} \tag{4.11}$$

where $K_{\tau p1}$ and $K_{\tau d1}$ are the proportional and derivative terms of the PD controller, K_{b1} is a gain that should be made slightly smaller than 1, $\hat{J}_{1}$ is the estimated motor inertia, and $\ddot{\hat{\theta}}_{1}$ is the estimated joint angular acceleration. Note that $\ddot{\hat{\theta}}_{1}$ is calculated by backward differencing and first order low-pass filtering $\dot{\hat{\theta}}_1$; and the motor torque is limited to: $\left|\tau_{M1}\right| \le \tau_{\max 1}$. The estimated friction torque, $\hat{\tau}_{F1}$, is the same as with the EA. The torque derivatives used in (4.11) may be obtained as follows:

$$\dot{\tau}_{A1} = K_{S1}\left(\frac{\dot{\theta}_{M1}}{R_{g1}} - \dot{\theta}_1\right) \tag{4.12}$$

$$\dot{\tau}_{A1d} = \hat{I}_{r1}\dddot{\theta}_{1d} + K_{dp1}\left(\dot{\theta}_{1d} - \dot{\hat{\theta}}_1\right) + K_{dd1}\left(\ddot{\theta}_{1d} - \ddot{\hat{\theta}}_1\right) \tag{4.13}$$

$$\ddot{\tau}_{A1d} = \hat{I}_{r1}\ddddot{\theta}_{1d} + K_{dp1}\left(\ddot{\theta}_{1d} - \ddot{\hat{\theta}}_1\right) \tag{4.14}$$

Note that we did not include the $K_{dd1}\left(\dddot{\theta}_{1d} - \dddot{\hat{\theta}}_1\right)$ term in the $\ddot{\tau}_{A1d}$ equation since the 3rd derivative contains excessive high frequency noise.

In order to tune the controller systematically, a derivation similar to the one done for the EA can be done for the SEA. First, the time domain equations are transformed to frequency domain equations. Then τ_{A1} can be written as:

$$\tau_{A1} = \left[\left(\tau_{M1} - \frac{\tau_{A1}}{R_{g1}}\right)\frac{1}{J_1 R_{g1} s^2} - \theta_1\right] K_{s1} \tag{4.15}$$

τ_{M1} can be written as:

$$\tau_{M1}=\left(\frac{1}{R_{g1}}+\hat{J}_1\frac{R_{g1}}{K_{s1}}s^2\right)\tau_{A1d}+\left(K_{\tau d1}s+k_{\tau p1}\right)\left(\tau_{A1d}-\tau_{A1}\right)+K_{b1}\hat{J}_1R_{g1}s^2\theta_1+\hat{\tau}_{F1} \tag{4.16}$$

Substituting equation (4.16) into (4.15), assuming K_{b1}=1, and assuming we know the motor inertia perfectly (*i.e.*, $\hat{J}_1=J_1$), we obtain:

$$\left(J_1R_{g1}{}^2s^2+K_{s1}K_{\tau d1}R_{g1}s+K_{s1}K_{\tau p1}+K_{s1}\right)\left(\tau_{A1d}-\tau_{A1}\right)=0 \tag{4.17}$$

Equation (4.10) can then be written as:

$$\tau_{A1d}=\hat{I}_{r1}s^2\theta_{1d}+K_{dd1}s\left(\theta_{1d}-\hat{\theta}_1\right)+K_{dp1}\left(\theta_{1d}-\hat{\theta}_1\right) \tag{4.18}$$

From chapter 3, we have:

$$\theta_1=\tau_{A1}\frac{1}{I_{r1}s^2} \tag{4.19}$$

Assuming the model is perfect, combining (4.18) and (4.19) gives:

$$\left(I_{r1}s^2+K_{dd1}s+K_{dp1}\right)\left(\theta_{1d}-\theta_1\right)=0 \tag{4.20}$$

This error equation can be written in the standard 2nd order form: $(s^2+2\xi\omega_n s+\omega_n{}^2)E(s)=0$. Then using (4.17), (4.20), and the standard 2nd order form, the controller gains can be found using:

$$K_{\tau p1} = \frac{J_1 R_{g1} 2\omega_{n\_in1}{}^2 - K_{s1}}{K_{s1} R_{g1}} \tag{4.21}$$

$$K_{\tau d1} = \frac{2 J_1 R_{g1} \xi_{in1} \omega_{n\_in1}}{K_{s1}} \tag{4.22}$$

$$K_{dp1} = \hat{I}_{r1} \omega_{n\_out1}{}^2 \text{ and} \tag{4.23}$$

$$K_{dd1} = 2\hat{I}_{r1} \xi_{out1} \omega_{n\_out1} \tag{4.24}$$

where $\omega_{n\_out1} = \dfrac{2\pi f_{bw}}{\zeta_{out1} + \sqrt{1+\zeta_{out1}{}^2}}$ and $\omega_{n\_in1} = 10\omega_{n\_out1}$.

4.4 Controller for pneumatic actuator and hybrid pneumatic electric actuator

4.4.1 Outer-loop position controller

The pneumatic actuator may be controlled using an outer position control loop with an inner pressure control loop (Rouzbeh et al., 2019d). The PD plus acceleration feedforward position controller is:

$$\tau_{p1d} = \hat{I}_{r1} \ddot{\theta}_{1d} + \hat{\tau}_{F1} + K_{pp1}\left(\theta_{1d} - \hat{\theta}_1\right) + K'_{dp1}\left(\dot{\theta}_{1d} - \dot{\hat{\theta}}_1\right) \tag{4.25}$$

where K_{pp1} and K'_{dp1} are the proportional and derivative terms of the PD controller, and $\hat{\tau}_{F1}$ is obtained using:

$$\hat{\tau}_{F1} = \begin{cases} r_p \hat{F}_c \operatorname{sgn}\left(\dot{\hat{\theta}}_1\right) + \hat{C}_{vf}\dot{\hat{\theta}}_1 & \dot{\hat{\theta}}_1 \neq 0 \\ r_p \hat{F}_p & \dot{\hat{\theta}}_1 = 0 \wedge \left|\hat{F}_p\right| < \hat{F}_s \\ r_p \hat{F}_s \operatorname{sgn}\left(\hat{F}_p\right) & otherwise \end{cases} \tag{4.26}$$

where $\hat{F}_p = A_g(\hat{P}_1 - \hat{P}_2)$.

If hybrid actuator is used, the position controller for the electric actuator is:

$$\tau_{M,HPEA} = K_{pm1}(\theta_{1d} - \hat{\theta}_1) + K_{dm1}(\dot{\theta}_{1d} - \dot{\hat{\theta}}_1) \tag{4.27}$$

where K_{pm1} and K_{dm1} are the proportional and derivative terms of the PD controller, and the torque for the HPEA's motor is limited as follows: $\left|\tau_{M,HPEA}\right| \leq \tau_{M,HPEA,\max}$.

The desired chamber pressures are given by:

$$P_{1d} = \frac{1}{2}(P_{atm} + P_s + \Delta P_{1d}) \tag{4.29}$$

$$P_{2d} = \frac{1}{2}(P_{atm} + P_s - \Delta P_{1d}) \text{ and} \tag{4.30}$$

$$\Delta P_{1d} = \tau_{p1d} / (A_g r_p) \tag{4.31}$$

The pressures from (4.29) and (4.30) may need to be adjusted based on the pressure limits: $P_0 \leq P_{1d} \leq P_s$, and $P_0 \leq P_{2d} \leq P_s$. If P_{1d} reaches the upper limit, we set

$P_{2d} = \max(P_s - \Delta P_{1d}, P_0)$. If P_{1d} reaches the lower limit, we set $P_{1d} = \min(P_0 + \Delta P_{1d}, P_s)$. If P_{2d} reaches the upper limit, we set $P_{1d} = \max(P_s + \Delta P_{1d}, P_0)$. Finally, if P_{2d} reaches the lower limit, we set $P_{2d} = \min(P_0 - \Delta P_{1d}, P_s)$.

In order to tune the controller systematically, similar derivation as the SEA was performed, and the controller gains are given by:

$$K_{pp1} = \hat{I}_{r1} \omega_{n\_p1}{}^2 \tag{4.32}$$

$$K'_{dp1} = 2\hat{I}_{r1} \xi_{p1} \omega_{n\_p1} \tag{4.33}$$

$$K_{pm1} = \hat{I}_{r1} \omega_{n\_m1}{}^2 \text{ and} \tag{4.34}$$

$$K_{dm1} = 2\hat{I}_{r1} \xi_{m1} \omega_{n\_m1} \tag{4.35}$$

where $\omega_{n\_p1} = \dfrac{2\pi f_{bw}}{\zeta_{p1} + \sqrt{1 + \zeta_{p1}{}^2}}$ and $\omega_{n\_m1} = 5\omega_{n\_p1}$.

4.4.2 Inner-loop pressure controller

The equations of the model-based controller of the CG pressures are:

$$\tilde{\dot{P}}_j = P_{jd} + K'_{p1}(P_{jd} - \hat{P}_j) + K_{i1} \int (P_{jd} - \hat{P}_j) dt \quad j \in \{1, 2\} \tag{4.36}$$

$$\dot{m}_{dj} = (K\hat{P}_j \hat{\dot{V}}_j + \tilde{\dot{P}}_j \hat{V}_j) / (KRT) \;\; j \in \{1, 2\} \tag{4.37}$$

where K'_{p1} and K_{i1} are the proportional and integral terms of the PI controller. The inputs to the valves, u_1 and u_2, are obtained by substituting the sensed pressures into (3.17)-(3.19) to get μ_{dj}, and substituting μ_{dj} and $\dot{m}_{dj}$ into:

$$u_j = \frac{\dot{m}_{dj}}{\mu_{dj} A_{vgain}} \quad j \in \{1, 2\} \tag{4.38}$$

where $\left|u_j\right| \le \mathrm{u}_{\text{valvemax}}$ $j \in \{1, 2\}$. Note that (4.38) was derived from (3.16) and (3.20).

Since the inner loop controller is a PI controller instead of a PD controller, the equations for systematically obtaining the controller gains must be derived differently. The inner loop pressure model can be rewritten as follows:

$$\dot{P} = F + G\dot{m} \tag{4.39}$$

where $F = -\frac{KP_j\dot{V}_j}{V_j}$, $G = \frac{KRT}{V_j}$. The equation of the controller is:

$$\dot{m}_d = [\dot{P}_d + K'_{p1}(P_d - P) + K_{i1}\int(P_d - P)dt - \hat{F}]/\hat{G} \tag{4.40}$$

Assuming $\hat{F} = F, \hat{G} = G, \dot{m} = \dot{m}_d$, and substituting (4.40) into (4.39) gives:

$$\dot{P} = \dot{P}_d + K'_{p1}(P_d - P) + K_{i1}\int(P_d - P)dt \tag{4.41}$$

Defining $e_p = P_d - P$ and transforming equation (4.41) to the frequency domain we obtain:

$$(s^2 + K'_{p1}s + K_{i1})E_p(s) = 0 \tag{4.42}$$

Finally, the gains of the inner pressure loop are obtained using:

$$K'_{p1} = 2\xi_{d1}\omega_{n\_d1} \text{ and} \tag{4.43}$$

$$K_{i1} = \omega_{n\_d1}{}^2 \tag{4.44}$$

where $\omega_{n\_d1} = 5\omega_{n\_p1}$.

4.5 Low-pass filter

As mentioned in sections 4.2-4.4, first order low-pass filters, with the transfer function $\frac{1}{\tau_f s + 1}$, are used to reduce the negative effects of encoder quantization noise. The best values of τ_f were dependent on the actuator. For the EA:

$$\tau_f = \frac{0.01}{\omega_{nd1}} \tag{4. 46}$$

For the SEA:

$$\tau_f = \frac{0.1}{\omega_{n\_in1}} \tag{4. 47}$$

For the PA and HPEA:

$$\tau_f = \frac{0.01}{\omega_{n\_p1}} \tag{4.48}$$

4.6 Collision reaction strategies

Collision detection and reaction is another method for potentially reducing the impact force. We will investigate two collision reaction strategies in this thesis. The first strategy is to turn the actuator off immediately after detecting the collision. This strategy will be abbreviated as "TAO". The second strategy is to rapidly withdraw the arm when the collision is detected. This second strategy will be abbreviated as "WTA". These strategies will be used with all of the actuators, but the way they are applied depends on the specific actuator. For the EA and SEA, we set $\tau_{M1} = 0$ when using TAO, and set $\tau_{M1} = -\tau_{\max 1}$ with WTA. For the PA, we set $u_1 = u_2 = -u_{valve\max}$ with TAO; and $u_1 = -u_{valve\max}$ and $u_2 = u_{valve\max}$ with WTA. With the HPEA, we additionally set $\tau_{M,HPEA} = 0$ with TAO, and $\tau_{M,HPEA} = -\tau_{M,HPEA,\max}$ with WTA.

CHAPTER 5 ACTUATOR COMPARISON STUDY

5.1 Introduction

In this chapter, we present a simulation study comparing the safety and performance of different actuators and force reduction strategies. A robot whose first joint is being moved under position control is simulated. Collisions between the robot and a human's head are studied. The maximum impact force (MIF) is used to quantify the robot's safety, and the RMSE (calculated from the tracking errors before the impact occurs) is used to quantify its performance. An overview of the simulation is presented in section 5.2. The sensor noise and model mismatch are described in section 5.3. In section 5.4, we present and discuss the simulation results for the EA, PA, HPEA and SEA actuators; and study the effects of the collision reaction strategies (*i.e.,* TAO and WTA), detection delay, compliant covering stiffness, desired closed-loop bandwidth, and SEA spring stiffness. A summary is provided in section 5.5.

5.2 Simulation overview

The simulation was programmed in Matlab using m code. The desired trajectory used for all of the simulations is shown in Figure 5.2.1. This trajectory is a quintic spline with specified positions, velocities, and accelerations at the following times: 0, 0.5 s, 1 s, 1.5 s, and 2 s. The desired joint angles in radians at these times are: 1.257, 0.785, 0.393, 0.785, and 1.471. The desired joint angular velocities in rad/s at these times are: 0, $\frac{-1.8}{L_1}$, 0, $\frac{1.8}{L_1}$, and $\frac{0.25}{L_1}$. The accelerations at these times are all set as 0. This quintic spline trajectory was chosen since it produces the smooth jerk trajectory that is required by some of the controllers. It was designed to have large accelerations and velocities during the first 2 s to test each actuator's ability to track a challenging motion trajectory. After 2 s, the desired joint velocity is set to $\frac{0.25}{L_1}$ rad/s. The human's head is located such that the collision happens after 2 s. This means the desired linear velocity of the EE will be 0.25 m/s when the collision occurs. The value of 0.25 m/s was chosen since it is the highest speed permitted by the Canadian (CAN/CSA-Z434-14) and international safety standards (ISO 10218-1:2011) when a human is within reach of a robot arm. The default robot parameters and human parameters are listed in Tables 5.1 and 5.2, respectively. The parameters of the EA and SEA; and PA and HPEA are listed in Tables 5.3 and 5.4, respectively. Finally, the default controller parameters are listed in Table 5.5. It is important to note that most of the robot and EA parameters are based on the Universal Robots UR5 robot since it is one of most popular collaborative robots used in industry today. They are specifically for the case of the robot arm being rotated by only its first joint, as was shown in Figure 1.1.1.

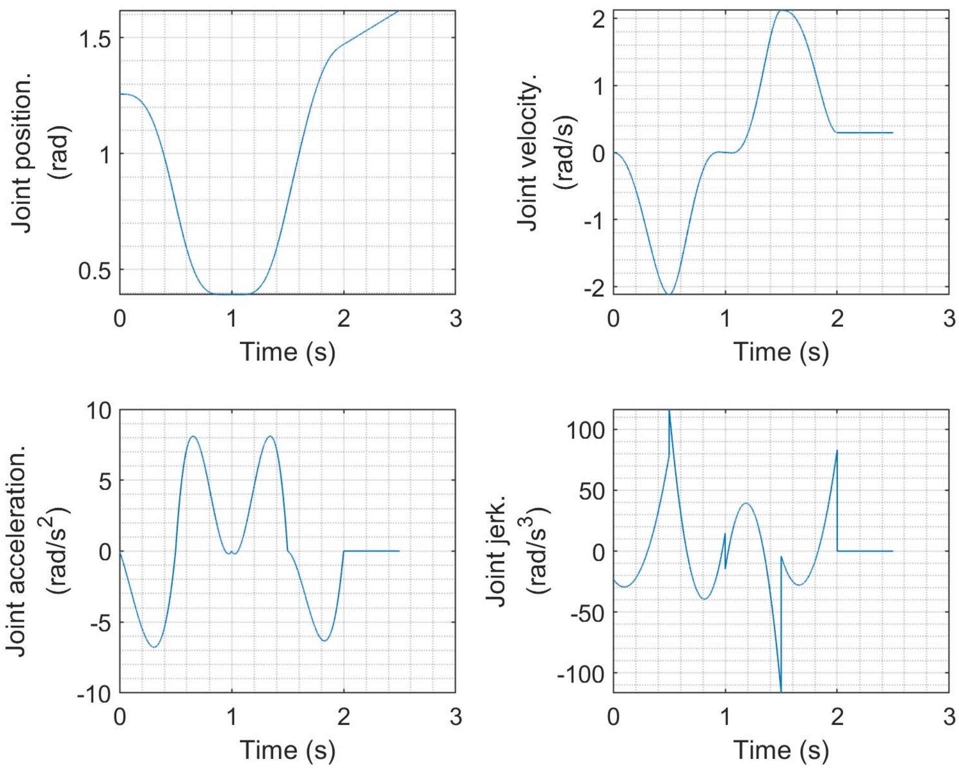

Figure 5.2.1 The desired trajectory.

Table 5.1 Default parameters of the robot.

Parameter	Value	Description
m_1	9.57 kg	Equivalent robot mass for UR5 robot (Rouzbeh & Bone, 2018c)
L_1	0.85 m	Distance from the EE to the rotation axis of the first joint for the UR5 robot (*Universal Robots*, 2015)
$m_{payload}$	3 kg	Payload mass
$m_{PayloadM\text{ax}}$	5 kg	Maximum allowed payload for the UR5 robot (*Universal Robots*, 2015)
$m_{PayloadMin}$	0 kg	Minimum allowed payload for the UR5 robot
d_{foam0}	0.01 m	Initial thickness of compliant covering
$d_{\min}$	0.0025 m	Lower thickness limit of compliant covering
K_{foam}	20 kN/m	Compliant covering stiffness
t_d	25 ms	Collision detection delay

Table 5.2 Parameters of the human.

Parameter	**Value**	**Description**
K_{head}	150 kN/m	Head stiffness (ISO/TS 15066, 2016)
K_{neck}	5 kN/m	Neck stiffness (Viano, 2003)
C_{neck}	130.2 Ns/m	Neck damping coefficient (Viano, 2003)
m_{head}	4.4 kg	Head mass (Willinger et al., 2005)

Table 5.3 Parameters of the EA and SEA.

Parameter	**Value**	**Description**
R_{g1}	100	HDT transmission ratio (*Universal Robots*, 2015)
$\tau_{\max 1}$	1.5 Nm	Motor torque limit (*Universal Robots*, 2015)
τ_{C1}	0.165 Nm	UR5 Coulomb friction torque (Rouzbeh & Bone, 2018c)
C_{v1}	0.004 Ns	UR5 coefficient of viscous friction (Rouzbeh & Bone, 2018c)
K_{s1}	20 kN/rad	Spring stiffness of SEA

Table 5.4 Parameters of the PA and HPEA.

Parameter	Value	Description
P_{atm}	100 kPa	Atmospheric pressure
P_s	700 kPa	Supply pressure (6 bar gauge pressure)
r_p	0.0315 m	Pitch radius of pinion gear (Rouzbeh et al., 2018b)
k	1.4	Ratio of specific heats for air
R	287 J/kgK	Universal gas constant
T	293 K	Air temperature
A_g	0.0072 m^2	Total cross-sectional area of each CG[a]
V_{01}	7.23×10^{-4} m^3	CG1 volume at θ=0[a]
V_{02}	6.14×10^{-4} m^3	CG2 volume at θ=0[a]
$\tau_{M,HPEA,\max}$	11.6 Nm	HPEA motor's maximum torque[b]
u_{valvemax}	1	Maximum value of the valve input[c]
C_f	0.5393	Valve coefficient used in (3.17)[c]
C_1	0.040418	Valve coefficient used in (3.17)[c]

C_2	0.156174	Valve coefficient used in (3.17)[c]
P_{cr}	0.528	Critical pressure ratio that differentiates subsonic and sonic flows in the valve[c]
A_{vgain}	2×10^{-5} m^2/V	Valve gain factor[c]
F_c	104 N	Coulomb friction force[a]
F_s	144 N	Static friction force[a]
C_{vf}	355 N/m/s	Viscous friction force coefficient[a]

a. For a SMC CQ2A50TN-50DMZ-XB9 cylinder.
b. For a MTI Torque Systems, T0852J0001, brushless servomotor.
c. For an Enfield LS-V05s proportional valve connected to each chamber.

Table 5.5 Default parameters of the controllers.

Parameter	Value	Description
f_{bw}	3 Hz	Desired closed-loop bandwidth
T_c	0.001 s	Sampling period
ξ , ξ_{out1} , ξ_{in1} , ξ_{p1} , ξ_{d1} and ξ_{m1}	0.7	Damping ratio
dt	0.0001 s	Integration timestep

5.3 Sensor noise and model mismatch

To make it more realistic, the simulation includes joint angle encoder quantization noise; pressure sensor noise (with the PA and HPEA); and mismatches between the model used by the model-based controllers and the simulated robot. Specifically, mass mismatch and friction mismatch are included.

The chosen encoder is a QR-12 optical encoder made by Quantum Devices. It is a high-resolution encoder, with a resolution of 80,000 counts/rev. Its quantization noise is simulated by setting $\theta_{sensed} = \left(2\pi/80,000\right) round\left(\left(80,000/2\pi\right)\theta\right)$ where θ_{sensed} is the sensed joint angle, θ is the joint angle, and *round* is the standard rounding function. Regarding the pressure sensors, the sensed pressures are obtained by adding 0.1% uniformly distributed random noise to the ideal pressures. This noise level is typical for the sensors used with PA and HPEA (Ashby, 2015).

As for the mass mismatch, the source of the uncertainty is assumed to be the uncertain of the mass of the payload. The estimated value of the moment of inertia of the link and actuator used by the model-based controllers is derived as follows:

$$I_{r\max} = \begin{cases} J_1 {R_{g1}}^2 + m_1 {L_1}^2 + m_{PayloadMax} {L_1}^2 & \text{EA} \\ m_1 {L_1}^2 + m_{PayloadMax} {L_1}^2 & \text{PA, SEA, and HPEA} \end{cases} \tag{5.1}$$

$$I_{r\min} = \begin{cases} J_1 {R_{g1}}^2 + m_1 {L_1}^2 + m_{PayloadMin} {L_1}^2 & \text{EA} \\ m_1 {L_1}^2 + m_{PayloadMin} {L_1}^2 & \text{PA, SEA, and HPEA} \end{cases} \tag{5.2}$$

$$\hat{I}_r = \sqrt{I_{r\max} I_{r\min}} \tag{5.3}$$

where $m_{PayloadM\text{ax}}$ and $m_{PayloadMin}$ are the maximum and minimum allowed payloads for the UR5 robot.

Finally, for friction mismatch the friction parameters used by the model are 25% smaller than the values used by the plant. Specifically, for the electric motor and SEA, $\hat{\tau}_{C1}$ is estimated as $0.75\tau_{C1}$, $\hat{C}_{v1}$ is estimated as $0.75C_{v1}$; and for PA and HPEA, $\hat{F}_c$, $\hat{F}_s$ and $\hat{C}_{vf}$ are estimated as $0.75F_c$, $0.75F_s$ and $0.75C_{vf}$.

5.4 Simulation results and discussion

Various simulation results will be presented and discussed in this section. All of the simulations include sensor noise, mass mismatch, friction and friction mismatch.

5.4.1 Actuator and controller comparison

In this section, the RMSE and MIF of the four actuators using the default parameters are compared. The results are listed in Table 5.6. Constrained and unconstrained impact cases will both be discussed.

Table 5.6 Actuator and controller comparison for the default parameters.

Actuator	**Controller**	**RMSE (rad)**	**MIF for constrained case (N)**	**MIF for unconstrained case (N)**
Electric	PD	0.0057	519	211
	Model-based	0.0017	470	193
SEA	Model-based	0.0025	346	179
Pneumatic	Model-based	0.0121	334	174
HPEA	Model-based	0.0021	351	181

From the table, we can see that the MIF values for the unconstrained case are much less than for the constrained case. Since it is clearly more dangerous, we will use the constrained case for the rest of the simulations in this thesis.

The RMSE of the EA with the PD controller is larger than with the model-based controller. Since the MIF with the model-based controller is also around 10% smaller, only this controller will be used with the EA in the rest of this chapter.

The MIF values with the other actuators are almost the same and are around 27% smaller than the EA with the model-based controller. The MIF of the PA is the smallest, but its RMSE is also the biggest, *i.e.*, 7.1 times larger than the RMSE of the EA. Unlike the PA, the RMSE of the SEA and HPEA are the same order of magnitude as with the EA.

To allow more detailed comparisons, the joint position, position error, velocity error, friction torque, actuator torque, and impact force are plotted vs. time in Figures 5.4.1-5.4.6. Note that the initial contact between the robot and human's head occurs at about 2.2 s. The results for the PD control and model-based control of the EA with the constrained impact case are shown in Figures 5.4.1 and 5.4.2. For comparison purposes, the results for model-based control of the EA with unconstrained impact are given in Figure 5.4.3.

Comparing Figures 5.4.1 and 5.4.2, in addition to having larger magnitudes of position and velocity errors, the velocity errors with the PD controller contain more high frequency oscillations. The torque for the PD controller also contains more high frequency oscillations. Based on these results, the PD controller is more sensitive to high frequency sensor noise than the model-based controller.

Comparing Figures 5.4.2 and 5.4.3, apart from the reduction in the MIF that happens, another noticeable difference is that the impacts occur more frequently after the initial impact with the unconstrained case. This is understandable since some of the robot's momentum is transferred to the human's head when it is unconstrained, so the robot will rebound less before continuing to move forward and repeat the contact.

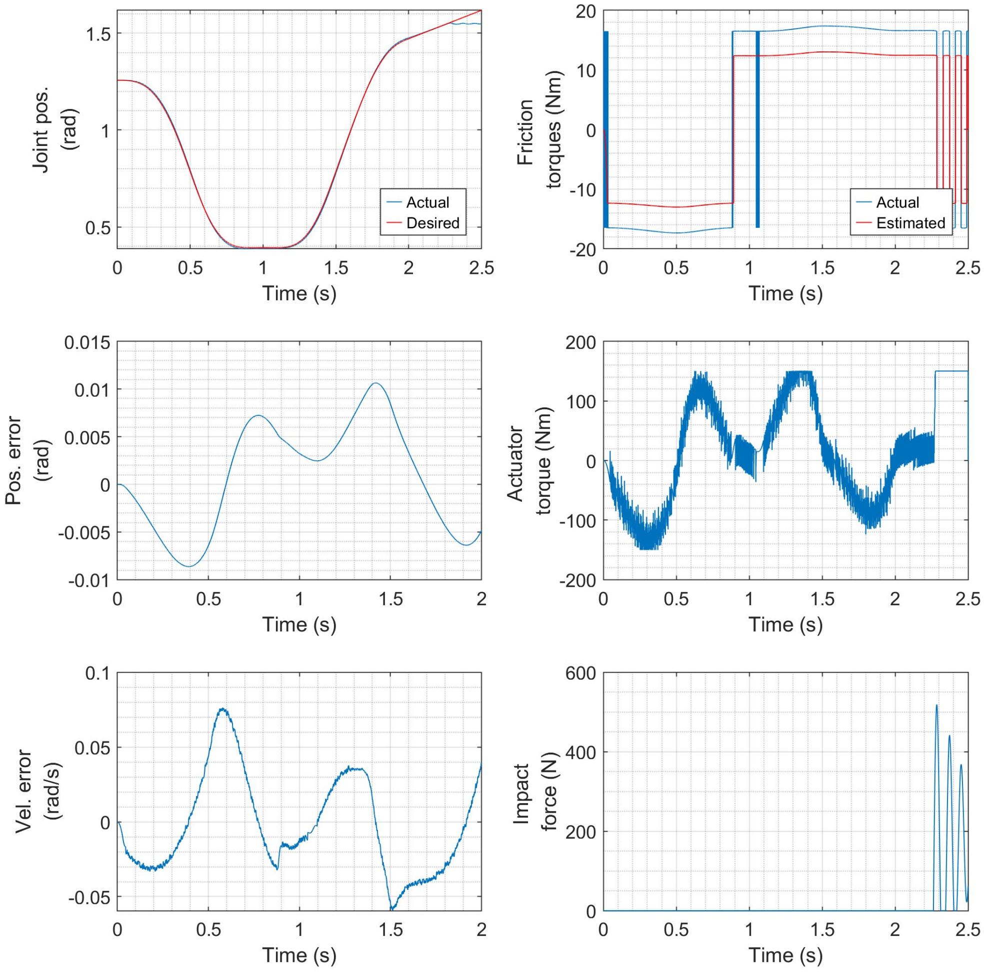

Figure 5.4.1 Results for the EA with PD controller and constrained impact case.

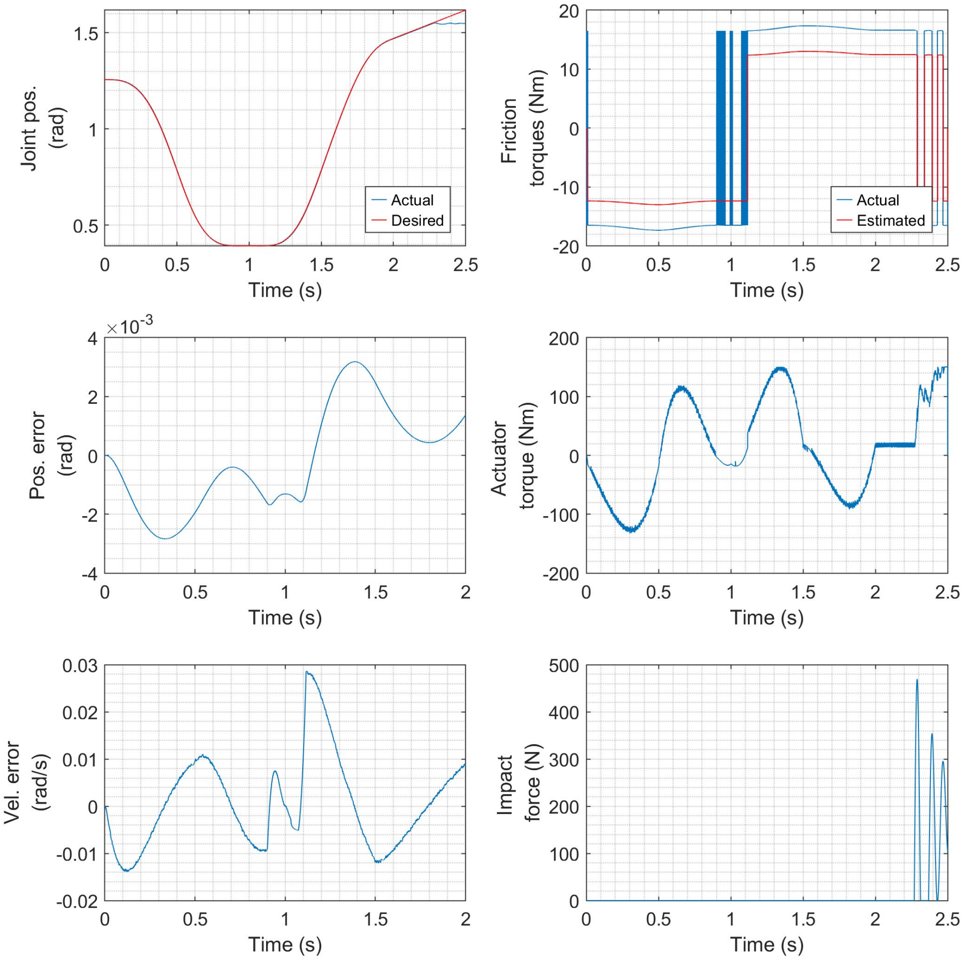

Figure 5.4.2 Results for the EA with model-based controller and constrained impact case.

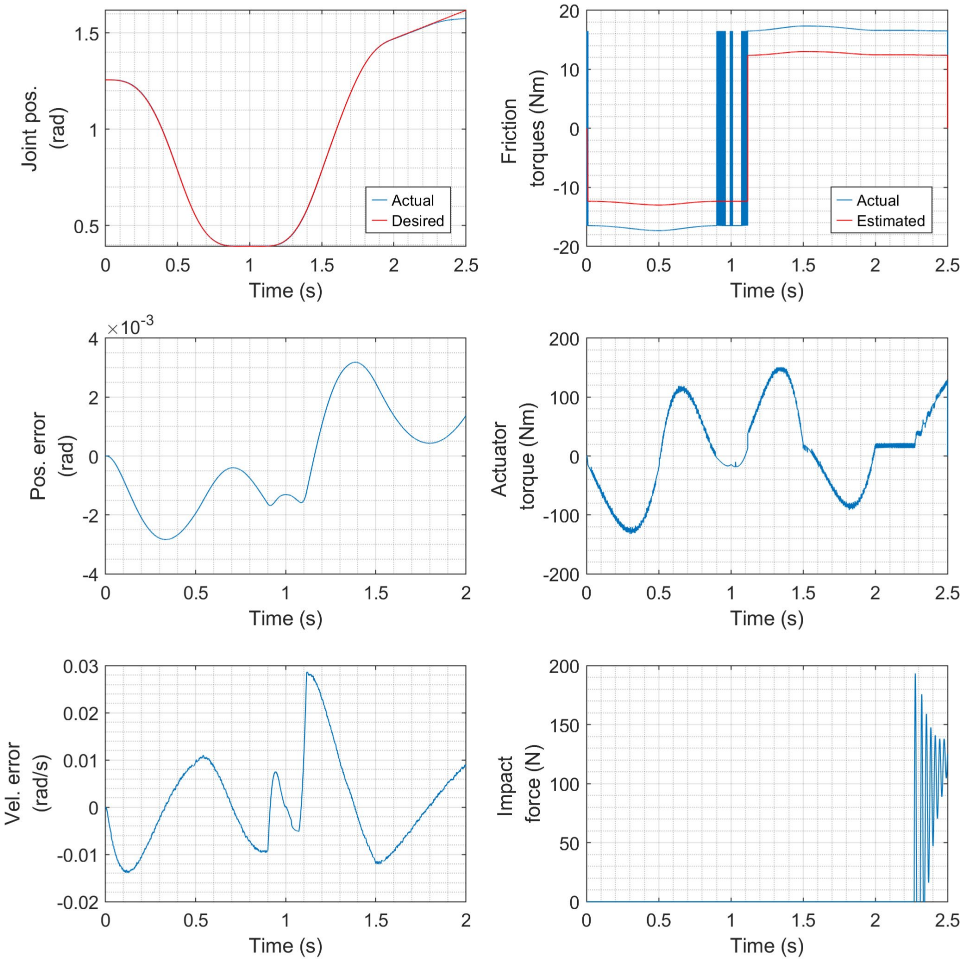

Figure 5.4.3 Results for the EA with model-based controller and unconstrained impact case.

The results for the SEA with a constrained impact are plotted in Figure 5.4.4. The position errors have a similar trend to those shown in Figure 5.4.2, but are larger in magnitude. Unlike the previous figures, the middle right plot shows the torque of the EA (that is part of the SEA, and includes the gain of 100 provided by the HDT) and the torque produced by the spring; and the bottom left plot is the torque error of the SEA's torque control loop. Although the motor torque has a large amount of high frequency oscillation, the spring torque that drives the arm is quite smooth. The maximum torque error is 6.8 Nm, or less than 9% of the maximum torque produce by the spring, which shows that the torque control loop is working reasonably well.

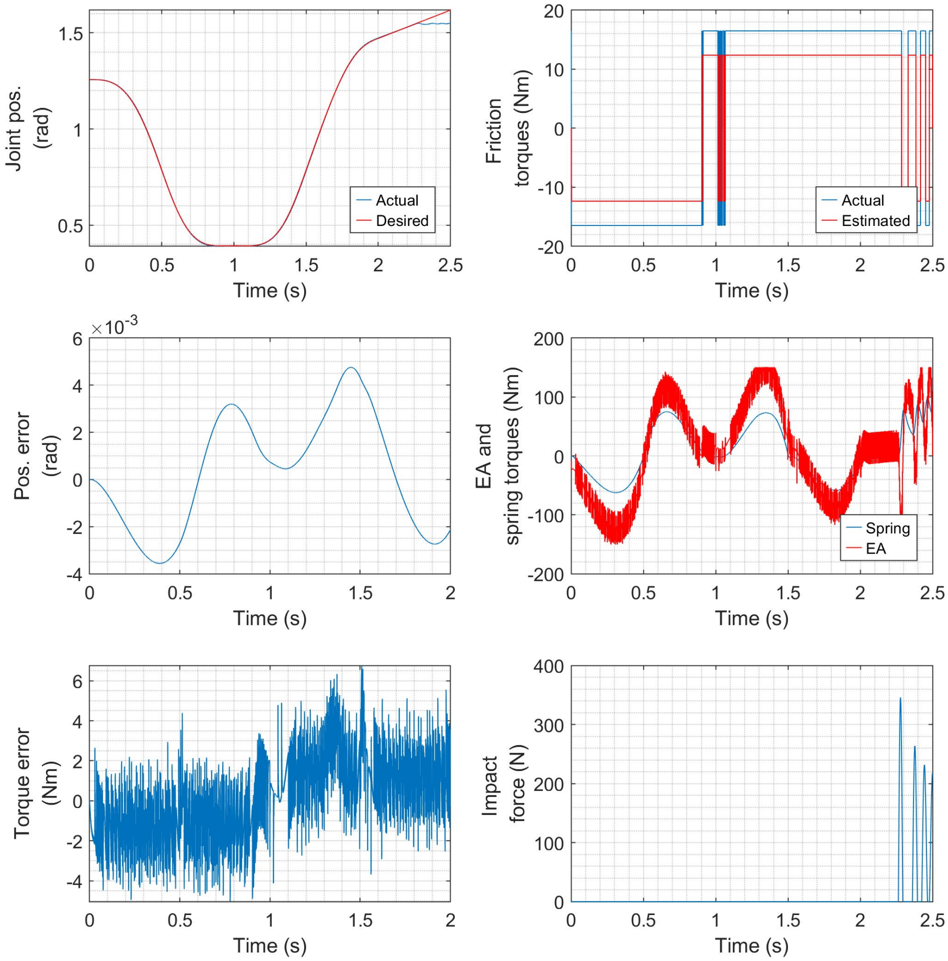

Figure 5.4.4 Results for the SEA with model-based controller and constrained impact case.

Results for the PA and HPEA with the constrained case are shown in Figures 5.4.5

and 5.4.6, respectively. Compared to the previous figures, the middle right plot has been replaced by the pneumatic torque (and electric torque for the HPEA only), the lower left plot shows the desired and sensed pressures for the two CGs, and the bottom two plots show the desired and actual mass flowrates through the valves. From the pressure and mass flowrate plots, it can be seen that the largest pressure errors occurred when the differences between the desired mass flowrate (calculated by the inner loop pressure controller) and the actual mass flow (achievable by the valve) were also large. The largest position errors also occurred at around the same times as the largest pressure errors. These errors could be reduced in future by selecting larger valves, with the drawback that large servo valves are costly. As expected from its RMSE value, the position error plots show that the errors with the PA are much larger than with the EA and SEA. The HPEA has smaller position errors, and the magnitude and trend of the errors are similar to the SEA's. It important to note that this similar performance was achieved even though the maximum friction torques with the HPEA are about 2 times larger than with the SEA due to the cylinders' seal friction. Regarding the HPEA torque, even though the electric motor contributes only about 1/8 of the total torque as the plot shows, its contribution greatly reduced the position errors.

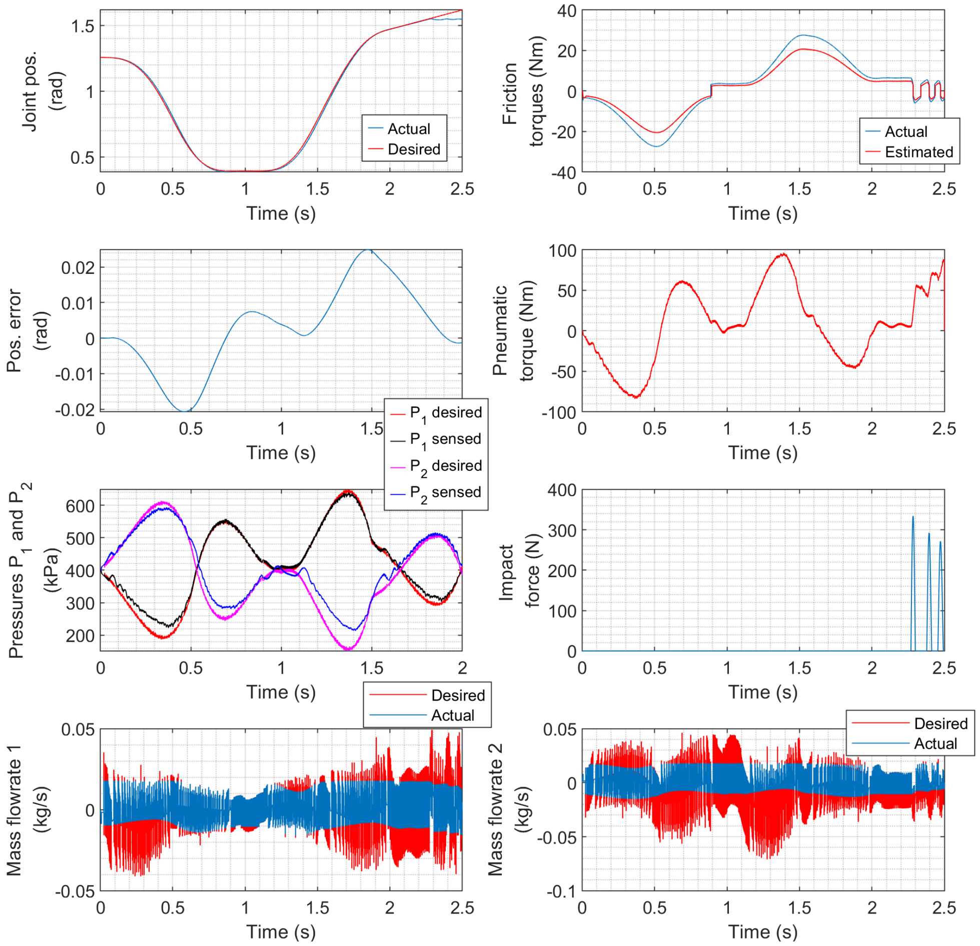

Figure 5.4.5 Results for the PA with model-based controller and constrained impact case.

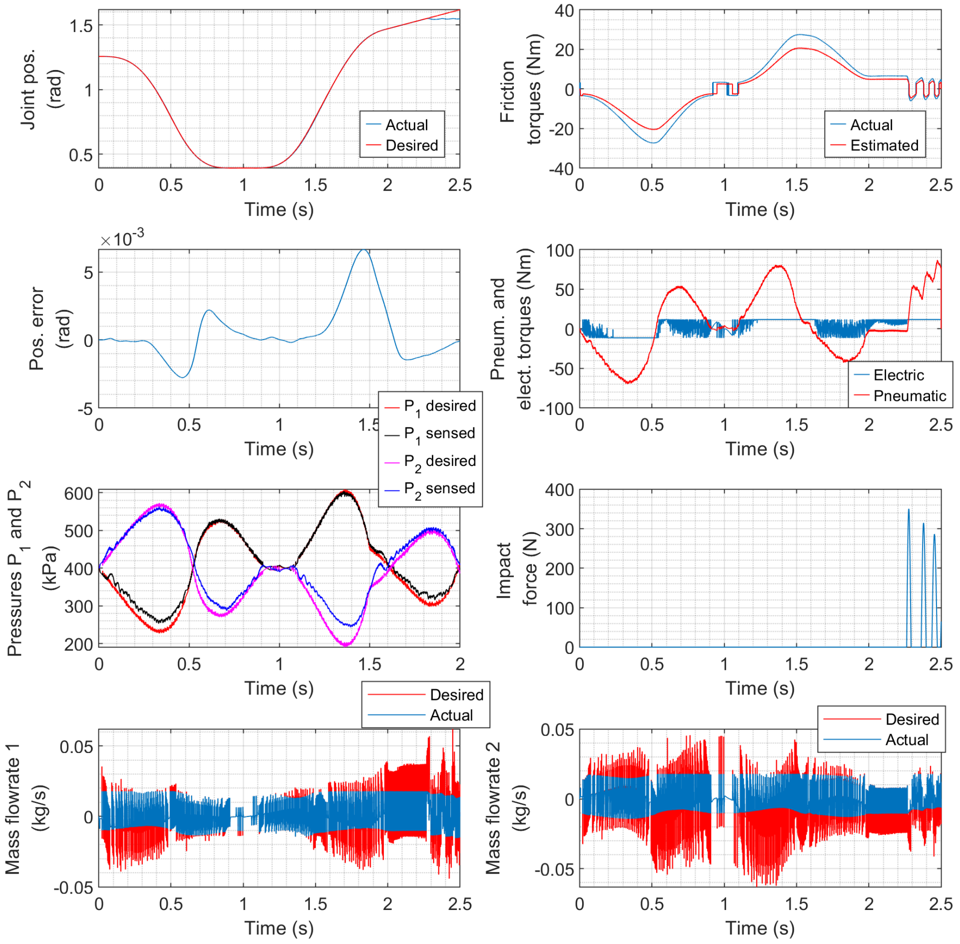

Figure 5.4.6 Results for the HPEA with model-based controller and constrained impact case.

5.4.2 Collision reaction, detection delay and compliant covering stiffness comparison

The ISO standard TS 15066:2016 lists the impact force limit for avoiding injuries to a person's head as 130 N (ISO/TS 15066, 2016) As is shown in the previous section, with all of the actuators the MIF is much larger than this limit. In this section, we will investigate the effects of adding collision reaction strategies, without/with a compliant covering and with different detection delays, on the MIF.

We will study the EA first. As shown in Table 5.7, adding compliant covering can reduce the MIF greatly. When there is no collision reaction, the MIF reduces 39.4% after adding compliant covering. When the detection delay is only 5 ms and no compliant covering is used, WTA is also an effective method which reduces the MIF by 20.6%. Under the same conditions, TAO is less effective and only reduces the MIF by 4.9%.

The results in the table also show that the effectiveness of collision reaction is very dependent on the detection delay. Without compliant covering, when the detection delay is 25 ms or longer, these reaction methods do nothing to reduce the MIF.

However, the MIF results in the rightmost column of the table show that adding compliant covering can reduce the negative effect of detection delay and make the collision reaction strategy more effective. From these results, when the detection delay is 5 ms, TAO reduces the MIF by 50.5% and WTA reduces the MIF by 74.7%. When the detection delay is 25 ms, TAO reduces the MIF by 39.3% and WTA reduces the force by 55.4%. Even when the detection delay is 50 ms, both methods still reduce the MIF slightly.

Table 5.7 Collision reaction, detection delay and compliant covering comparison for the EA.

Actuator	Collision Reaction	Detection Delay (ms)	MIF (N) (without compliant covering)	MIF (N) (with compliant covering)
EA	None	5	470 (case 7.1)	285 (case 7.3)
		25		
		50		
	TAO	5	447	141
		25	470	173
		50	470	277
	WTA	5	373	72
		25	470	127
		50	470 (case 7.2)	270 (case 7.4)

To better understand the connection between the collision reaction, detection delay and compliant covering, the EA torque and impact force plot after 2 s will now been examined. We chose the four cases indicated in Table 5.7 and plot their torques and impact forces in Figures 5.4.7-5.4.10. Please note that the plots of the EA torques and SEA motor torques include the gain of 100 provided by the HDT.

As shown in Figures 5.4.7 and 5.4.8, when there is no compliant covering, the entire first impact lasts about 44 ms. So, if the detection delay is 50 ms, the collision reaction is too late to alter the first impact. However, we cannot say that using the collision reaction method is totally useless because it still stops the second, third impact and so on. Figures 5.4.9 and 5.4.10 show that adding compliant covering extends the duration of the first, and subsequent, impacts. This is reasonable because during the impact phase, the kinetic energy of the arm plus the work done by the actuator is transformed into the elastic potential energy of the skull and the robot. When the impact force peaks all of the kinetic energy has gone into that deformation. When there is no compliant covering that impact duration is short because the skull's stiffness is large. When the compliant covering is added to the robot, we have two springs are in series, and the equivalent stiffness is much smaller than the skull's stiffness. That lower stiffness increases the duration of impact. Since the initial kinetic energy hasn't changed, the area under the force vs. time curve is constant, so the increased impact time decreases the maximum impact force. Figures 5.4.9 and 5.4.10 show that the extended impact duration allows the collision reaction to reduce the MIF from 285 N to 270 N even though the detection delay is 50 ms.

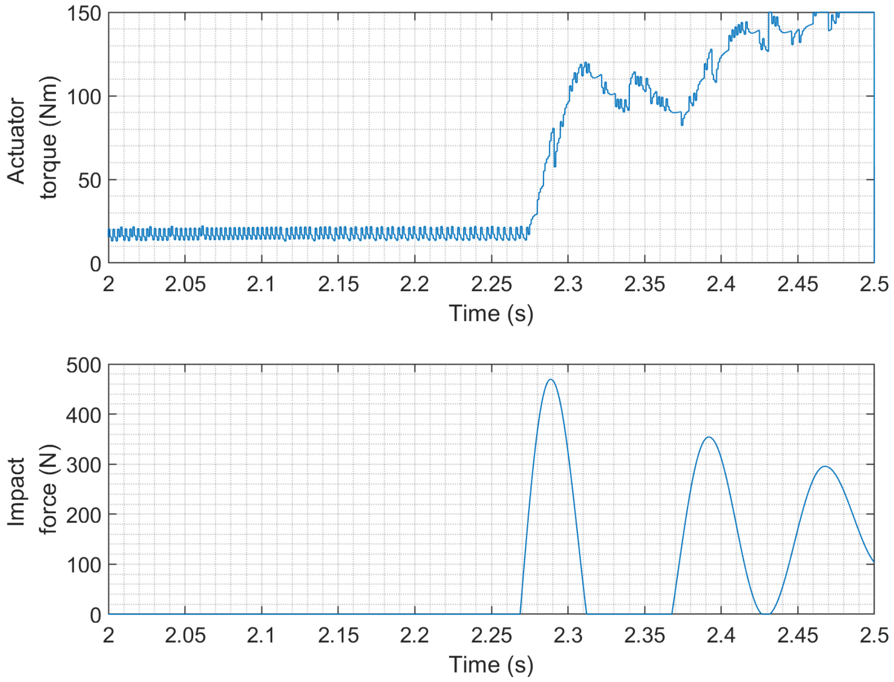

Figure 5.4.7 Motor plus HDT torque and impact force after 2 s of EA case 7.1.

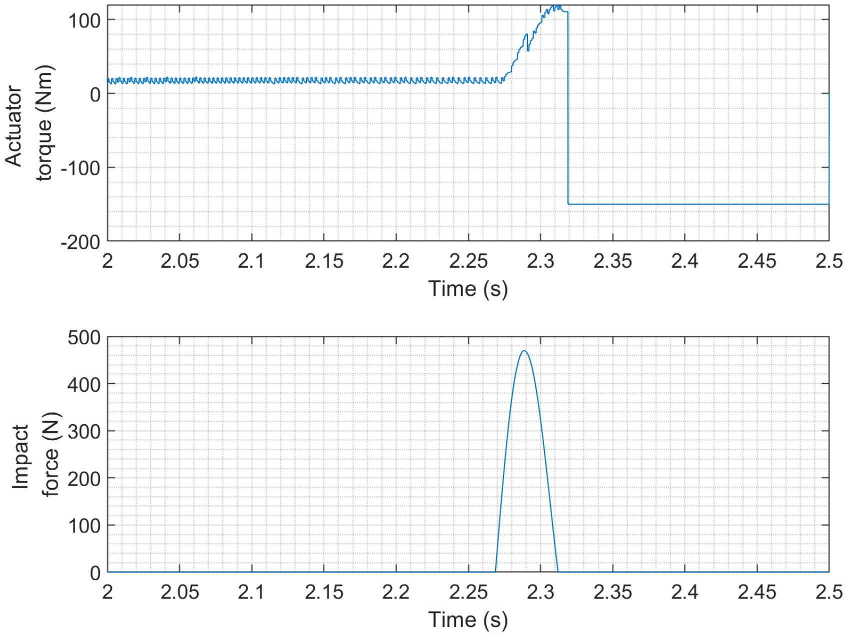

Figure 5.4.8 Motor plus HDT torque and impact force after 2 s of EA case 7.2.

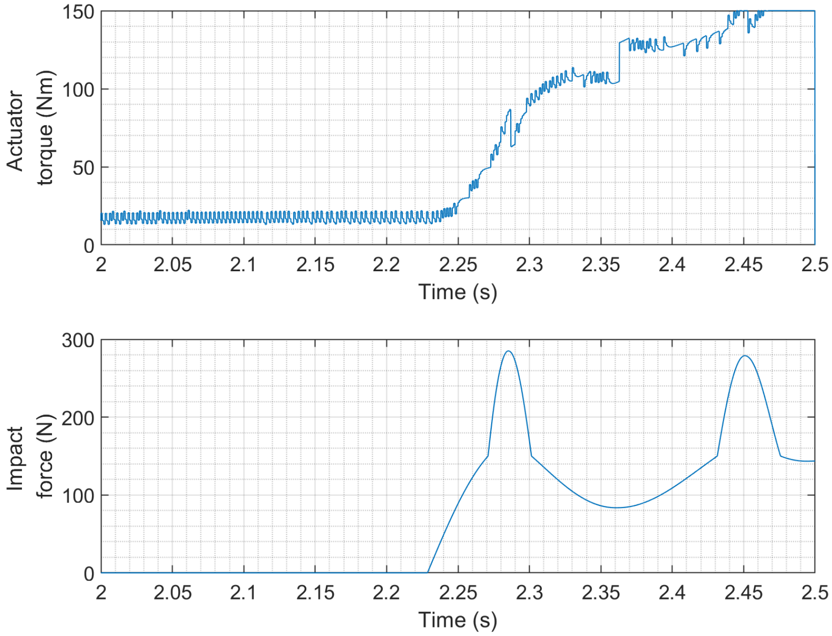

Figure 5.4.9 Motor plus HDT torque and impact force after 2 s of EA case 7.3.

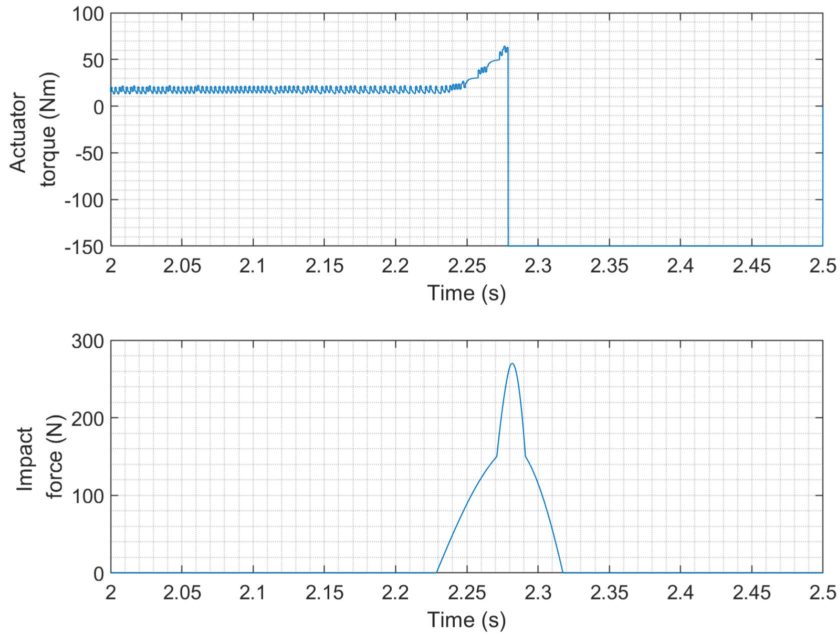

Figure 5.4.10 Motor plus HDT torque and impact force after 2 s of EA case 7.4.

Since adding compliant covering was so effective with the EA, we will continue the discussion by studying the effects of using it with the SEA, PA and HPEA.

For the SEA, from the results in Table 5.8 we can see that TAO has no effect on the MIF when the detection delay is only 5 ms. WTA reduces the MIF by 21.1% when detection delay is 5 ms; and reduces the MIF by 2.4% when detection delay is 25 ms. These results indicate that the collision reaction strategies are less effective with the SEA than they were with the EA.

Table 5.8 Collision reaction, detection delay comparison with compliant covering for the SEA.

Actuator	**Collision Reaction**	**Detection Delay (ms)**	**MIF (N) (including compliant Covering)**
SEA	None	5	123 (case 8.1)
		25	
		50	
	TAO	5	122 (case 8.2)
		25	123
		50	123
	WTA	5	97 (case 8.3)
		25	120
		50	123

To understand why the effectiveness decreased with the SEA, we will examine the motor torque, spring torque and impact force plots after 2s for the three cases listed in the table.

Comparing Figures 5.4.11 and 5.4.12, we can see that TAO has very little effect on the spring torque. This is because, during the collision, the link's momentum causes the spring to be squeezed harder after the motor has been turned off. However, from Figure 5.4.13 we can see that WTA is able to reduce the spring torque which causes the MIF to be reduced from 123 N to 97 N. The reduction is less than with the EA because the spring torque decreases slower than the motor torque as shown in the motor and spring force torques plot.

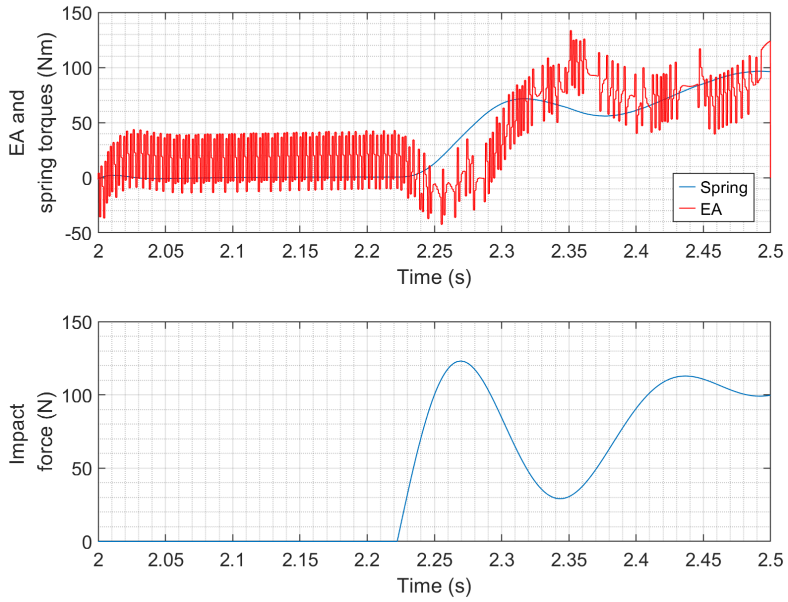

Figure 5.4.11 Motor plus HDT torque, spring torque and impact force after 2 s of SEA case 8.1.

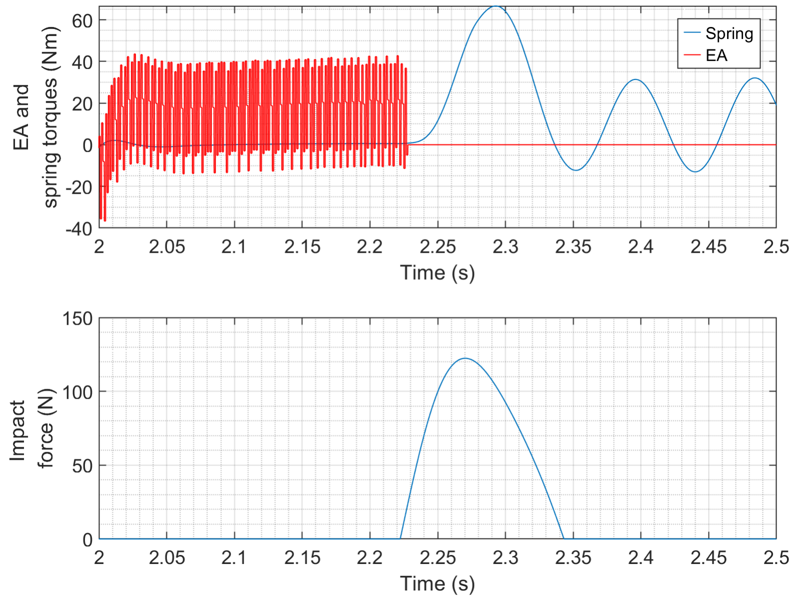

Figure 5.4.12 Motor plus HDT torque, spring torque and impact force after 2 s of SEA case 8.2.

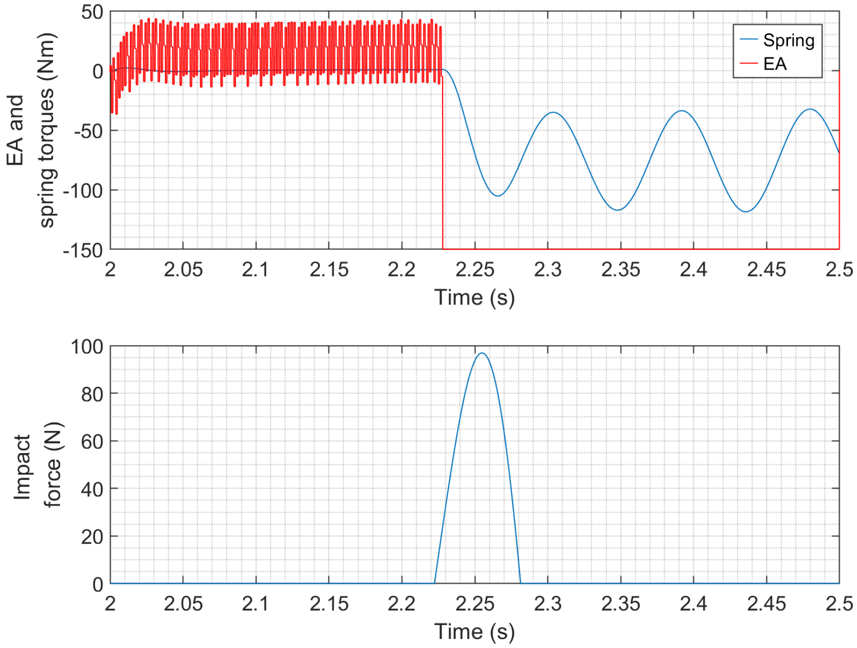

Figure 5.4.13 Motor plus HDT torque, spring torque and impact force after 2 s of SEA case 8.3.

The corresponding results for the PA are listed in Table 5.9. They show that TAO reduces the MIF by 1.6% and WTA reduces the MIF by 21.3% when the detection delay is 5 ms. When the detection delay is 25 ms, TAO changes the MIF by only 0.8%, and WTA reduces it by 4.1%. The plots of the pneumatic torque and impact force after 2 s for the three cases in the table are shown in Figures 5.4.14-5.4.16. The plots demonstrate similar behaviour to the SEA since the air in the PA compresses similar to a spring when the impact happens. The WTA strategy is again less effective than with the EA because the PA torque changes more slowly than the EA torque, as can be seen by comparing Figures 5.4.10 and 5.4.16.

Table 5.9 Collision reaction, detection delay comparison with compliant covering of PA.

Actuator	Collision Reaction	Detection Delay (ms)	Force (N) (including compliant covering)
Pneumatic	None	5	122 (PA case 9.1)
		25	
		50	
	TAO	5	120 (case 9.2)
		25	121
		50	122
	WTA	5	96 (case 9.3)
		25	117
		50	122

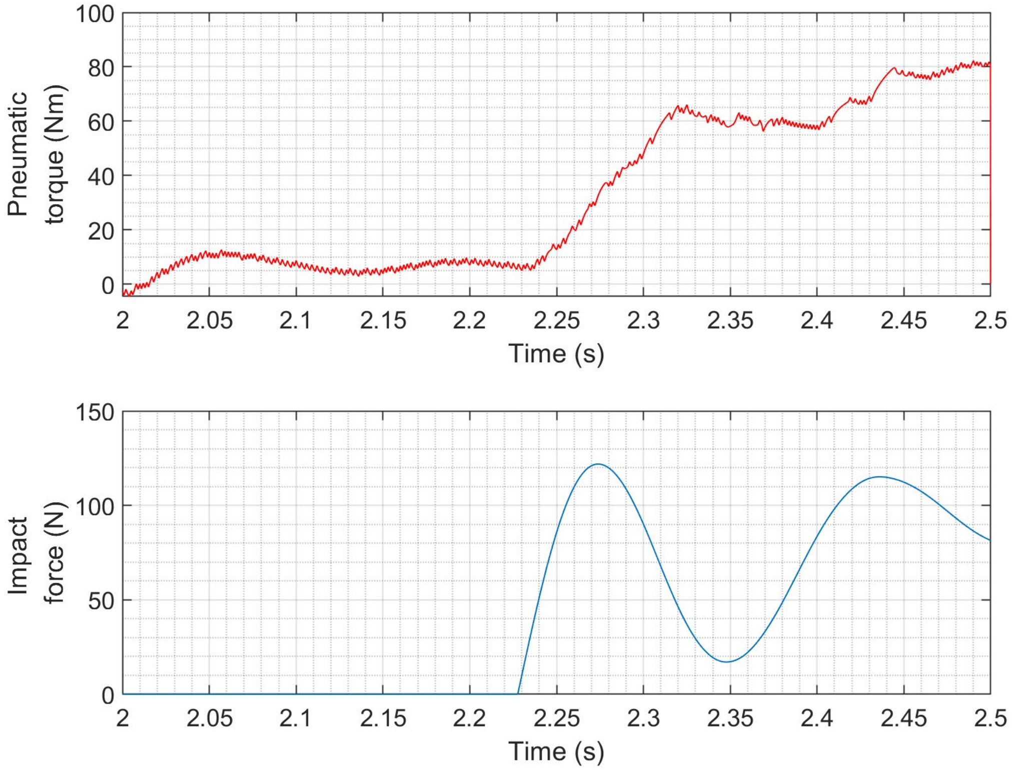

Figure 5.4.14 Pneumatic torque and impact force after 2 s of PA case 9.1.

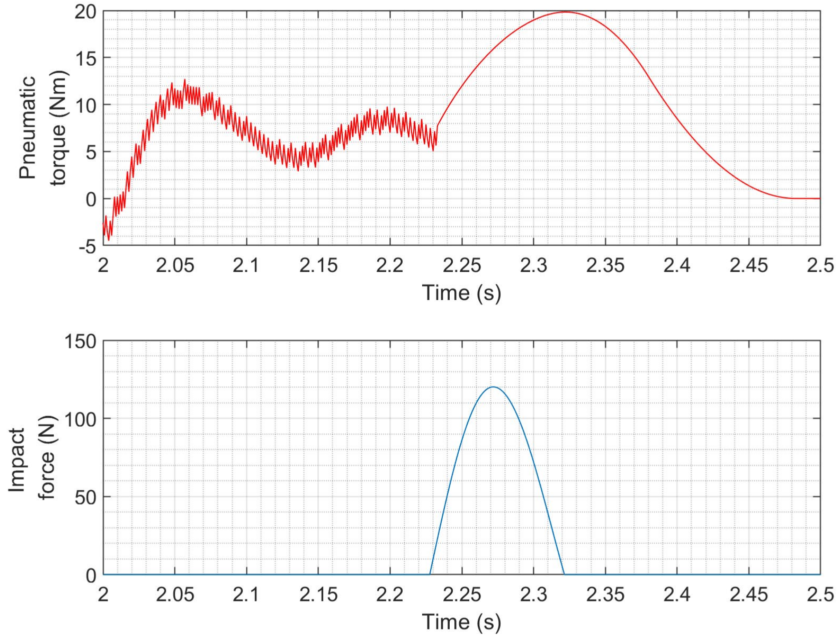

Figure 5.4.15 Pneumatic torque and impact force after 2 s of PA case 9.2.

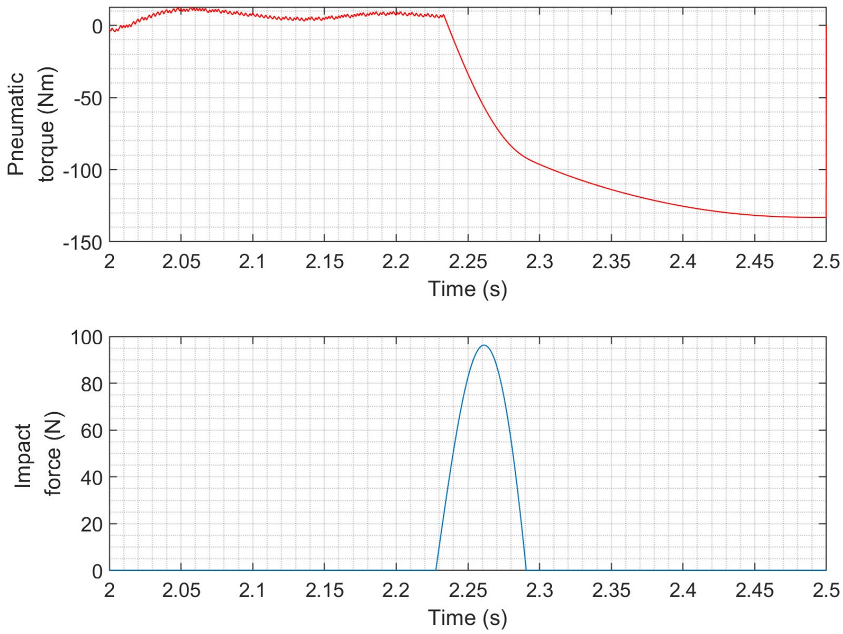

Figure 5.4.16 Pneumatic torque and impact force after 2 s of PA case 9.3.

Finally, the corresponding results for the HPEA are shown in Table 5.10. We can see that when the detection delay is 5 ms, TAO reduces the MIF by 12.4% and WTA reduces the MIF by 31.0%.

Table 5.10 Collision reaction, detection delay comparison with compliant covering for the HPEA.

Actuator	Collision Reaction	Detection Delay (ms)	Force (N) (including compliant covering)
HPEA	None	5	129 (HPEA case 10.1)
		25	
		50	
	TAO	5	113 (case 10.2)
		25	124
		50	129
	WTA	5	89 (case 10.3)
		25	119
		50	129

Plots of the pneumatic torque, electric torque, and impact force after 2 s for three cases identified in the table are shown in Figures 5.4.17 to 5.4.19. Comparing Figures 5.4.15 and 5.4.18, we can see that turning the PA off is not effective at reducing its torque. Comparing Figures 5.4.15 and 5.4.18, the benefit of the rapidly changing electric torque for reducing the MIF can be seen.

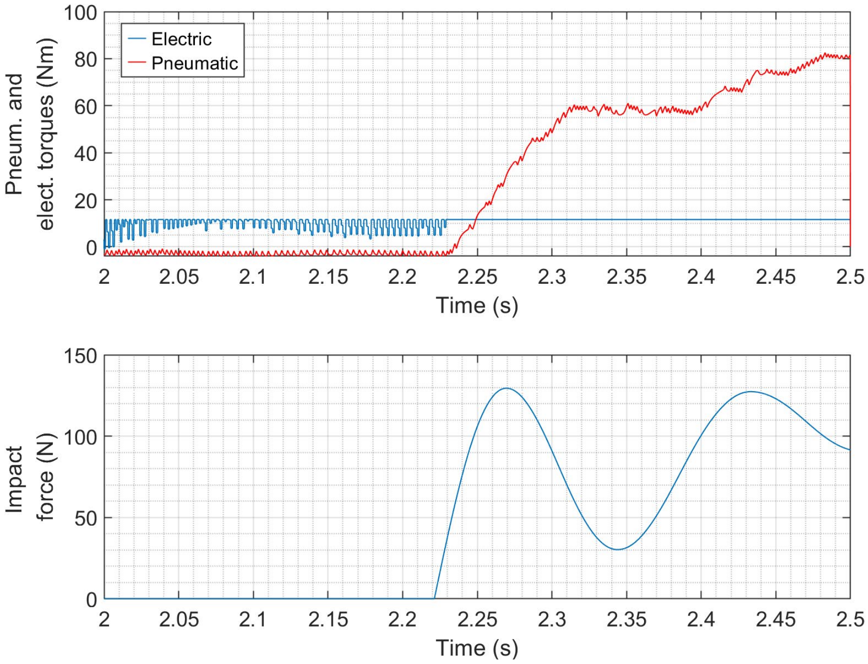

Figure 5.4.17 Pneumatic, electric torque and impact force after 2 s of HPEA case 10.1.

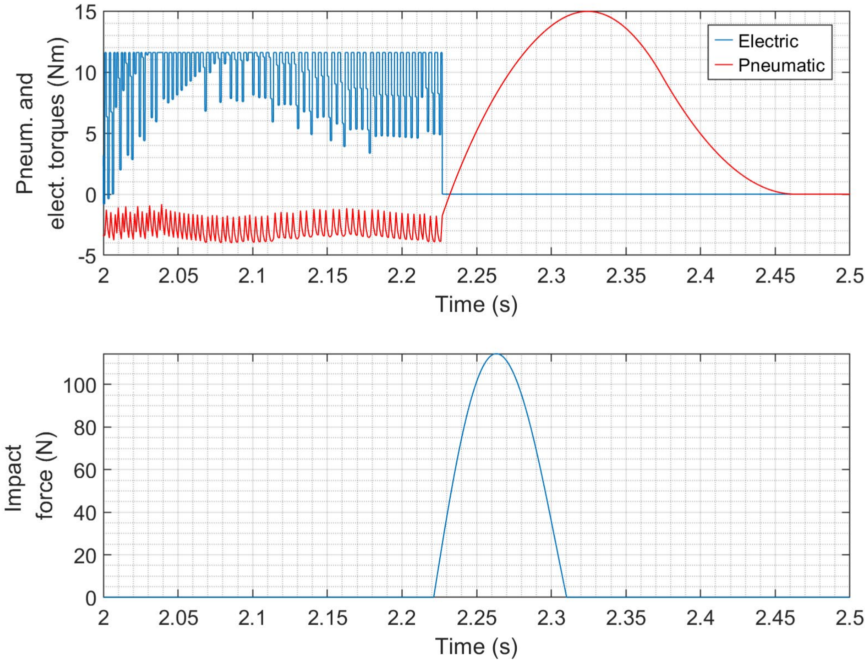

Figure 5.4.18 Pneumatic, electric torque and impact force after 2 s of HPEA case 10.2.

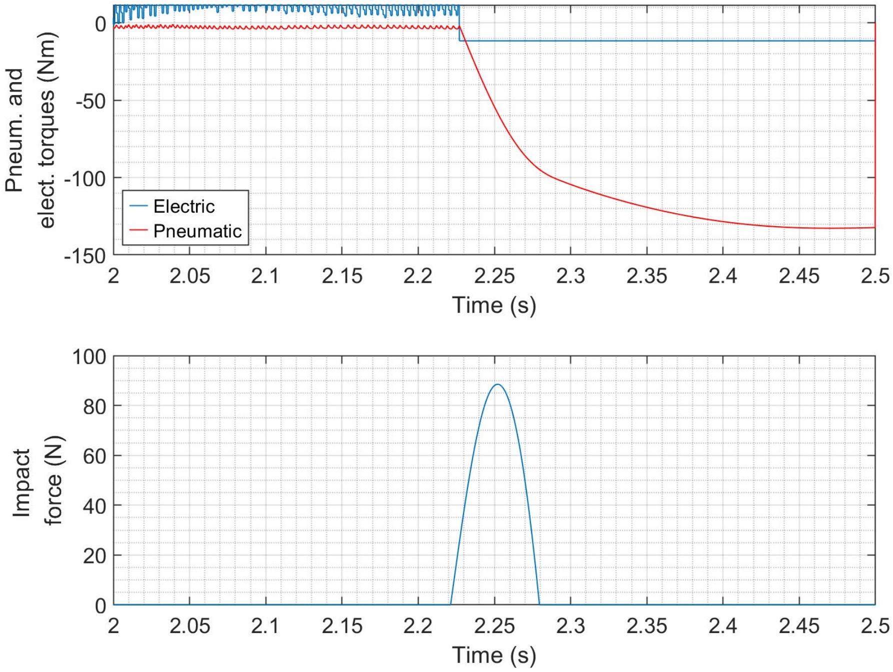

Figure 5.4.19 Pneumatic, electric torque and impact force after 2 s of HPEA case 10.3.

From all the results above, adding compliant covering and WTA when the collision is detected is the best approach for improving safety. For the SEA, PA and HPEA, the MIF when using this approach is under the 130 N limit when the detection delay is 50 ms or less. When the detection delay is 25 ms or less, the EA can be added to this list.

We have shown that adding a compliant covering with the default stiffness of $K_{foam} = 20$ kN/m is effective at improving safety, but we should not assume that other stiffness values will produce similar results. We will use the EA to study how the stiffness of the compliant covering affects the MIF. The cases with and without collision reaction strategies will be included.

For the case of no collision reaction, the MIF is plotted vs. covering stiffness in Figure 5.4.20. Since the covering was modelled as a spring, we might have expected this plot to have been a straight line. The nonlinear behavior of this plot will now be explained. A thick covering is impractical of course, so we chose a realistic thickness of 0.01 m. As discussed in section 3.4.1, a real covering will have a lower thickness limit where it cannot be further compressed so it becomes effectively rigid. When that thickness limit it reached, the covering doesn't compress, and the combined stiffness of the skull and covering increases as defined by (3.24). This is the reason the MIF increases for lower stiffness values. In Figure 5.4.20, a stiffness of about 27 kN/m produces the smallest MIF.

Figures 5.4.21 and 5.4.22 show how the peak impact force changes with the compliant cover stiffness when applying the TAO and WTA strategies, respectively. The collision detection delay is set to 25 ms. We can see that when using TAO, the best stiffness is about 21 kN/m. When WTA is applied, at the best stiffness of 11 kN/m and the MIF is only 82 N. These results show the advantage of the WTA strategy again.

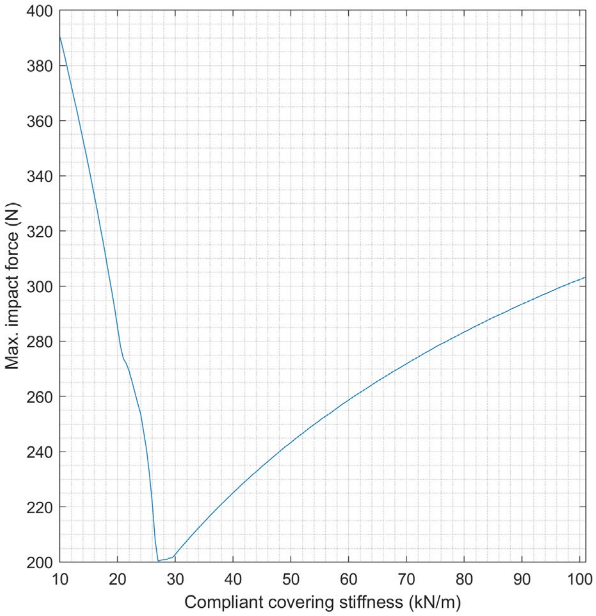

Figure 5.4.20 MIF vs. K_{foam}.

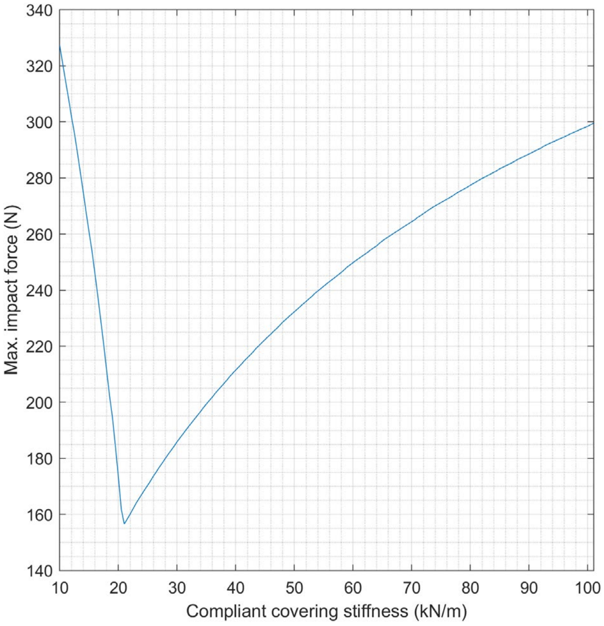

Figure 5.4.21 MIF vs K_{foam} when using the TAO reaction strategy.

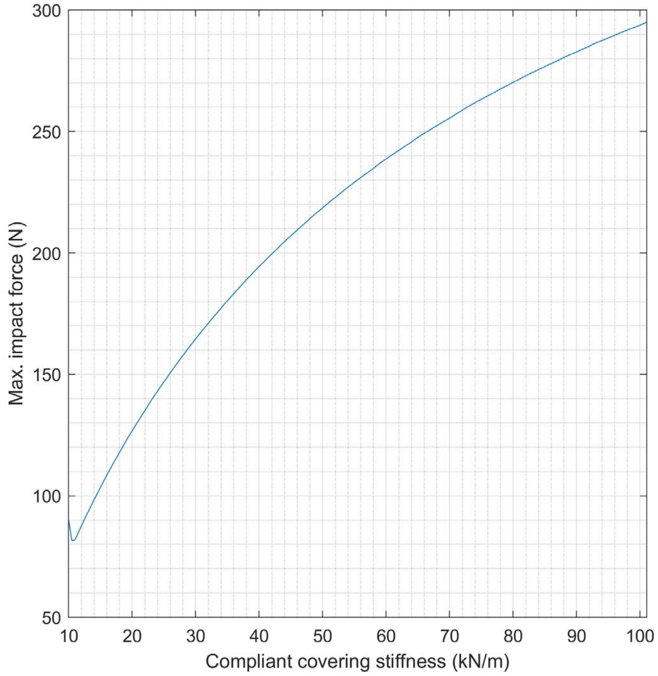

Figure 5.4.22 MIF vs K_{foam} when using the WTA reaction strategy.

5.4.3 Effects of the desired closed-loop bandwidth

In the previous section, we made f_{bw} the same for all actuators. The chosen value was 3 Hz. It is likely that each actuator will have its own "best" value for f_{bw}. In this section, we will vary f_{bw} for the four actuators to see how it affects the RMSE and MIF. Since there is no f_{bw} value that balances the need for both safety and performance, one value that prioritizes safety and a 2^{nd} value that prioritizes performance will be chosen for each actuator. We already know that adding a compliant covering and using WTA after detecting the collision will produce the smallest MIF, so in this section, both methods will be applied, and the detection time will be again set as 25 ms.

Firstly, let's see how the RMSE and MIF change with f_{bw} when using EA. As is shown in Figure 5.4.23, as f_{bw} is increased from 1 to 50 Hz, the MIF increases from 123 N to 144 N, while the RMSE reduces from 0.015 rad to only 0.000121 rad. Note that the erratic small increases and decreases in the MIF are caused by small variations in the robot's velocity at the moment of impact that are produced by the interaction of the sensor noise and the system's nonlinear dynamics. Based on these results, for the EA, f_{bw} values of 1 Hz and 50 Hz are the best safety and performance, respectively.

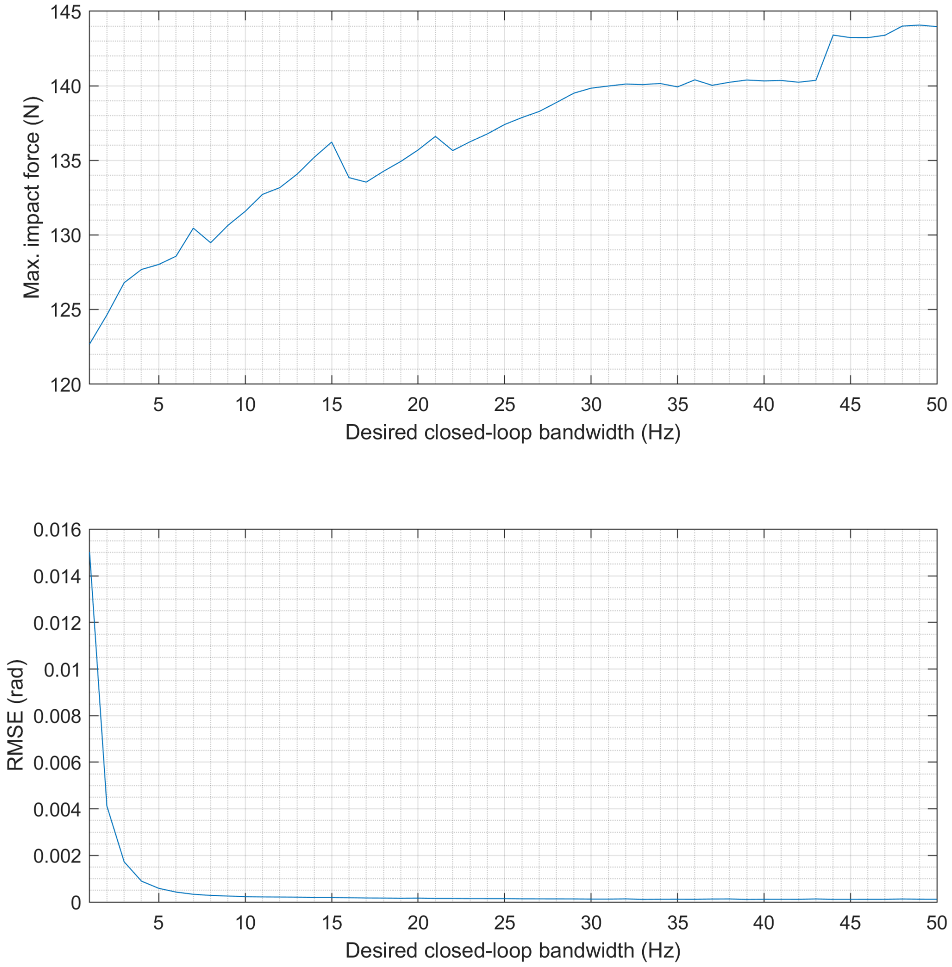

Figure 5.4.23 MIF and RMSE vs. f_{bw} for the EA.

The SEA was studied next. The SEA was found to be quite limited in terms of its achievable closed-loop bandwidth when compared with the EA. As shown in Figures 5.4.24 and 5.4.25, with $f_{bw} = 8$ Hz, the torque error is beginning to have significant oscillations, then when $f_{bw} = 9$ Hz, the amplitude of those vibrations grows over time, and closed-loop system is unstable. The cause of the instability is believed to be the large amount of motor saturation. Therefore, the variation of RMSE and MIF with the SEA will only be studied when f_{bw} varies from 1 to 8 Hz. These results are plotted in Figure 5.4.26.

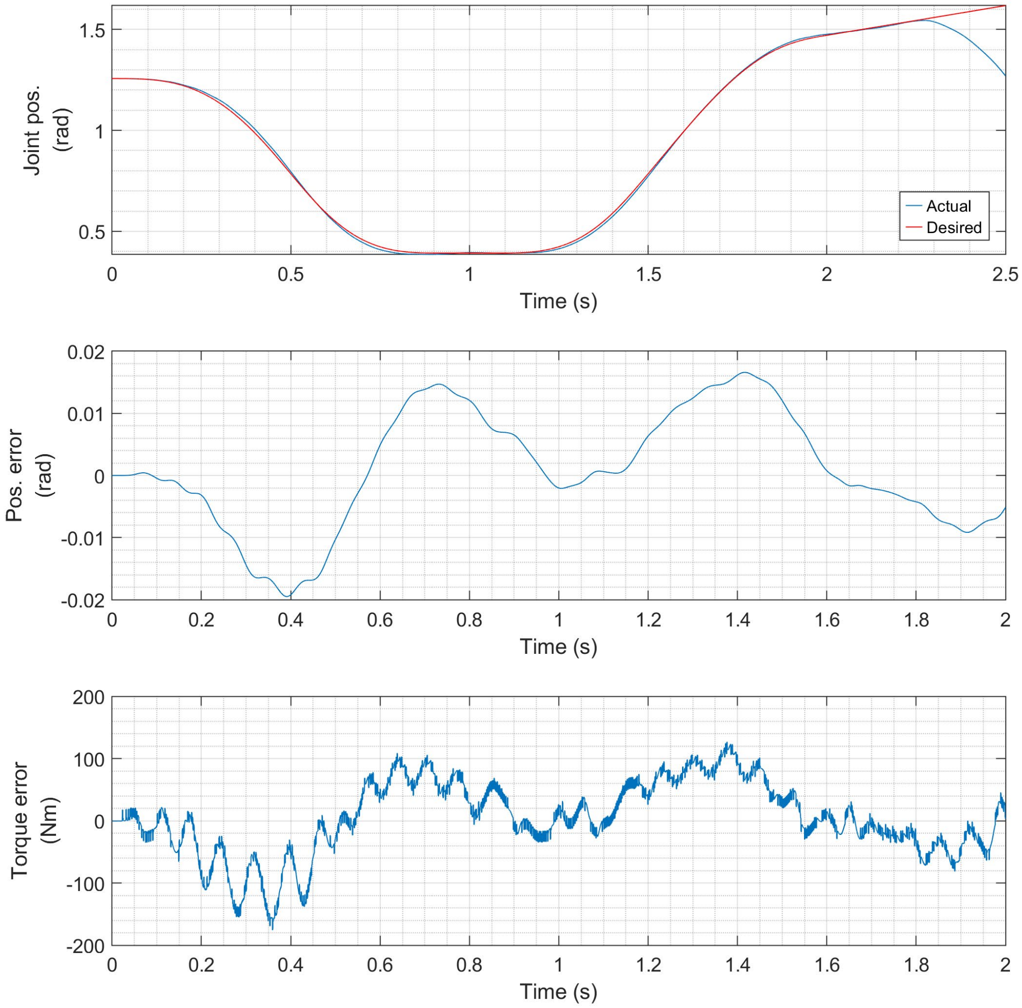

Figure 5.4.24 Results for the SEA when $f_{bw} = 8$ Hz.

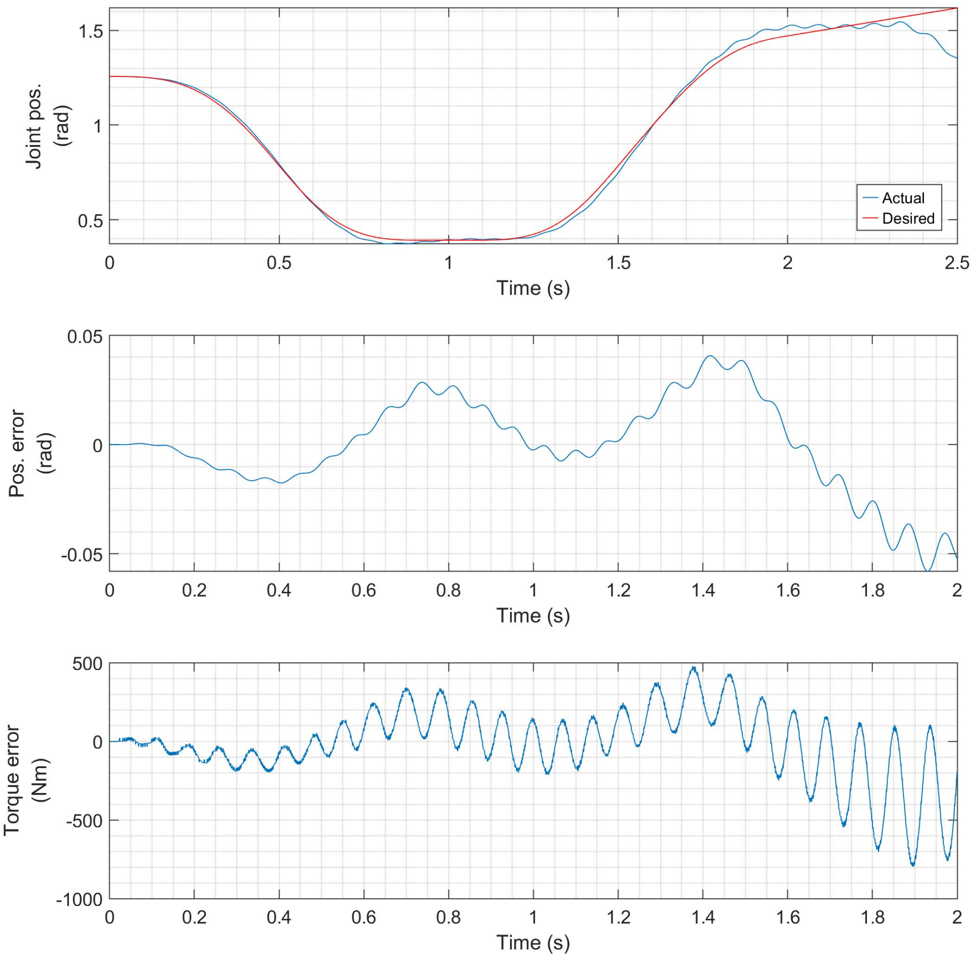

Figure 5.4.25 Results for the SEA when $f_{bw} = 9$ Hz .

As is shown in Figure 5.4.26, except for a small bump around 1 Hz, the MIF stays lower than 130 N when $f_{bw} \leq 5$ Hz . Please note that when $f_{bw} = 1$ Hz , the MIF is 0 because the collision didn't happen due to the actuator's large tracking error. When $f_{bw} > 5$ Hz , the MIF sometimes exceeds 130 N, and the RMSE also increases a small amount. The lowest MIF of 104 N occurs at f_{bw} = 1.9 Hz, and the lowest RMSE of 0.00194 rad is produced when $f_{bw} = 3.3$ Hz.

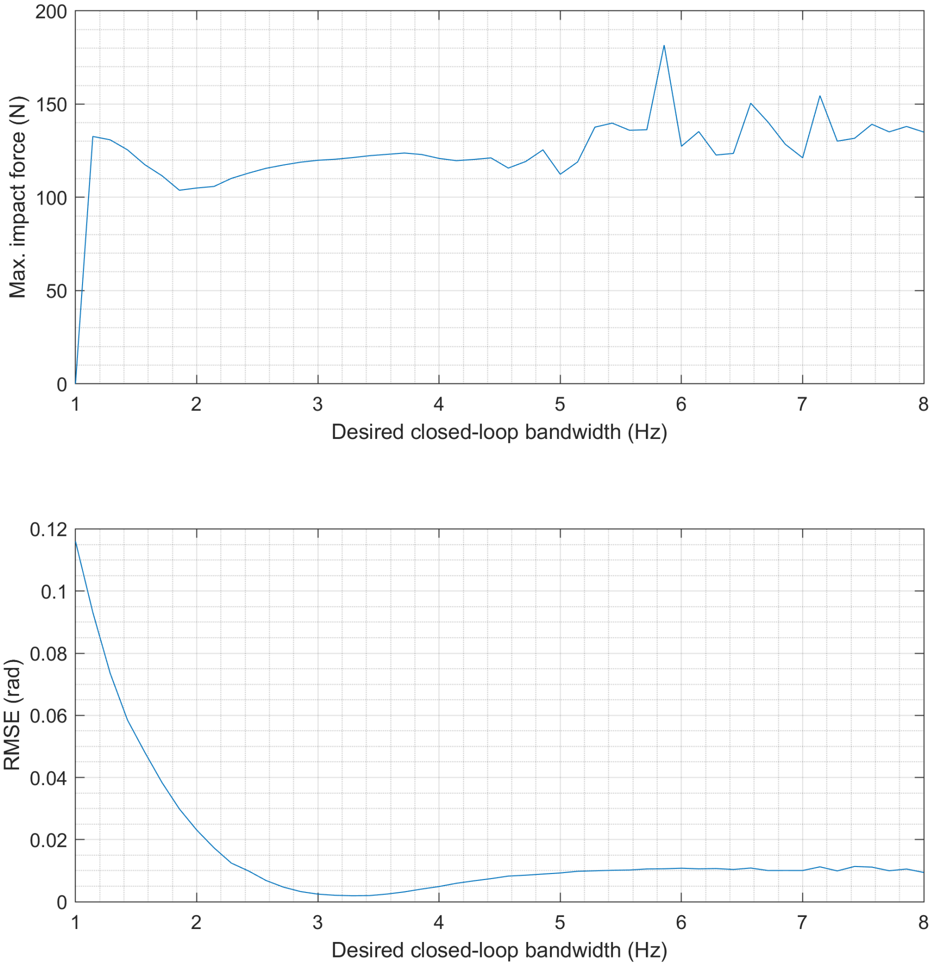

Figure 5.4.26 MIF and RMSE vs f_{bw} for the SEA.

The PA was studied next. The PA was also found to have a low limit for its achievable closed-loop bandwidth when compared with the EA. As shown in Figures 5.4.27 and 5.4.28, we can see from the position error and pressure error plots that the closed-loop becomes unstable when $f_{bw} = 16\text{ Hz}$, likely due to the amount of saturation of the valve inputs.

Therefore, we will only discuss how the RMSE and MIF varies with f_{bw} over the range 1 to 15 Hz.

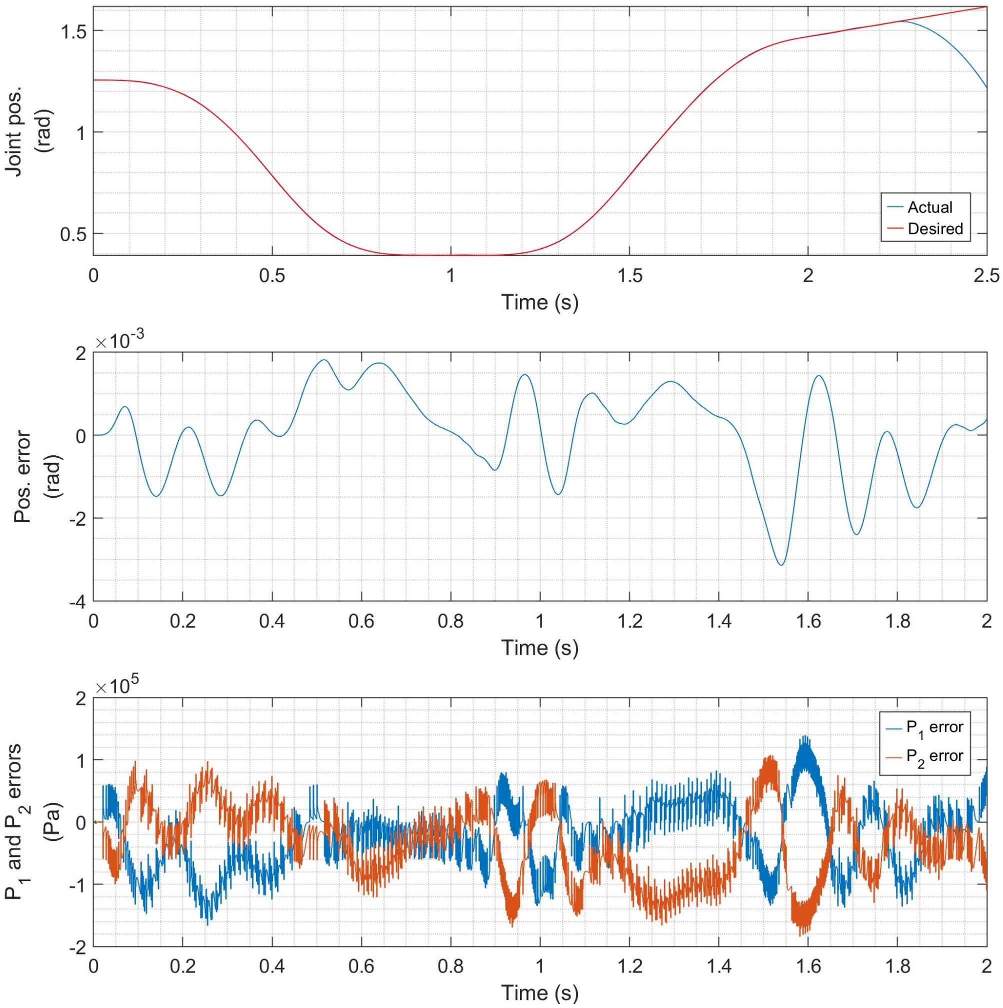

Figure 5.4.27 Results for the PA when $f_{bw} = 15$ Hz.

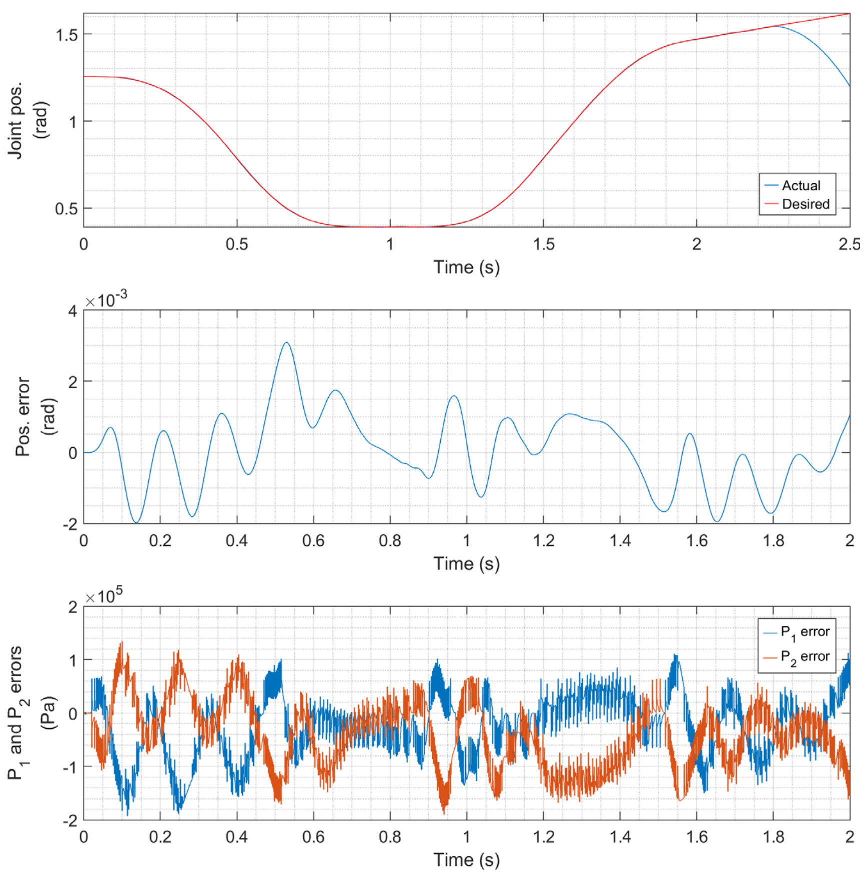

Figure 5.4.28 Results for the PA when $f_{bw} = 16$ Hz.

As shown in Figure 5.4.29, the MIF stays under 130 N when $f_{bw} \leq 13.5$ Hz. The best choice for safety is 8.1 Hz where the MIF is only 102 N. The RMSE reduces as f_{bw} is increased, so the best choice for performance is 15.0 Hz where the RMSE is 0.00107 rad.

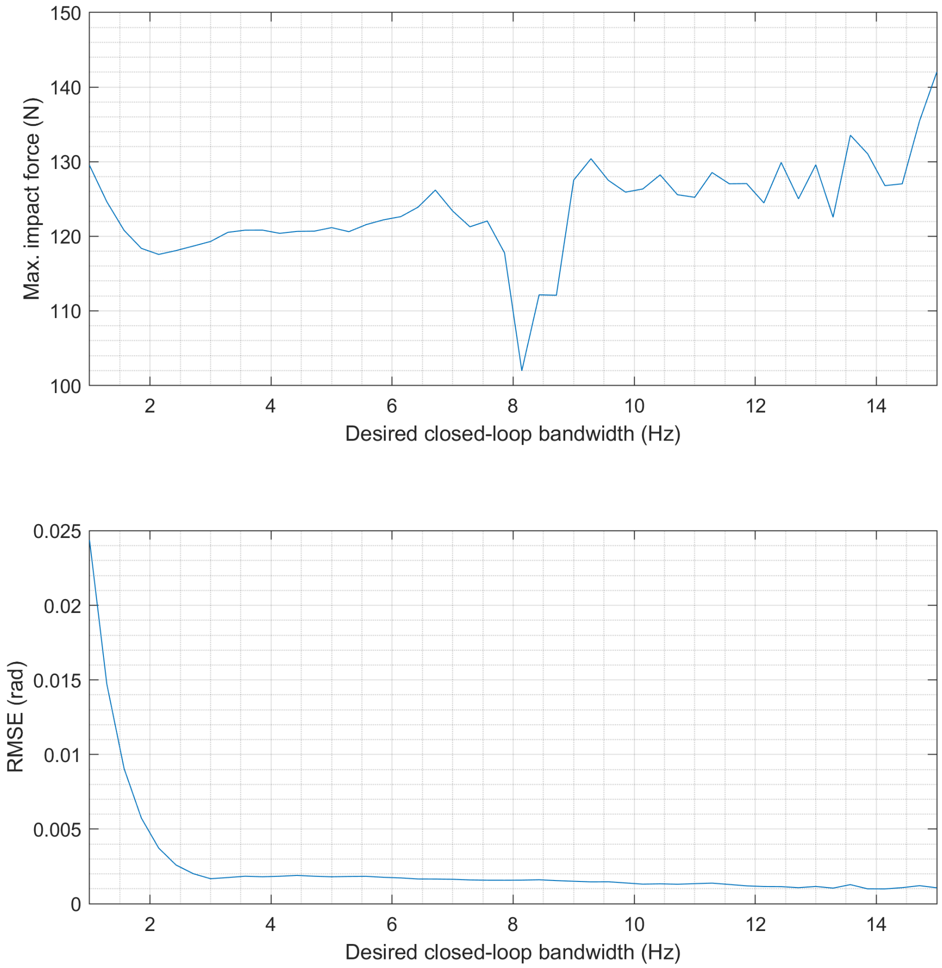

Figure 5.4.29 MIF and RMSE vs. f_{bw} for the PA.

The HPEA was studied last. As shown in Figures 5.4.30 and 5.4.31, similar to the PA, the closed-loop becomes unstable when f_{bw} is around 20 Hz, again likely due to the amount of saturation of the valve inputs. Therefore, we will only discuss how the RMSE and MIF changes with f_{bw} over the range 1 to 19.5 Hz.

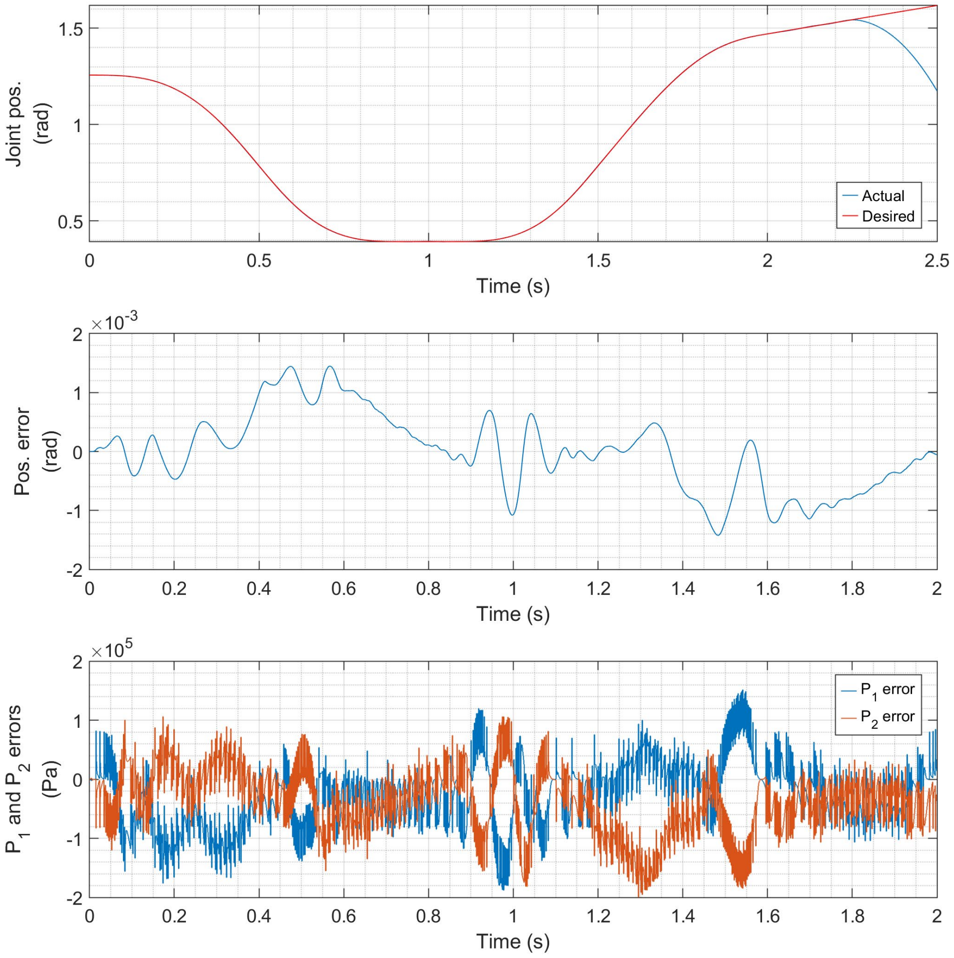

Figure 5.4.30 Results for the HPEA when $f_{bw} = 19$ Hz .

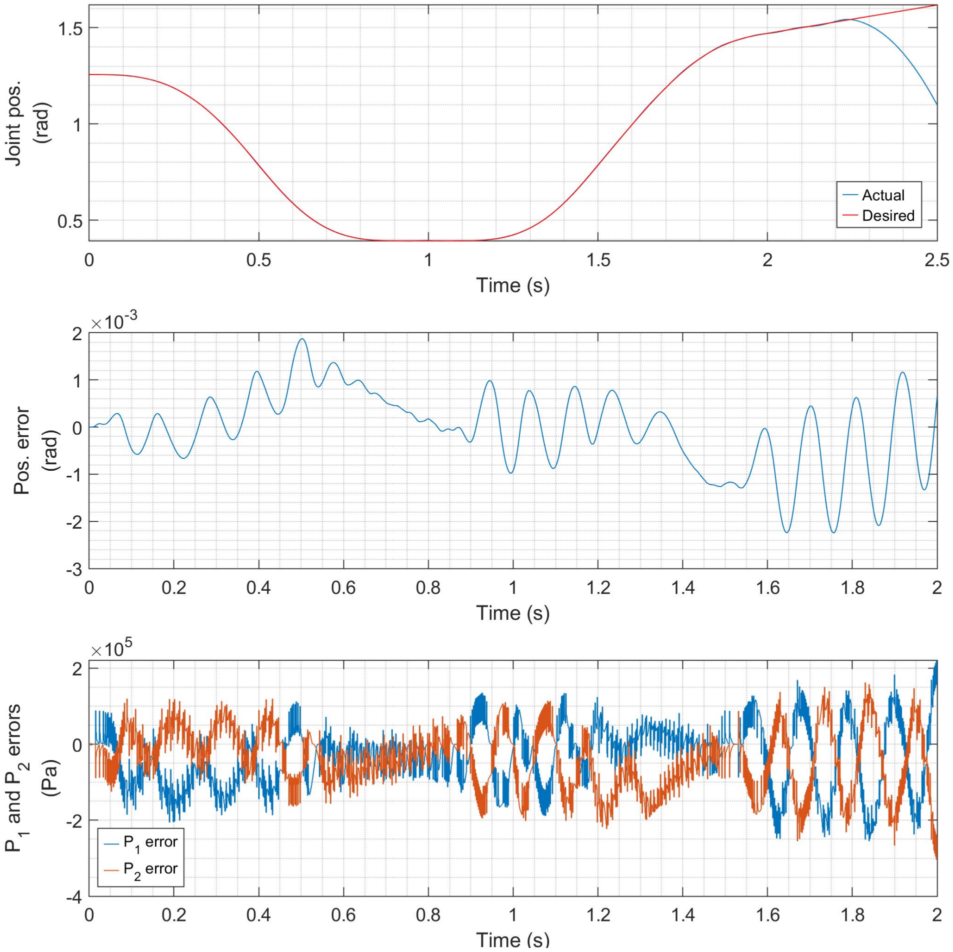

Figure 5.4.31 Results for the HPEA when $f_{bw} = 20$ Hz.

As shown in Figure 5.4.32, the MIF stays below, or near to, 130 N until 19.5 Hz where it suddenly jumps to almost 350 N. The RMSE reduces as f_{bw} is increased. The best choice for safety is 8.0 Hz where the MIF is 117 N, and the best choice for performance is 19.2 Hz where the RMSE is 0.000663 rad.

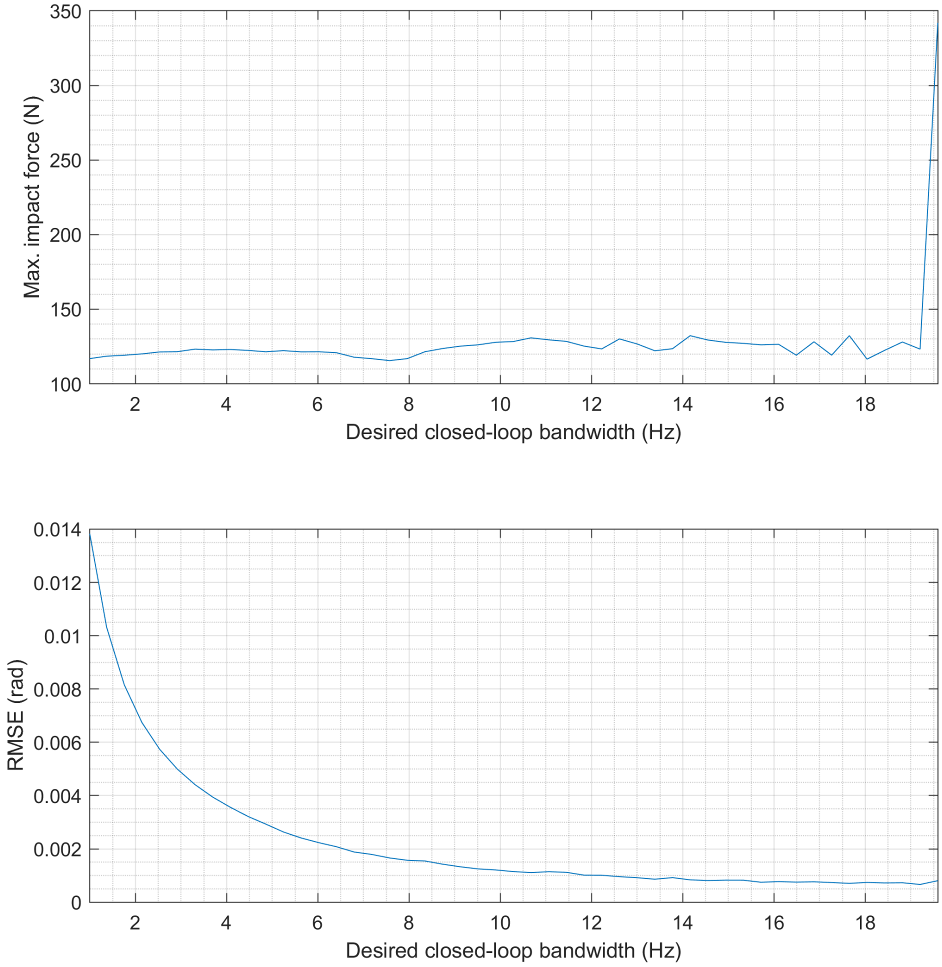

Figure 5.4.32 MIF and RMSE vs. f_{bw} for the HPEA.

For all of the actuators, the RMSE and MIF values for the best choices of f_{bw} are summarized in Table 5.11. If performance is the only concern, then the EA should be used since its RMSE is the smallest. The HPEA provides the 2nd best performance, followed by the PA and SEA. In terms of safety, the PA produces the lowest MIF, but the value for the SEA is very similar. The HPEA provides the 3rd best safety, and the EA is the least safe.

Table 5.11 Best results comparison for all actuators.

Actuator	**Priority**	f_{bw} **(Hz)**	**RMSE (rad)**	**MIF (N)**
EA	Safety	1.0	0.0150	123
	Performance	50.0	0.000121	144
SEA	Safety	1.9	0.0299	104
	Performance	3.3	0.00194	121
PA	Safety	8.1	0.00158	102
	Performance	15.0	0.00107	142
HPEA	Safety	8.0	0.00157	117
	Performance	19.2	0.000663	123

5.4.4 Effects of the SEA spring stiffness

The results in the previous sections have shown that the SEA with a spring stiffness of $K_{s1} = 20$ kN/rad had the effect of reducing the MIF and increasing the RMSE in comparison with the EA. In this section, we will examine how the MIF and RMSE vary as this string stiffness is changed. Compliant covering and WTA will both be applied.

Figure 5.4.33 shows how the MIF and RMSE change with the spring stiffness. The

MIF and RMSE both decreases initially and then increase with the increasing of the spring stiffness. The MIF stays below the 130 N safety limit until $K_{s1} >$ 90 kN/m and is smallest when K_{s1} is about 70 kN/rad. When the RMSE is also considered, the best range for K_{s1} is 16-20 kN/rad.

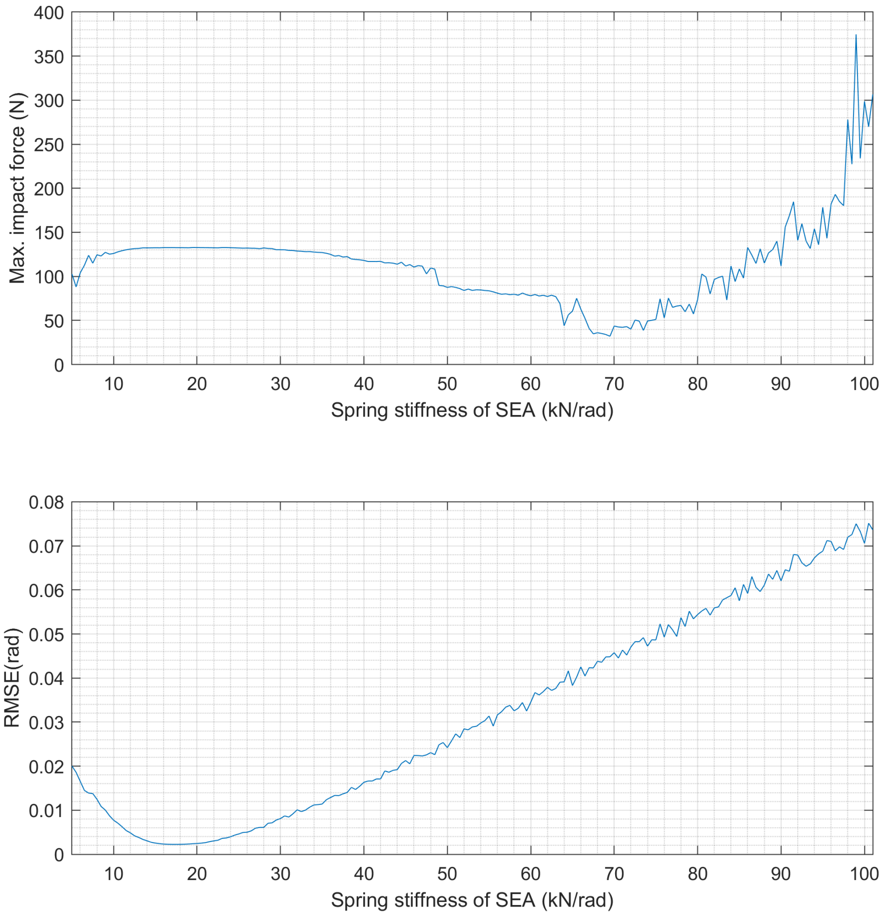

Figure 5.4.33 Maximum impact force and RMSE vs. SEA spring stiffness.

5.5 Summary

In this chapter, a robot whose first joint was driven by each of the four actuators (*i.e.,* EA, SEA, PA and HPEA) was simulated for a challenging motion trajectory. After showing that they are more dangerous than unconstrained impacts, constrained impacts between the robot and human head were studied. Sensor noise and model mismatch were included to make the simulation more realistic. The performance and safety of the robot were quantified using RMSE and MIF, respectively. The effects of the collision reaction strategies (*i.e.,* TAO and WTA), detection delay, compliant covering stiffness, desired closed-loop bandwidth, and SEA spring stiffness were studied.

When no safety measures were used, the MIF values for all actuators exceeded ISO's 130 N safety limit. Adding compliant covering was found to be the most effective method to reduce the MIF. For example, a compliant covering with the default stiffness of 20 kN/m reduced the MIF for the SEA from 346 N to 123 N. The MIF for all actuators except the EA were reduced to below the 130 N limit using this only a compliant covering. At the same time, the stiffness of the covering should be chosen carefully. As shown in section 5.4.2, choosing very small or very large values for its stiffness can make the safety benefit of a compliant covering negligible.

The comparison of the TAO and WTA reaction strategies when compliant covering was not used concluded that neither was very effective at improving the safety of the SEA, PA and HPEA. Even with the fast dynamics of the EA, the WTA strategy only reduced the MIF by 20.6% when the detection delay was 5 ms. With delays of 25 ms and 50 ms, no improvement was produced. The WTA strategy worked much better when combined with a compliant covering. With a 25 ms detection delay, this combination reduced the MIF values for the EA, SEA, PA and HPEA by 73%, 65%, 65%, and 66%, respectively.

The value chosen for f_{bw} was also shown to be important. Larger values tended to increase the MIF and decrease the RMSE, but there were also exceptions to these trends. The distinct f_{bw} values that produced the best safety and performance were found for each actuator. As discussed at the end of section 5.4.3, using the compliant covering, WTA strategy, and these individually chosen f_{bw} values, the EA ranked highest in terms of performance and lowest in terms of safety. The PA was the safest, but ranked 3rd in terms of performance. The SEA was slightly less safe and ranked last in terms of performance. The HPEA achieved the best combination of performance and safety.

CHAPTER 6 OPTIMIZATION-BASED PATH PLANNER FOR REDUCING THE IMPACT FORCE

6.1 Introduction

As discussed in section 2.5, state-of-the-art path planners can reduce a robot's reflected mass during its motion, and decrease the impact force of a collision, but they can only be used with redundant robots. A redundant spatial robot has more than six DOF and a redundant planar robot has more than three DOF. Non-redundant robots are much more common, and are less expensive, than redundant robots. They include 6-DOF industrial robots and 6-DOF assistive robots. In this chapter, an optimal path planner is proposed that can be used with non-redundant robots. Although the included equations and results are for a 3-DOF planar robot, the proposed planner can be easily extended for use with a 6-DOF spatial robot.

The equations for the robot's dynamics and its reflected mass are given in section 6.2. This section also includes results and a discussion of how the reflected mass varies with the joint angles and contact normal. In section 6.3, the optimal planner, and a simple planner (used as a benchmark), are presented. Simulation results for the two path planners are presented and discussed in section 6.4. The chapter is summarized in section 6.5.

6.2 Dynamics and Reflected Mass of a 3R Planar Robotic Arm

6.2.1 Dynamics

A planar 3-DOF robotic arm with three revolute joints, and moving in the horizontal plane, will be used to evaluate the two path planners. It is also known as a 3R planar robot. The robot's model is shown in Figure 6.2.1.

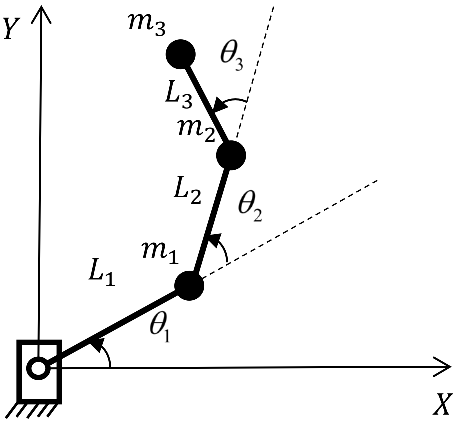

Figure 6.2.1 Model of the 3R planar robot.

The dynamic equation of the robot driven by EAs is given by:

$$\begin{bmatrix} R_{g1}\tau_{M1} - \tau_{CT1} - R_{g1}\tau_{F1} \\ R_{g2}\tau_{M2} - \tau_{CT2} - R_{g2}\tau_{F2} \\ R_{g3}\tau_{M3} - \tau_{CT3} - R_{g3}\tau_{F3} \end{bmatrix} = \mathbf{M} \begin{bmatrix} \ddot{\theta}_1 \\ \ddot{\theta}_2 \\ \ddot{\theta}_3 \end{bmatrix} + \mathbf{h} \tag{6.1}$$

where $\tau_{Mi}, \tau_{CTi}, \tau_{Fi}$, and R_{gi} $(i = 1, 2, \text{ and } 3)$ are the motor torques, contact torques, friction torques and transmission ratios for the three joints, respectively; the inertia matrix is:

$$\mathbf{M} = \begin{bmatrix} m_{11} & m_{12} & m_{13} \\ m_{21} & m_{22} & m_{23} \\ m_{31} & m_{32} & m_{33} \end{bmatrix} \tag{6.2}$$

and the vector of Coriolis and centripetal torques is:

$$\mathbf{h} = \begin{bmatrix} h_1 \\ h_2 \\ h_3 \end{bmatrix} \tag{6.3}$$

where:

$$\begin{aligned} m_{11} &= J_1 {R_{g1}}^2 + m_1 {L_1}^2 + m_2 {L_1}^2 + m_3 {L_1}^2 + m_2 {L_2}^2 + m_3 {L_2}^2 + m_3 {L_3}^2 \\ &\quad +2m_3 L_1 L_3 \cos(\theta_2 + \theta_3) + 2m_2 L_1 L_2 \cos\theta_2 + 2m_3 L_1 L_2 \cos\theta_2 + 2m_3 L_2 L_3 \cos\theta_3 , \\ m_{12} &= m_2 {L_2}^2 + m_3 {L_2}^2 + m_3 {L_3}^2 + L_1 L_3 m_3 \cos(\theta_2 + \theta_3) \\ &\quad +m_2 L_1 L_2 \cos\theta_2 + m_3 L_1 L_2 \cos\theta_2 + 2m_3 L_2 L_3 \cos\theta_3 , \\ m_{13} &= m_3 {L_3}^2 + m_3 L_1 L_3 \cos(\theta_2 + \theta_3) + m_3 L_2 L_3 \cos\theta_3 , \\ m_{21} &= m_{12} , \\ m_{22} &= J_2 {R_{g2}}^2 + m_2 {L_2}^2 + m_3 {L_2}^2 + m_3 {L_3}^2 + 2m_3 L_2 L_3 \cos\theta_3 , \\ m_{23} &= m_3 {L_3}^2 + m_3 L_2 L_3 \cos\theta_3 \\ m_{31} &= m_{13} \\ m_{32} &= m_{23} \\ m_{33} &= J_3 {R_{g3}}^2 + m_3 {L_3}^2 \end{aligned} \tag{6.4}$$

$$\begin{aligned}
h_1 = & -m_2 L_1 L_2 \dot{\theta}_2^{\,2} \sin\theta_2 - m_3 L_1 L_2 \dot{\theta}_2^{\,2} \sin\theta_2 - m_3 L_2 L_3 \dot{\theta}_3^{\,2} \sin\theta_3 - m_3 L_1 L_3 \dot{\theta}_2^{\,2} \sin\left(\theta_2 + \theta_3\right) \\
& -m_3 L_1 L_3 \dot{\theta}_3^{\,2} \sin\left(\theta_2 + \theta_3\right) - 2m_2 L_1 L_2 \dot{\theta}_1 \dot{\theta}_2 \sin\theta_2 - 2m_3 L_1 L_2 \dot{\theta}_1 \dot{\theta}_2 \sin\theta_2 - 2m_3 L_2 L_3 \dot{\theta}_1 \dot{\theta}_3 \sin\theta_3 \\
& -2m_3 L_2 L_3 \dot{\theta}_2 \dot{\theta}_3 \sin\theta_3 - 2m_3 L_1 L_3 \dot{\theta}_1 \dot{\theta}_2 \sin\left(\theta_2 + \theta_3\right) - 2m_3 L_1 L_3 \dot{\theta}_1 \dot{\theta}_3 \sin\left(\theta_2 + \theta_3\right) \\
& -2m_3 L_1 L_3 \dot{\theta}_2 \dot{\theta}_3 \sin\left(\theta_2 + \theta_3\right) \\[1em]
h_2 = & \left(m_2 + m_3\right) L_1 L_2 \dot{\theta}_1^{\,2} \sin\theta_2 - m_3 L_2 L_3 \dot{\theta}_3^{\,2} \sin\theta_3 + m_3 L_1 L_3 \dot{\theta}_1^{\,2} \sin\left(\theta_2 + \theta_3\right) \\
& -2m_3 L_2 L_3 \dot{\theta}_1 \dot{\theta}_3 \sin\theta_3 - 2m_3 L_2 L_3 \dot{\theta}_2 \dot{\theta}_3 \sin\theta_3 \\[1em]
h_3 = & \, m_3 L_3 \left[L_1 \dot{\theta}_1^{\,2} \sin\left(\theta_2 + \theta_3\right) + L_2 \dot{\theta}_1^{\,2} \sin\theta_3 + L_2 \dot{\theta}_2^{\,2} \sin\theta_3 + 2L_2 \dot{\theta}_1 \dot{\theta}_2 \sin\theta_3 \right]
\end{aligned} \tag{6.5}$$

Note that the friction torques in (6.1) can be calculated in a similar manner to (3.4).

In (6.4), $J_1, J_2, \text{and}\, J_3$ are the motor inertias. They are given by:

$$\begin{gathered}
J_1 = \frac{\left(m_1 + m_2 + m_3\right) L_1^{\,2} + \left(m_2 + m_3\right) L_2^{\,2} + m_3 L_3^{\,2}}{r_i R_{g1}^{\,2}} \\[1em]
J_2 = \frac{\left(m_2 + m_3\right) L_2^{\,2} + m_3 L_3^{\,2}}{r_i R_{g2}^{\,2}} \quad \text{and} \\[1em]
J_3 = \frac{m_3 L_3^{\,2}}{r_i R_{g3}^{\,2}}
\end{gathered} \tag{6.6}$$

where r_i is the inertia ratio. Since inertia matching is a common design approach with robots, $r_i = 1$ will be used for all of the robot's joints.

Another difference with the 1-DOF version is the calculation of the contact torques, $\tau_{CTi}\ (i = 1, 2, \text{and } 3)$. Since it is the most dangerous, only the constrained impact case is simulated in this chapter. Beginning with the head deflection:

$$D_h = \begin{bmatrix} n_{cx} & n_{cy} \end{bmatrix} \begin{bmatrix} x_{robot} - x_{head} \\ y_{robot} - y_{head} \end{bmatrix} \tag{6.7}$$

where $\begin{bmatrix} n_{cx} & n_{cy} \end{bmatrix}$ is the contact normal, the contact force components in the x and y directions are then:

$$\begin{bmatrix} F_{cx} \\ F_{cy} \end{bmatrix} = \begin{cases} K_{head} \begin{bmatrix} n_{cx} \\ n_{cy} \end{bmatrix} D_h & D_h > 0 \\ \begin{bmatrix} 0 \\ 0 \end{bmatrix} & D_h \le 0 \end{cases} \tag{6.8}$$

Note that no compliant covering with be used with this robot. The torque from the contact is then given by:

$$\begin{bmatrix} \tau_{CT1} \\ \tau_{CT2} \\ \tau_{CT3} \end{bmatrix} = \mathbf{J}_{xy}^{\ T} \begin{bmatrix} F_{cx} \\ F_{cy} \end{bmatrix} \tag{6.9}$$

where $\mathbf{J}_{xy}$ is the first and second row of $\mathbf{J}_r$, and $\mathbf{J}_r$ is the robot's Jacobian matrix which is:

$$\mathbf{J}_r = \begin{bmatrix} -L_1 \sin\theta_1 - L_2 \sin(\theta_1 + \theta_2) - L_3 \sin(\theta_1 + \theta_2 + \theta_3) & -L_2 \sin(\theta_1 + \theta_2) - L_3 \sin(\theta_1 + \theta_2 + \theta_3) & -L_3 \sin(\theta_1 + \theta_2 + \theta_3) \\ L_1 \cos\theta_1 + L_2 \cos(\theta_1 + \theta_2) + L_3 \cos(\theta_1 + \theta_2 + \theta_3) & L_2 \cos(\theta_1 + \theta_2) + L_3 \cos(\theta_1 + \theta_2 + \theta_3) & L_3 \cos(\theta_1 + \theta_2 + \theta_3) \\ 1 & 1 & 1 \end{bmatrix} \tag{6.10}$$

The friction torques with the 3-DOF robot are given by:

$$\tau_{Fj} = \begin{cases} \tau_{Cj} & \dot{\theta}_j = 0 \text{ and } \tau_{Mj} - h_j / R_{gj} > \tau_{Cj} \\ -\tau_{Cj} & \dot{\theta}_j = 0 \text{ and } \tau_{Mj} - h_j / R_{gj} < -\tau_{Cj} \\ \tau_{Mj} - h_j / R_{gj} & \dot{\theta}_1 = 0 \text{ and } \left| \tau_{Mj} - h_j / R_{gj} \right| \leq \tau_{Cj} \\ \tau_{Cj} \operatorname{sgn}\left(\dot{\theta}_j\right) + C_{vj}\dot{\theta}_j & \dot{\theta}_j \neq 0 \end{cases} \quad j = 1,2,3 \tag{6.11}$$

where τ_{Cj} is the Coulomb friction torque, C_{vj} is the coefficient of viscous friction.

The controller for the 3-DOF robot is also different. The control law is given by:

$$\tau_{Mjf} = \frac{1}{R_{gj}} \hat{\mathbf{M}} \left(\ddot{\theta}_{jd} + \hat{\mathbf{h}} \right) \quad j = 1,2,3 \tag{6.12}$$

$$\tau_{Mjb} = \frac{1}{R_{gj}} \hat{\mathbf{M}} \left[K_{pj} \left(\theta_{jd} - \hat{\theta}_j \right) + K_{dj} \left(\dot{\theta}_{jd} - \dot{\hat{\theta}}_j \right) + K_{ij} \int \left(\theta_{jd} - \hat{\theta}_j \right) \right] \quad j = 1,2,3 \tag{6.13}$$

$$\tau_{Mj} = \tau_{Mjf} + \tau_{Mjf} + \hat{\tau}_{Fj} \quad j = 1,2,3 \tag{6.14}$$

where τ_{Mjf} and τ_{Mjb} are the feedforward and feedback term of the motor torque; and K_{pj}, K_{dj} and K_{ij} are the proportional, derivative and integral terms of the PID controller. θ_{jd} is the desired joint angle we get from the desired trajectory. $\hat{\theta}_j$ is the estimated joint angle. $\hat{\tau}_{Fj}$ is the estimated value of τ_{Fj}, its equation is similar to equation (6.11) except we need to replace τ_{Cj} with its estimated value $\hat{\tau}_{Cj}$.

6.2.2 Reflected mass

As noted in chapter 2, (Khatib, 1995) introduced the concept of a reflected mass, which is the mass perceived during a collision with the robot's EE, and derived its general equation. The reflected mass of the 3R planar robot, $m_{contact}$, is obtained from the robot's Cartesian space inertia matrix and the contact normal vector as follows:

$$m_{contact} = \begin{bmatrix} n_{cx} & n_{cy} \end{bmatrix} \mathbf{M_{cs}} \begin{bmatrix} n_{cx} \\ n_{cy} \end{bmatrix} \tag{6.15}$$

where $\mathbf{M_{cs}}$ is the robot's Cartesian space inertia matrix which is given by:

$$\mathbf{M_{cs}} = \left(\mathbf{J}_{xy} \mathbf{M}^{-1} \mathbf{J}_{xy}^{T} \right)^{-1} \tag{6.16}$$

Please note that the expanded equation for $m_{contact}$ has 268 terms so it will not be presented here for brevity.

Equations (6.15) and (6.16) were programmed in Matlab to allow the influences of the contact normal direction and the three joint angles on the reflected mass to be studied. The parameters used for the robot were as follows: $L_1 = L_2 = 0.4$ m, $L_3 = 0.15$ m, $m_1 = m_2 = 3$ kg, $m_3 = 2$ kg, and $R_{g1} = R_{g2} = R_{g3} = 100$. We chose six different combinations of θ_3 and the contact normal, and plotted the corresponding $m_{contact}$ surfaces to show how $m_{contact}$ varies with θ_1 and θ_2. **Please note $m_{contact}$ values larger than 100 kg are not shown on these plots.**

Figures 6.2.2 to 6.2.4 show the $m_{contact}$ surfaces when the contact normal equals $\left[0,1\right]$ and $\theta_3 = 0, -\frac{\pi}{4}$, and $-\frac{\pi}{2}$, respectively. Figure 6.2.2 shows that in this case, the largest $m_{contact}$ values exceed 100 kg, and we can easily observe that the reflected mass becomes bigger when θ_1 gets close to $\frac{\pi}{2}$ and θ_2 gets close to 0.

We will now explain discuss why this happens. Note that this robot has a singularity when $\theta_2 = 0$. Since the contact normal is $[0,1]$, the EE velocity will be in that direction. At the extreme point, when $\theta_1 = \frac{\pi}{2}$, $\theta_2 = \theta_3 = 0$, the robot would require infinite joint velocity to move in that direction, and therefore would possess infinity kinetic energy, so the reflected mass will also be infinite. Near this point the reflected mass is also very large.

Further understanding can be obtained from Figures 6.2.3 and 6.2.4. In the blue regions of these figures, we can observe that $\theta_1 + \theta_2 + \theta_3$ is close to $\frac{\pi}{2}$, which means the direction of the 3rd link is nearly perpendicular to the contact normal. In this situation, only very small joint velocities are required to move the EE in the contact normal's direction, so the reflected mass is also small. On the other hand, when $\theta_1 + \theta_2 + \theta_3$ is close to 0, the reflected mass becomes large, and Figure 6.2.3 shows that it even becomes even larger when θ_2 is close to 0, which means how the close the arm is to a singularity can also increase the reflected mass. This conclusion is also consistent with the phenomenon in Figure 6.2.2.

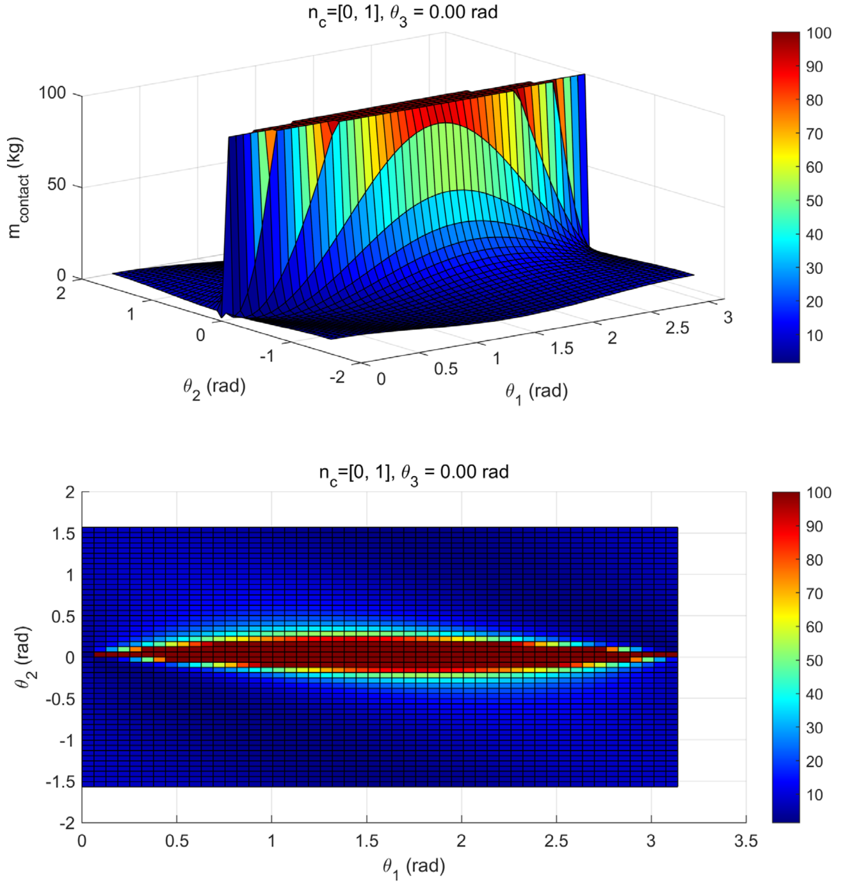

Figure 6.2.2 $m_{contact}$ surface for the case $\mathbf{n_c} = [0,1]$ and $\theta_3 = 0$.

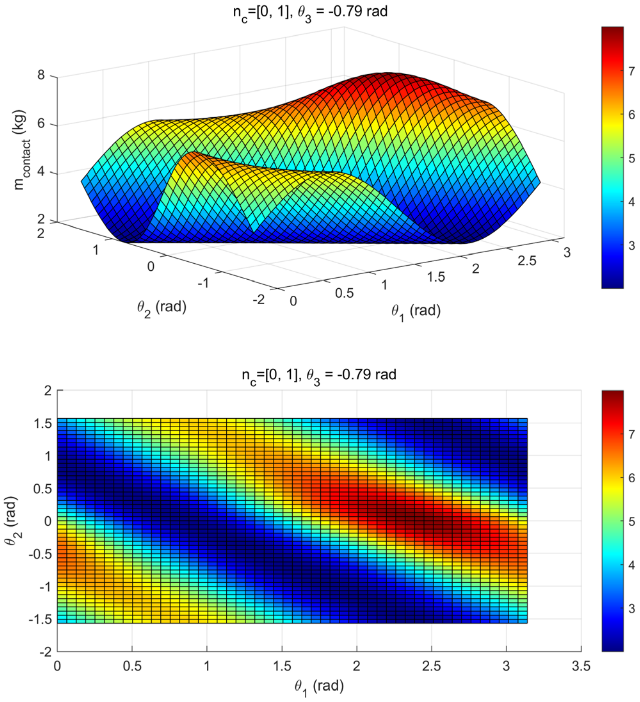

Figure 6.2.3 $m_{contact}$ surface for the case $\mathbf{n_c} = [0,1]$ and $\theta_3 = -\frac{\pi}{4}$.

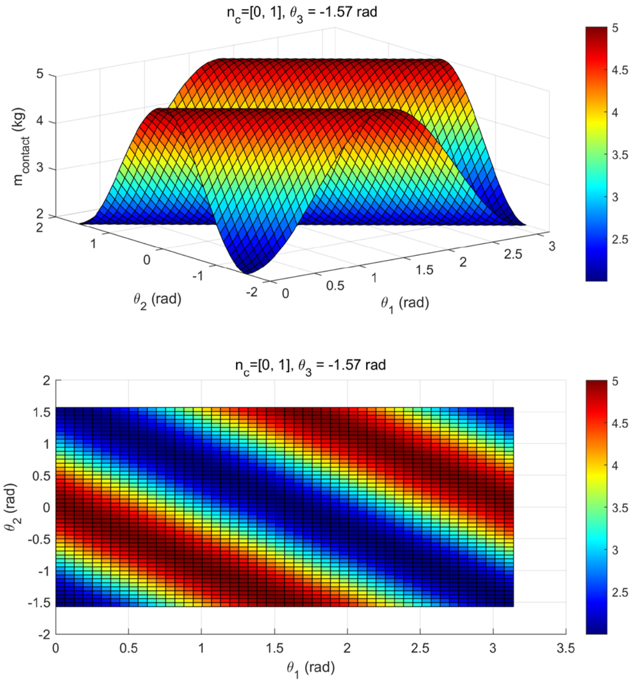

Figure 6.2.4 $m_{contact}$ surface for the case $\mathbf{n_c} = [0,1]$ and $\theta_3 = -\dfrac{\pi}{2}$.

Figures 6.2.5 to 6.2.7 shows the $m_{contact}$ surfaces when the contact normal is $[1,0]$ and $\theta_3 = 0, -\dfrac{\pi}{4}$, and $-\dfrac{\pi}{2}$, respectively. By comparing the plots of Figures 6.2.5 to 6.2.7 and Figures 6.2.2 to 6.2.4, we observe that $m_{contact}$ is closely related to the directions of the contact normal and the vector decided by $\theta_1 + \theta_2 + \theta_3$ (which is the same as the direction of the 3rd link). When these two directions are colinear, $m_{contact}$ becomes large, and when they are perpendicular, $m_{contact}$ becomes small. In addition, to limit the size of $m_{contact}$ the singularity should be avoided as much as possible.

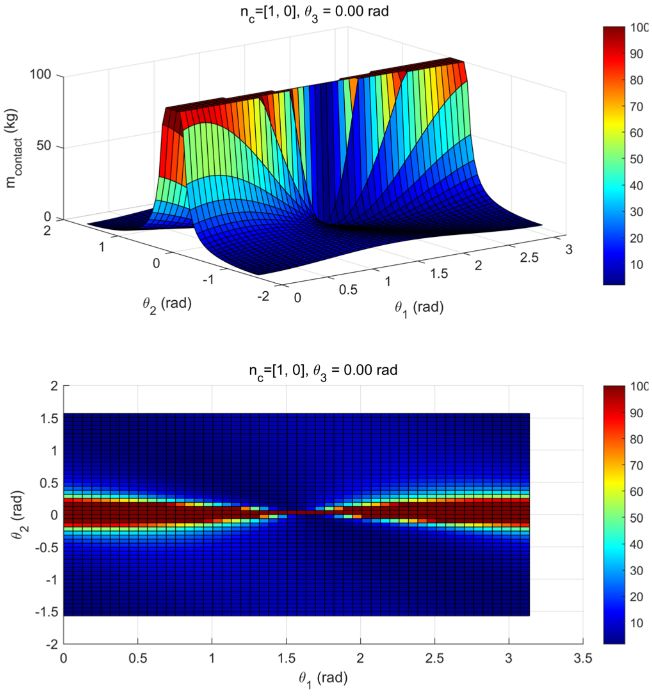

Figure 6.2.5 $m_{contact}$ surface for the case $\mathbf{n_c} = [1,0]$ and $\theta_3 = 0$.

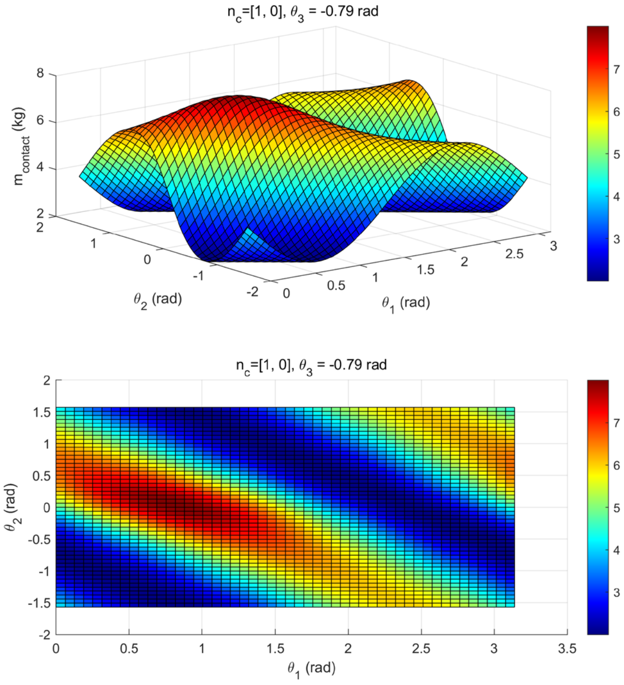

Figure 6.2.6 $m_{contact}$ surface for the case $\mathbf{n_c} = [1, 0]$ and $\theta_3 = -\frac{\pi}{4}$.

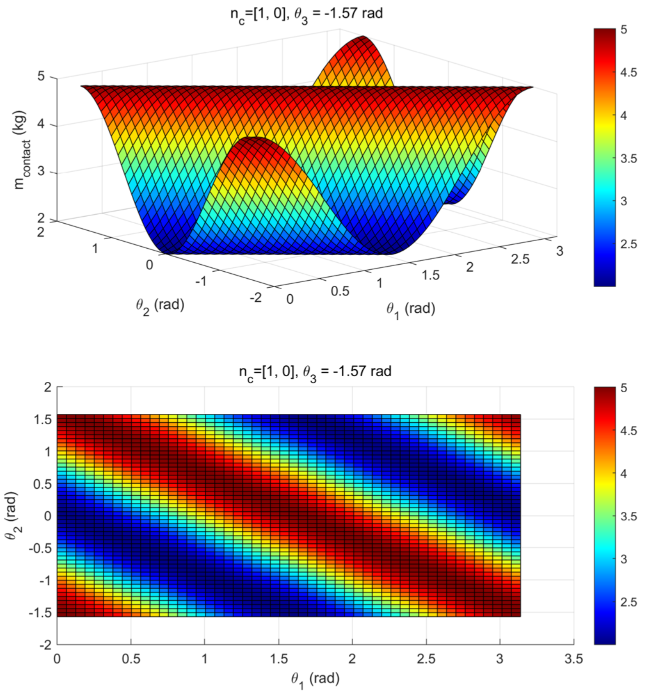

Figure 6.2.7 $m_{contact}$ surface for the case $\mathbf{n_c} = [1, 0]$ and $\theta_3 = -\frac{\pi}{2}$.

6.3 Path Planners

We present the two path planners in this section. Both planners calculate the desired change in the joint angles during the planner's sampling period. The reflected mass is only considered in the second path planner. We will term the first planner the "simple planner". It is based on the inverse kinematic algorithm given in section 3.7.1 of (Siciliano et al., 2008). Its equation is:

$$\begin{bmatrix} \Delta\theta_{d1} \\ \Delta\theta_{d2} \\ \Delta\theta_{d3} \end{bmatrix} = T_p \mathbf{J}_r^{-1} \left(\begin{bmatrix} v_{xd} \\ v_{yd} \\ 0 \end{bmatrix} + k_p \left(\begin{bmatrix} x_d \\ y_d \\ \varphi_d \end{bmatrix} - \begin{bmatrix} x \\ y \\ \varphi \end{bmatrix} \right) \right) \tag{6.17}$$

where $\Delta\theta_{di}(i=1,2,3)$ is the desired change in the joint angles during the planner's sampling period; T_p is the planner's sampling period; v_{xd} and v_{yd} is the desired EE velocity; x_d and y_d are the components of the desired EE position; φ_d is the desired EE orientation angle; and k_p is a positive constant.

The proposed optimal planner is the second path planner. It makes a trade-off between decreasing $m_{contact}$ and keeping the position of the end effector close to (or exactly on) the desired path. To give it a greater ability to decrease $m_{contact}$ it does not try to keep the EE orientation close to its desired value. It minimizes the following objective function:

$$objective = obj_1 + obj_2 + obj_3 \tag{6.18}$$

$$obj_1 = \begin{bmatrix} \dfrac{\partial m_{contact}}{\partial \theta_1} & \dfrac{\partial m_{contact}}{\partial \theta_2} & \dfrac{\partial m_{contact}}{\partial \theta_3} \end{bmatrix} \begin{bmatrix} \Delta\theta_{d1} \\ \Delta\theta_{d2} \\ \Delta\theta_{d3} \end{bmatrix} \tag{6.19}$$

$$obj_2 = Q\left(\left|x_d - x_{robot}\right| + \left|y_d - y_{robot}\right|\right) \tag{6.20}$$

$$obj_3 = R_{acc}\left(\left|\Delta\theta_{d1} - \Delta\theta_{d1previous}\right| + \left|\Delta\theta_{d2} - \Delta\theta_{d2previous}\right| + \left|\Delta\theta_{d3} - \Delta\theta_{d3previous}\right|\right) \tag{6.21}$$

where $\Delta\theta_{diprevious}(i=1,2,3)$ is the $\Delta\theta_{di}$ value from the planner's previous sampling time, Q is the weight for the path following errors, R_{acc} is the weight on the desired angular accelerations of the joints. The planner minimizes the objective defined by (6.18)-(6.21), subject to constraints of the desired joint angles, desired joint velocities, desired joint accelerations, and desired EE velocity. The purposes of the terms obj_1, obj_2, and obj_3 are to reduce the reflected mass, reduce the path tracking error, and reduce the commanded acceleration during the motion.

Considering the motion of a robotic arm for tasks such as material handling, the closer the EE gets to the target location, the more important the path following errors are. With the optimal planner, this is implemented by increasing the value of Q as the EE approaches its target.

It is important to note that the sampling period of the planner, T_p, is 0.01 s, which is 10 times larger than the sampling period of 0.001s used by the robot's motor controllers. The motor controllers are the same as in section 4.2.2 except that an integral term was added with the 3R robot. Making T_p longer allowed the planning to be computed faster. The planner uses cubic spline interpolation to get the desired joint angles, desired angular velocity, and desired angular accelerations to use at each sampling time of the motor controllers.

6.4 Simulation of path planner

6.4.1 Simulation overview

The simulation was programmed in Matlab using m code. We chose two different paths to make the results more comprehensive. With "Path 1" the EE starting point and target point in the XY plane are (0, 0.35) m and (0.5, 0.35) m, respectively. With path 2, the corresponding points are (-0.2, 0.15) m and (0.3, 0.15) m. The desired EE orientation angle used with both paths was: $\varphi_d = 0$. The head's position was set to 0.02 m in front of the target location. Friction and sensor noise are included in all simulations.

The parameters of the robot are the same in section 6.2.2. The parameters of the EA for the first two joints are the same as in Table 5.3. For joint 3, since it is the wrist joint of the robot, and wrist joints typically use much smaller motors than shoulder and elbow joints, we set the motor torque limit for joint 3 as: $\tau_{\max 3} = 0.28$ Nm. Assuming the friction scales down linearly with the maximum torque, we obtained: $\tau_{C3} = 0.031$ Nm and $C_{v3} = 7.37 \times 10^{-4}$ Ns. The desired closed-loop bandwidth was set as 10 Hz, the proportional and derivative gains were calculated using (4.9) and the integral gains were all set to 1000. The parameters of the path planner were set as follows: $k_p = R_{acc} = 50$, $Q = 0.05t$, where t is the simulation time.

6.4.2 Path planner comparison

The simulations were executed on a laptop running the Windows 10 operating system. Its central processing unit (CPU) is a 2.60GHz, Intel i7-10750H. The execution times (averaged over five runs) for the simple and optimal planners were 0.025 s and 1.663 s, respectively.

Table 6.1 shows the MIF values from the constrained impact when using the two planners and two paths. We can see that for both paths the optimal planner reduces the MIF by around 75% compared to its value with the simple planner.

Table 6.1 MIF values for the two planners and two paths.

Planner and path	**MIF (N)**
Simple planner (Path 1)	570
Optimal planner (Path 1)	146
Simple planner (Path 2)	640
Optimal planner (Path 2)	164

Those results show the large safety improvement produced by the optimal planner, but don't show how it affects the EE's path. The plots of the EE position and orientation for the two planners following path 1 without a human present (meaning no collision happens) are shown for the simple and optimal controllers in Figures 6.4.1 and 6.4.2, respectively. Figure 6.4.1 shows that maximum position error occurs near the start of the motion and is less than 5 mm, the maximum orientation error is 0.04 rad, and that the EE reaches the target position and orientation perfectly with the simple planner. Because the optimal planner is trying to reduce $m_{contact}$ and follow the path at the same time, it creates the new desired path shown by the red line in Figure 6.4.2. Note that the optimized desired path and original desired path converge close to the target location due to the time varying Q value used with the optimal planner. The plots of the actual position show that it reaches the target position just like the simple planner. Note that optimal planner does not try to keep the EE orientation close to its original desired value in the lower plot, as discussed in section 6.3.

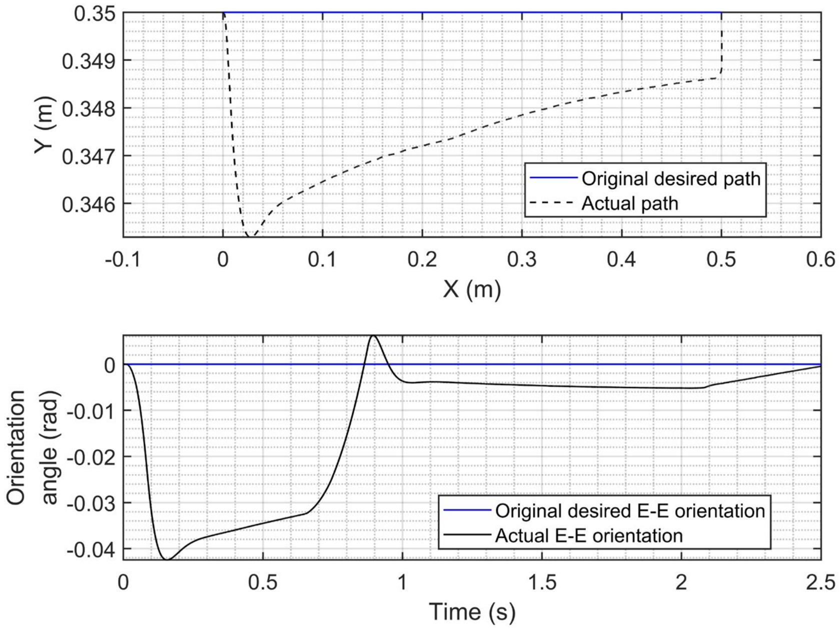

Figure 6.4.1 EE position and orientation for the simple planner, path 1, and no human.

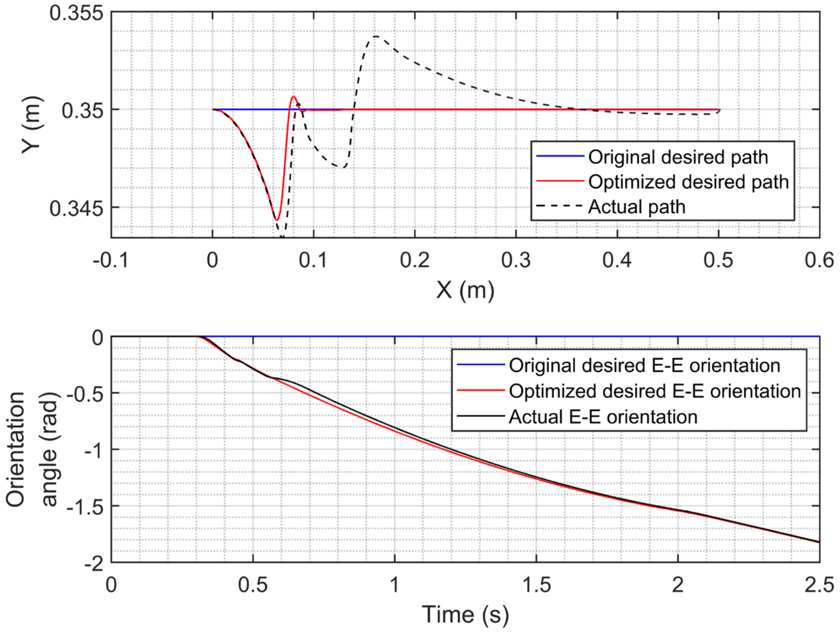

Figure 6.4.2 EE position and orientation for the optimal planner, path 1, and no human.

Now the results when the collision happens will be presented and discussed. Figure 6.4.3 shows the EE's path and orientation for the simple planner, and path 1. From the lower plot we can see that the collision happens at the time around 2s. Figure 6.4.4 shows the robot's configuration at the start and end of the path, and Figure 6.4.5 shows the reflected mass of the arm during the motion and contact force. From Figure 6.4.4 we can observe that the 3rd link's direction was nearly colinear with the contact normal when the collision happened, and recalling our conclusions from section 6.2.2, we would expect that the reflected mass would be large. Figure 6.4.5 shows our expectations were correct. The reflected mass was about 28 kg when the collision happened, and during the motion it was larger than 20 kg most of the time.

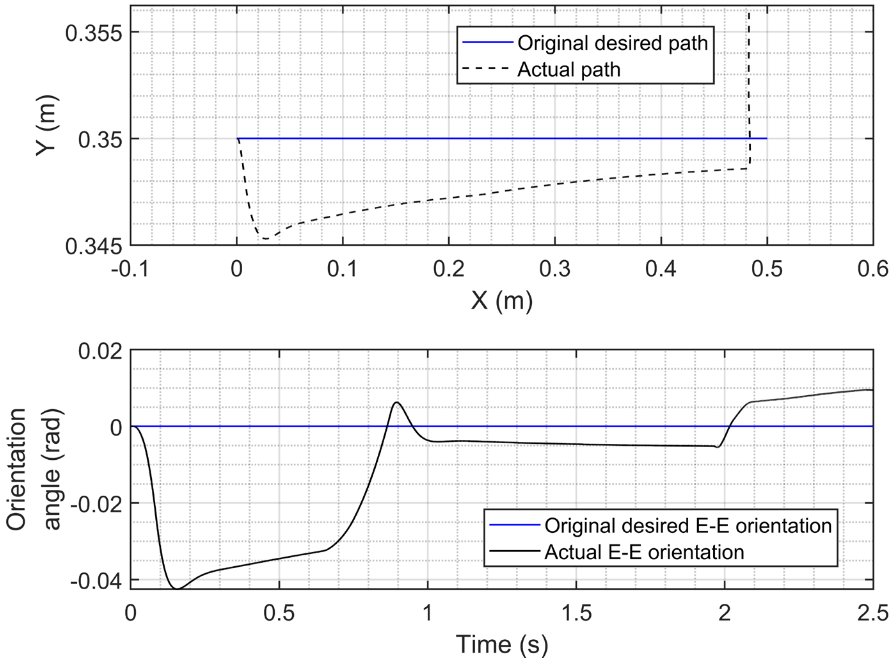

Figure 6.4.3 EE position and orientation for the simple planner, path 1, and collision.

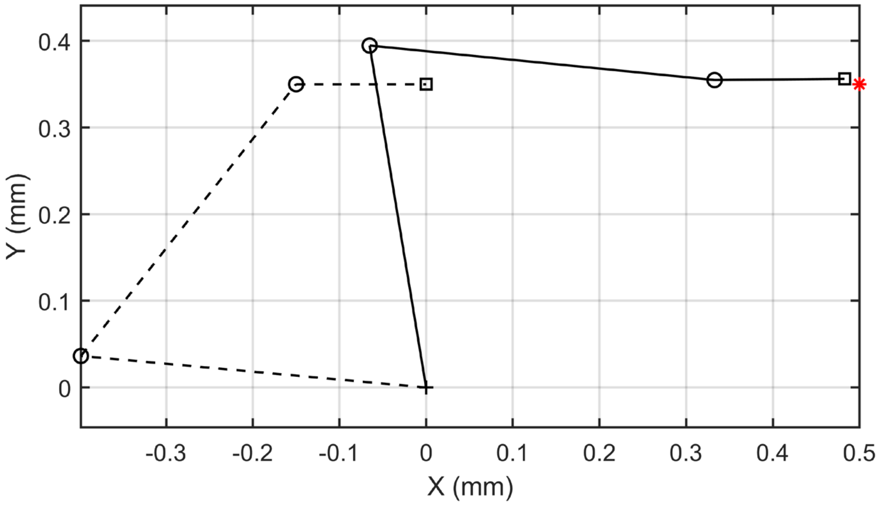

Figure 6.4.4 The robot's links at the start (dashed line) and end (solid line) of the path for the simple planner, path 1 and collision.

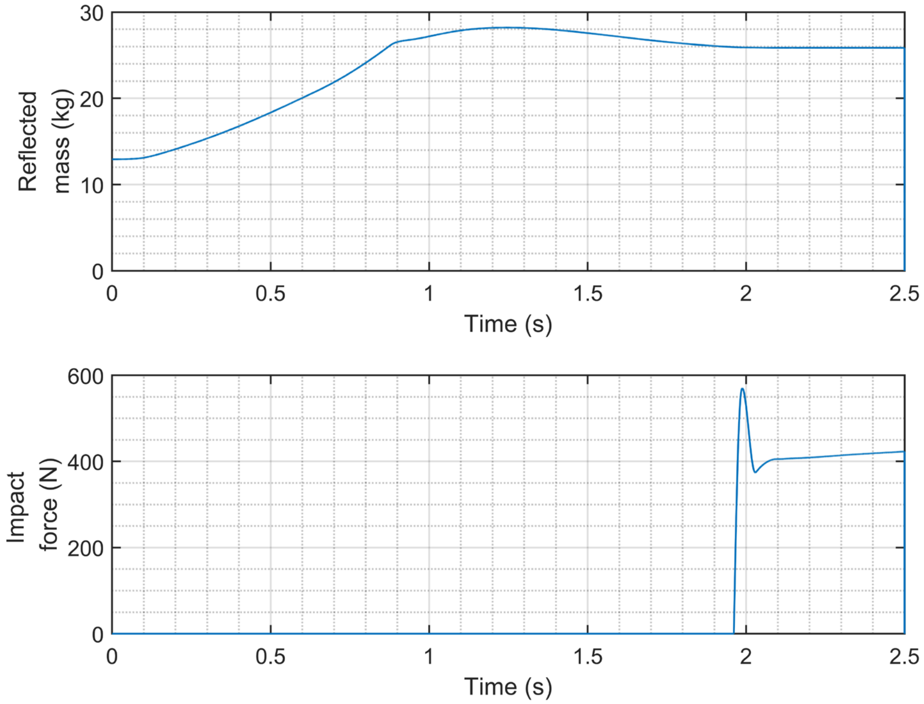

Figure 6.4.5 Reflected mass and impact force for the simple planner and path 1.

Figures 6.4.6 to 6.4.8 shows the corresponding results for the optimal planner. As shown in Figure 6.4.6, the collision happens when the EE reaches the human at x=0.48 m, at just before 2 s, like it did with the simple. Figure 6.4.7 shows that the 3rd link is far from being collinear with the contact normal with the optimal planner. As the results in Figure 6.4.8 show, the robot's configuration when the collision happened made the reflected mass around 7 kg, which is about 75% smaller than its value with the simple planner, and this also reduced the MIF by about 75%. The reflected mass during the motion is also much smaller with the optimal planner, which means the robot will be safer while it is moving. We should mention that the impact force grows slowly after the transient because the integral terms of the motor's controllers are still trying to push the EE towards the target position. This problem can be easily fixed by using either the TAO or WTA reaction strategies.

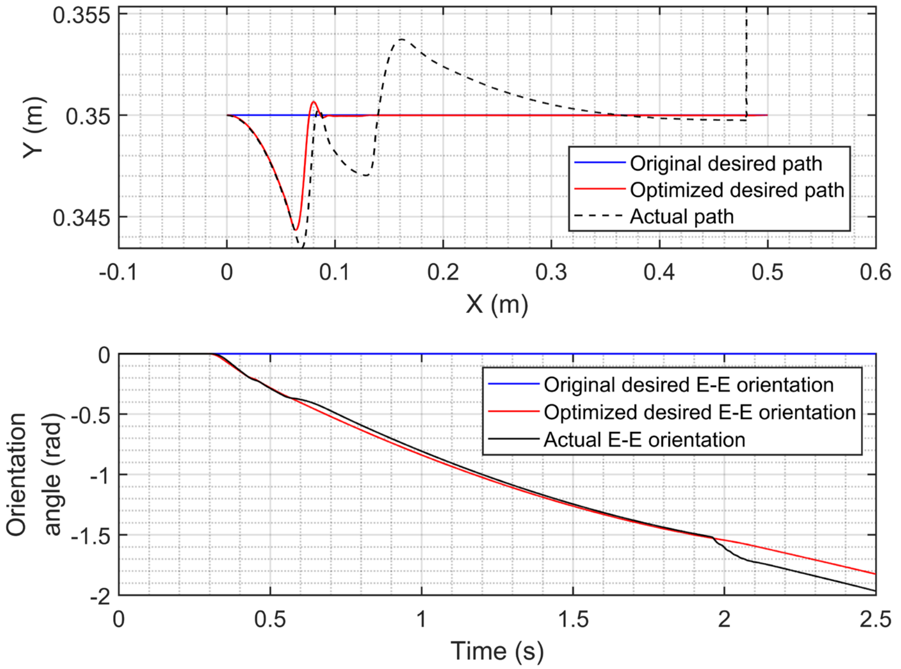

Figure 6.4.6 EE position and orientation angle for the optimal planner, path 1, and collision.

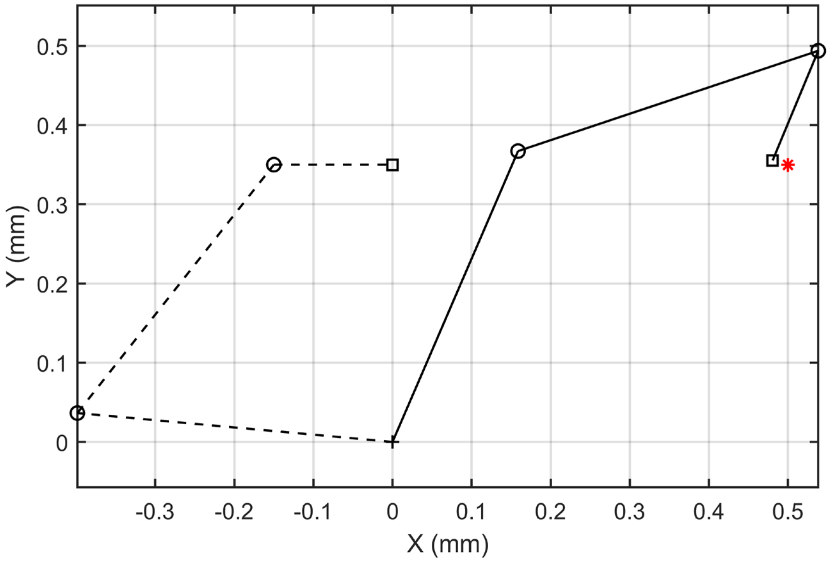

Figure 6.4.7 The robot's links at the start (dashed line) and end (solid line) of the path for the optimal planner, path 1, and collision.

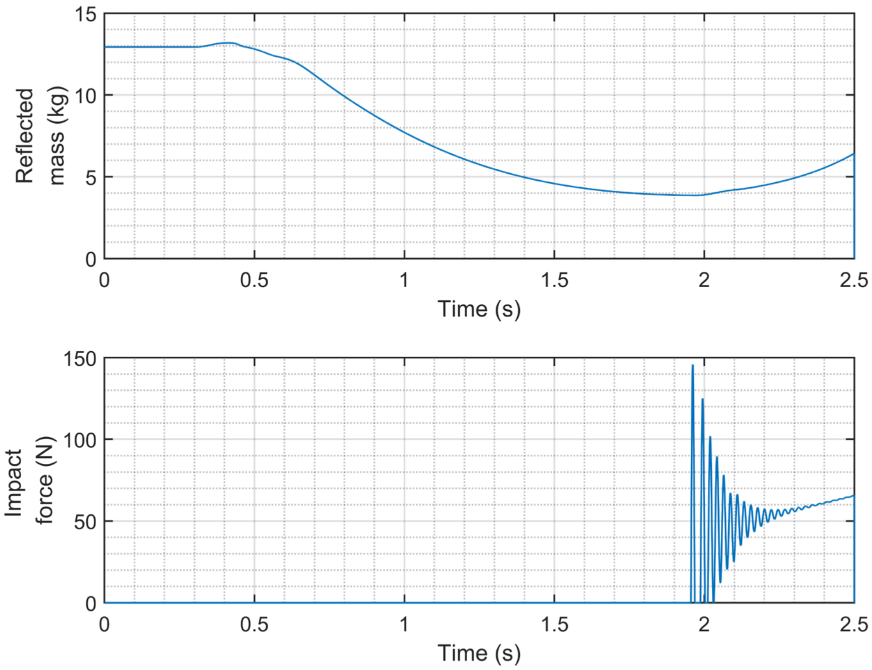

Figure 6.4.8 Reflected mass and impact force for the optimal planner and path 1.

To prove that the benefits of the optimal planner with path 1 were not an isolated case, we simulated both planners with another path, path 2. The path 2 results for the simple planner and optimal planner are shown in Figures 6.4.9-6.4.11 and 6.4.12-6.4.14, respectively. shows these data of the simpler and optimal planner of path 2. These results show similar trends to those seen with path 1. The simple planner produced a large reflected mass and large MIF when the collision happens. It made the robot even more dangerous during the earlier part of the motion when the reflected mass peaked at close to 125 kg (near 1.5 s). When using the optimal planner, the reflected mass was under 10 kg during most of the motion, and was only 7.5 kg when the collision happened. This confirms the optimal planner's effectiveness for different desired paths.

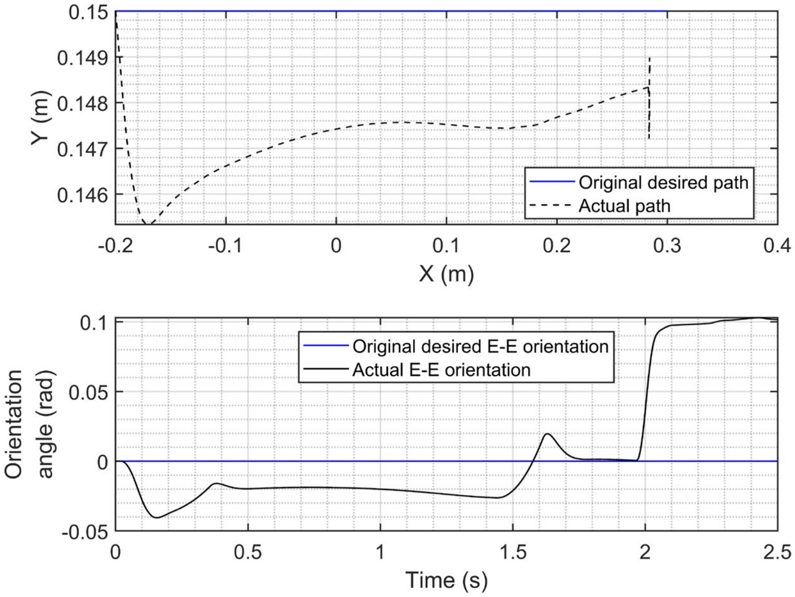

Figure 6.4.9 EE position and orientation angle for the simple planner, path 2, and collision.

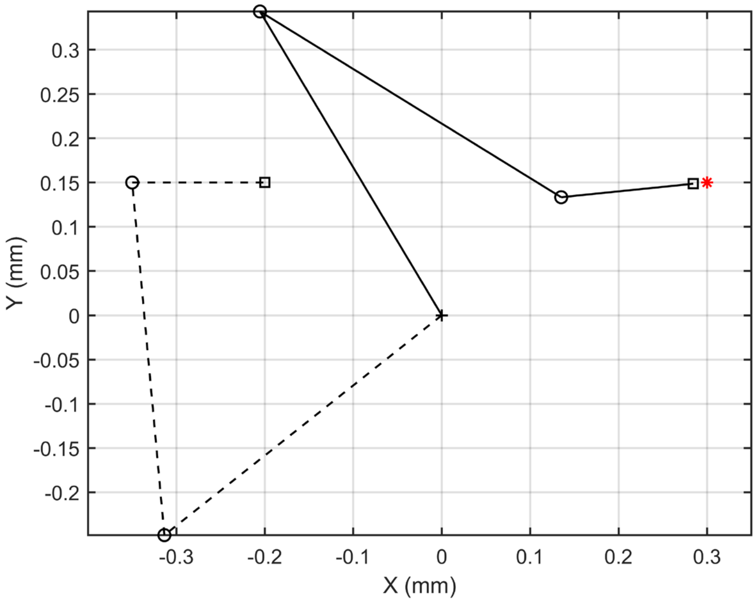

Figure 6.4.10 The robot's links at the start (dashed line) and end (solid line) of the path for the simple planner, path 2, and collision.

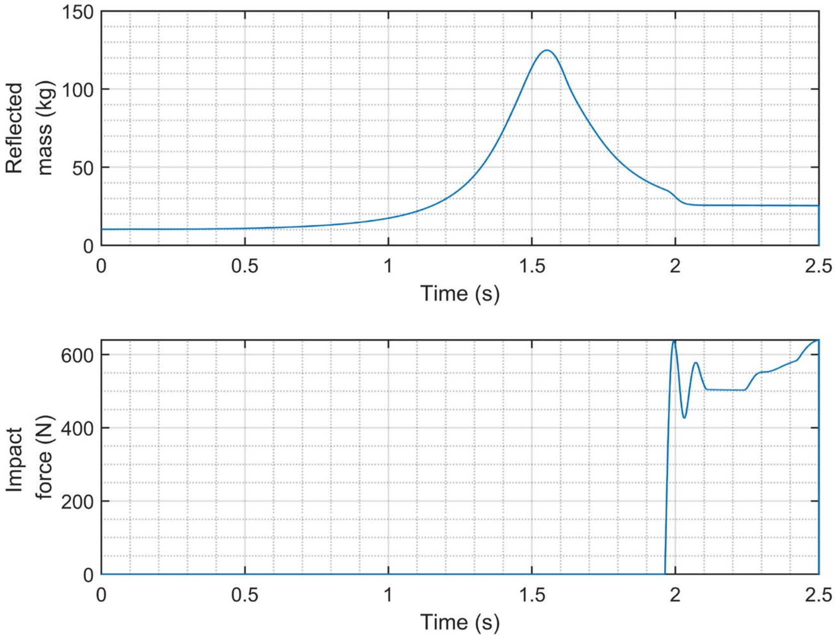

Figure 6.4.11 Reflected mass and impact force for the simple planner and path 2.

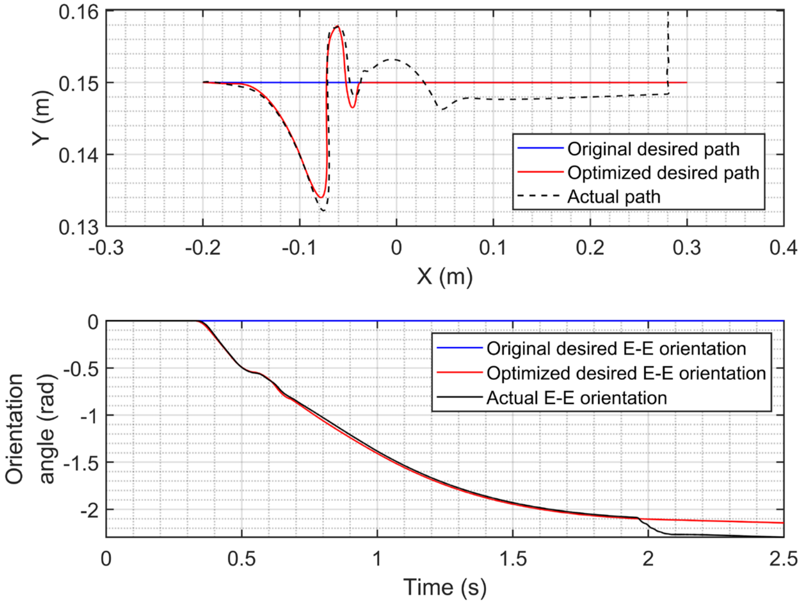

Figure 6.4.12 EE position and orientation angle for the optimal planner, path 2, and collision.

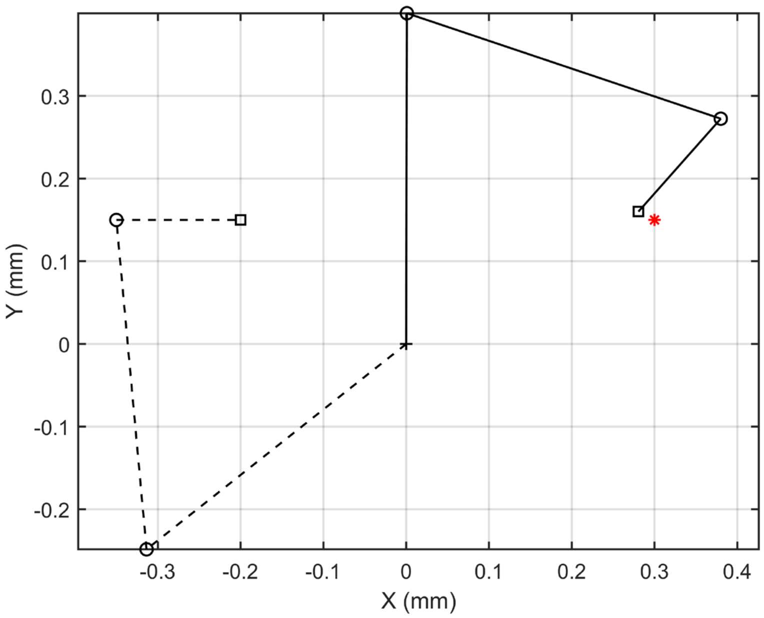

Figure 6.4.13 The robot's links at the start (dashed line) and end (solid line) of the path for the optimal planner, path 2, and collision.

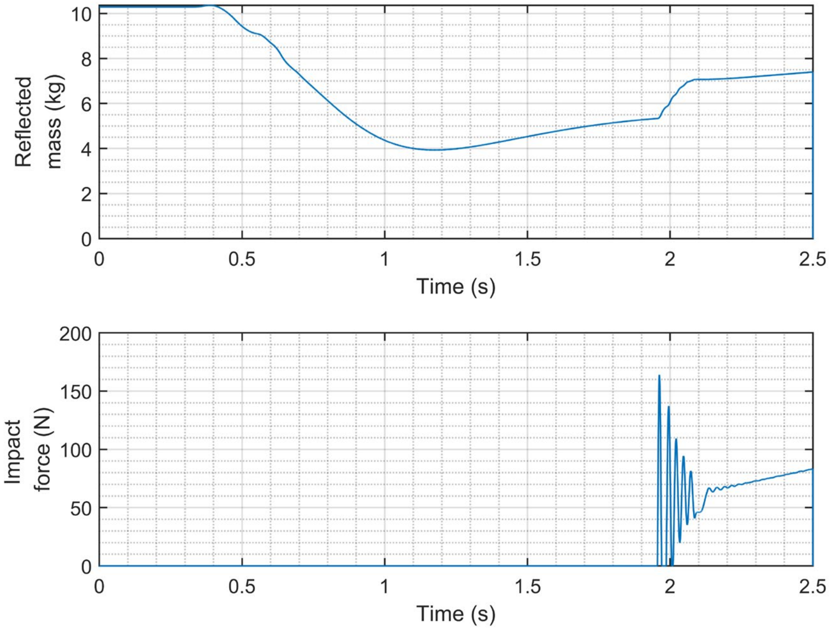

Figure 6.4.14 Reflected mass and impact force for the optimal planner and path 2.

6.5 Summary

An optimal path planner that makes a trade-off between reducing the robot's reflected mass and its path following errors was proposed. Unlike the state-of-the-art path planners for reflected mass reduction, the proposed planner can be used with non-redundant robots, such as the 3R planar robot studied in this chapter.

The chapter begins by presenting the equations the robot's dynamics and reflected mass. The effects of the joint angles and contact normal on the reflected mass were then explored. It was found that the direction of the 3rd link relative to contact normal has the greatest effect, followed by how close the robot is to a singularity. In general, to keep the reflected mass small, the direction of the 3rd link should be as perpendicular to the contact normal as possible.

Next, after presenting the equations for a simple planner and the optimal planner, simulation results for the 3R planar robot following two different paths were presented. The results show that the optimal planner increases the path following errors during the robot's motion when compared with the simple planner, but both planners bring the EE to the target position, unless it is blocked by the human. The optimal planner produces very different configurations of the robot's links than the simple planner. These configurations decreased the robot's reflected mass (and therefore increased its safety) throughout its motion in comparison to the simple planner. For both paths, due to the reductions in the reflected mass, the optimal planner reduced the MIF values by about 75% compared to the values with the simple planner.

CHAPTER 7 CONCLUSIONS AND RECOMMENDATIONS

7.1 Summary

In this research, a variety of actuators and methods for improving robot safety, while maintaining performance, were studied, and compared. Specifically, the safety and performance of a 1-DOF robotic arm driven by EA, SEA, PA and HPEA were compared using computer simulations. For the 1-DOF robot the safety methods studied were adding compliant covering and using the TAO or WTA strategies after detecting the collision. The relationship between collision reaction strategy, collision detection delay and MIF was established for each actuator. Using the EA as the example, the effect of the compliant covering stiffness on the MIF was also studied. The effects on the safety and performance of the desired closed-loop bandwidth with all four actuators, and of the spring stiffness with the SEA, were also investigated. The relationships between joint angles of a 3R planar robot arm and its reflected mass were established. Finally, an optimal path planner for the 3R robot was proposed and shown to be effective at improving safety.

7.2 Achievements

The main achievements of this thesis are as follows.

(1) A detailed and fair comparison of the safety and performance achieved by the EA, SEA, PA and HPEA was performed for a simulated 1-DOF robotic arm whose parameters

were mostly derived from the first joint of a 6-DOF industrial robot. The same desired trajectory, same payload and same collision scenario were employed in all simulations.

(2) Adding compliant covering was found to the most effective method to improve the robot's safety, but the stiffness of the compliant covering must be chosen carefully, or its effectiveness is diminished.

(3) Collision reaction was also proven to be useful for reducing the MIF when used in combination with a compliant covering. The WTA reaction strategy was usually more effective than the TAO strategy. When the collision detection delay was 25 ms, the combination of compliant covering and WTA reduced the MIF values for the EA, SEA, PA and HPEA by 73%, 65%, 65%, and 66%, respectively. However, when the delay was 50 ms or more, no reduction in the MIF occurred.

(4) The distinct values of desired closed-loop bandwidth that produced the best safety and performance were found for each actuator. When using the compliant covering, WTA strategy, and these individually chosen bandwidth values, the EA ranked highest in terms of performance and lowest in terms of safety. The PA was the safest, but ranked 3rd in terms of performance. The SEA was slightly less safe and ranked last in terms of performance. The HPEA achieved the best combination of performance and safety.

(5) The effects of the contact normal and joint angles of a 3R robot on its reflected mass were studied, and conclusions drawn. The direction of the 3rd link relative to the contact normal has the greatest effect, followed by how close the robot is to a

singularity. In general, to keep the reflected mass small, the direction of the 3rd link should be as perpendicular to the contact normal as possible.

(6) A novel optimal path planner that makes a trade-off between reducing the robot's reflected mass and its path following errors was proposed. Unlike prior methods, its use is not limited to redundant robots. The results for a simulated 3R planar robot showed that the optimal planner reduced the MIF by about 75% compared to a simple planner. Though it increased the path following errors, it was still able to bring the EE to the target position precisely.

7.3 Recommendations for future work

(1) The simulation of detection delay in this research was simplified. The program applied the specified detection delay after the impact force became greater than zero. In most real applications, the collision detection uses a signal (e.g., motor current) that is positively correlated with the impact force. This means that the detection delay will not be a constant. Instead, it will be larger when the force increases more slowly. Also, the collision is detected when the signal is larger than a threshold. The threshold must be made larger than the noise level in the signal to prevent false detections. This means that the collision detection time will increase when a noisier signal is used.

(2) In this research, other than the two controllers used with the EA, only one controller was used with each actuator. It would be interesting to see if other controllers such as SMC can provide better performance without worsening safety.

(3) The optimal path planner presented in chapter 6 should be extended so it works with the 6R robotic arms that are common in industry. After performing simulations, it should be tested using a real robotic arm.

(4) An experimental apparatus should be built so the simulation results in chapter 5 can be compared with experimental results.

(5) The WTA strategy is fine for the simulations done in this research, but it is not in its final form. It must be finished before it can be used with a real robot. Commanding the maximum torque will withdraw the arm, but after the torque decelerates the arm it will start accelerating the arm backwards. This could cause the arm to hit the person in a different location or to hit another person. A finished WTA strategy should decelerate the arm to a stop after it has moved a safe distance away from the human's head.

(6) The movement of other joints (especially joint 2) should be considered. We have simulated joint 1 moving the arm in the horizontal plane. If a joint (like joint 2) moves the arm in the vertical plane, then gravity may change the impact force significantly.

References

Ashby, G. (2015). *Design and validation of an improved hybrid pneumatic-electric actuator*. M.A.Sc. Thesis, McMaster University. Retrieved from MacSphere Database. http://hdl.handle.net/11375/18205.

Bae, J., Kong, K., & Tomizuka, M. (2010). Gait phase-based smoothed sliding mode control for a rotary series elastic actuator installed on the knee joint. *Proceedings of the 2010 American Control Conference*, 6030–6035. https://doi.org/10.1109/ACC.2010.5531282

Bicchi, A., & Tonietti, G. (2004). Fast and "Soft-Arm" Tactics. *IEEE Robotics & Automation Magazine*, *11*(2), 22–33. https://doi.org/10.1109/MRA.2004.1310939

CAN/CSA-Z434-14. (n.d.). *Industrial robots and robot systems. Canadian Standards Association*. CSA Group. Retrieved February 23, 2022, from https://www.csagroup.org/store/product/

De Luca, A., Albu-Schaffer, A., Haddadin, S., & Hirzinger, G. (2006). Collision Detection and Safe Reaction with the DLR-III Lightweight Manipulator Arm. *2006 IEEE/RSJ International Conference on Intelligent Robots and Systems*, 1623–1630. https://doi.org/10.1109/IROS.2006.282053

Ferretti, G., Magnani, G., & Rocco, P. (2004). Impedance control for elastic joints industrial manipulators. *IEEE Transactions on Robotics and Automation*, *20*(3), 488–498. https://doi.org/10.1109/TRA.2004.825472

Haddadin, S., Albu-Schaffer, A., & Hirzinger, G. (2008). The role of the robot mass and velocity in physical human-robot interaction - Part I: Non-constrained blunt impacts. *2008 IEEE International Conference on Robotics and Automation*, 1331–1338. https://doi.org/10.1109/ROBOT.2008.4543388

Han, Y., Wu, J., & Xiong, Z. (2017). A new method for sensorless collision detection on the servo level. *2017 IEEE International Conference on Advanced Intelligent Mechatronics (AIM)*, 553–558. https://doi.org/10.1109/AIM.2017.8014075

ISO 10218-1:2011(en). *Robots for industrial environments – Safety requirements – Part I: Robot. International organization for standardization*. ISO. https://www.iso.org/cms/render/live/en/sites/isoorg/contents/data/standard/05/13/51330.html

ISO/TS 15066:2016(en), Robots and robotic devices—Collaborative robots. (n.d.). Retrieved August 12, 2022, from https://www.iso.org/obp/ui/#iso:std:iso:ts:15066:ed-1:v1:en

Kang, S., Komoriya, K., Yokoi, K., Koutoku, T., Kim, B., & Park, S. (2010). Control of impulsive contact force between mobile manipulator and environment using effective mass and damping controls. *International Journal of Precision Engineering and Manufacturing*, *11*(5), 697–704. https://doi.org/10.1007/s12541-010-0082-4

Khatib, O. (1995). Inertial Properties in Robotic Manipulation: An Object-Level Framework. *The International Journal of Robotics Research*, *14*(1), 19–36. https://doi.org/10.1177/027836499501400103

Kulić, D., & Croft, E. A. (2005). Safe planning for human-robot interaction. *Journal of Robotic Systems*, *22*(7), 383–396. https://doi.org/10.1002/rob.20073

Mansfeld, N., Djellab, B., Veuthey, J. R., Beck, F., Ott, C., & Haddadin, S. (2017). Improving the performance of biomechanically safe velocity control for redundant robots through reflected mass minimization. *2017 IEEE/RSJ International Conference on Intelligent Robots and Systems (IROS)*, 5390–5397. https://doi.org/10.1109/IROS.2017.8206435

Petrosky, L. J., & County, W. (1987). *54) HYBRD ELECTRO-PNEUMATIC ROBOT JOINT ACTUATOR*. 6.

Pratt, G. A., & Williamson, M. M. (1995). Series elastic actuators. *Proceedings 1995 IEEE/RSJ International Conference on Intelligent Robots and Systems. Human Robot Interaction and Cooperative Robots*, *1*, 399–406. https://doi.org/10.1109/IROS.1995.525827

Rossi, R., Polverini, M. P., Zanchettin, A. M., & Rocco, P. (2015). A pre-collision control strategy for human-robot interaction based on dissipated energy in potential inelastic impacts. *2015 IEEE/RSJ International Conference on Intelligent Robots and Systems (IROS)*, 26–31. https://doi.org/10.1109/IROS.2015.7353110

Rouzbeh, B., & Bone, G. M. (2018a, May 30). Impact Force Reduction Strategies To Achieve Safer Human-Robot Collisions. *Progress in Canadian Mechanical Engineering*. 2018 Canadian Society for Mechanical Engineering (CSME) International Congress. https://doi.org/10.25071/10315/35249

Rouzbeh, B., & Bone, G. M. (2018b, May 30). Impact Force Reduction Strategies To Achieve Safer Human-Robot Collisions. *Progress in Canadian Mechanical Engineering*. 2018 Canadian Society for Mechanical Engineering (CSME) International Congress. https://doi.org/10.25071/10315/35249

Rouzbeh, B., & Bone, G. M. (2018c, May 30). Impact Force Reduction Strategies To Achieve Safer Human-Robot Collisions. *Progress in Canadian Mechanical Engineering*. 2018 Canadian Society for Mechanical Engineering (CSME) International Congress. https://doi.org/10.25071/10315/35249

Rouzbeh, B., Bone, G. M., & Ashby, G. (2018a). High-Accuracy Position Control of a Rotary Pneumatic Actuator. *IEEE/ASME Transactions on Mechatronics*, *23*(6), 2774–2781. https://doi.org/10.1109/TMECH.2018.2870177

Rouzbeh, B., Bone, G. M., & Ashby, G. (2018b). High-Accuracy Position Control of a Rotary Pneumatic Actuator. *IEEE/ASME Transactions on Mechatronics*, *23*(6), 2774–2781. https://doi.org/10.1109/TMECH.2018.2870177

Rouzbeh, B., Bone, G. M., Ashby, G., & Li, E. (2019a). Design, Implementation and Control of an Improved Hybrid Pneumatic-Electric Actuator for Robot Arms. *IEEE Access*, *7*, 14699–14713. https://doi.org/10.1109/ACCESS.2019.2891532

Rouzbeh, B., Bone, G. M., Ashby, G., & Li, E. (2019b). Design, Implementation and Control of an Improved Hybrid Pneumatic-Electric Actuator for Robot Arms. *IEEE Access*, *7*, 14699–14713. https://doi.org/10.1109/ACCESS.2019.2891532

Rouzbeh, B., Bone, G. M., Ashby, G., & Li, E. (2019c). Design, Implementation and Control of an Improved Hybrid Pneumatic-Electric Actuator for Robot Arms. *IEEE Access*, *7*, 14699–14713. https://doi.org/10.1109/ACCESS.2019.2891532

Rouzbeh, B., Bone, G. M., Ashby, G., & Li, E. (2019d). Design, Implementation and Control of an Improved Hybrid Pneumatic-Electric Actuator for Robot Arms. *IEEE Access*, *7*, 14699–14713. https://doi.org/10.1109/ACCESS.2019.2891532

Shin, D., Sardellitti, I., Park, Y.-L., Khatib, O., & Cutkosky, M. (2010). Design and Control of a Bio-inspired Human-friendly Robot. *The International Journal of Robotics Research*, *29*(5), 571–584. https://doi.org/10.1177/0278364909353956

Siciliano, B., Sciavicco, L., Villani, L., & Oriolo, G. (2008). *Robotics: Modelling, Planning and Control* (1st ed. 2009 edition). Springer.

Slotine, J.-J. E., & Li, W. (1991). *Applied nonlinear control*. Prentice Hall.

Sun, J., Guo, Z., Sun, D., He, S., & Xiao, X. (2018). Design, modeling and control of a novel compact, energy-efficient, and rotational serial variable stiffness actuator

(SVSA-II). *Mechanism and Machine Theory*, *130*, 123–136. https://doi.org/10.1016/j.mechmachtheory.2018.07.024

Toedtheide, A., Lilge, T., & Haddadin, S. (2016). Antagonistic Impedance Control for Pneumatically Actuated Robot Joints. *IEEE Robotics and Automation Letters*, *1*(1), 161–168. https://doi.org/10.1109/LRA.2015.2511663

Universal Robots. (2015). Universal Robots. http://www.universal-robots.com/how-tos-andfaqs/faq/ur-faq/max- joint-torques-17260/

Viano, D. C. (2003). Seat Influences on Female Neck Responses in Rear Crashes: A Reason Why Women Have Higher Whiplash Rates. *Traffic Injury Prevention*, *4*(3), 228–239. https://doi.org/10.1080/15389580309880

Walker, I. D. (1990). The use of kinematic redundancy in reducing impact and contact effects in manipulation. *Proceedings., IEEE International Conference on Robotics and Automation*, 434–439. https://doi.org/10.1109/ROBOT.1990.126016

Willinger, R., Bourdet, N., Fischer, R., & Le Gall, F. (2005). Modal analysis of the human neck in vivo as a criterion for crash test dummy evaluation. *Journal of Sound and Vibration*, *287*(3), 405–431. https://doi.org/10.1016/j.jsv.2004.11.008

Yamada, Y., Hirasawa, Y., Huang, S., Umetani, Y., & Suita, K. (1997). Human-robot contact in the safeguarding space. *IEEE/ASME Transactions on Mechatronics*, *2*(4), 230–236. https://doi.org/10.1109/3516.653047

Zeng, L., & Bone, G. M. (2013a). Design of elastomeric foam-covered robotic manipulators to enhance human safety. *Mechanism and Machine Theory*, *60*, 1–27. https://doi.org/10.1016/j.mechmachtheory.2012.09.010

Zeng, L., & Bone, G. M. (2013b). Design of elastomeric foam-covered robotic manipulators to enhance human safety. *Mechanism and Machine Theory*, *60*, 1–27. https://doi.org/10.1016/j.mechmachtheory.2012.09.010

Zheng, H., Wu, M., & Shen, X. (2016). Pneumatic Variable Series Elastic Actuator. *Journal of Dynamic Systems, Measurement, and Control*, *138*(8), 081011. https://doi.org/10.1115/1.4033620

Zhu, Y., & Barth, E. J. (2005). Impedance Control of a Pneumatic Actuator for Contact Tasks. *Proceedings of the 2005 IEEE International Conference on Robotics and Automation*, 987–992. https://doi.org/10.1109/ROBOT.2005.1570245